Full-Field Quantitative Visualization of Shock-Driven Pore Collapse in Solids: Mechanics of Deformation, Failure, and Interaction

Thesis by
Barry Patrick Lawlor

In Partial Fulfillment of the Requirements for the
Degree of
Doctor of Philosophy

CALIFORNIA INSTITUTE OF TECHNOLOGY
Pasadena, California

2025
Defended May 19th, 2025

Barry Patrick Lawlor
ORCID: 0000-0003-4487-2129

To my wife, parents, and Heavenly Father, who are my support, inspiration, strength, and joy.

ACKNOWLEDGEMENTS

Apart from the incredible community around me, I certainly would not be where I am today. Without the academic support of my advisor, mentors, and colleagues, this thesis would be a shadow of what it has grown to become. And without the support of my family, friends, church, and God, I would not have survived the rigors and stress of this PhD program, let alone thrived and grown in the process.

I would like to thank my advisor, Guruswami Ravichandran, for his unwavering support and optimism for my research and career goals. Even while he was on leave across the world, he made time each week to discuss results, guide me along, and reel me back when I strayed too far down the wrong path. There is much that I could say about Ravi's enthusiasm for research, extensive reading and knowledge, great wisdom in life, entertaining stories, insightful quotes, and his care for people. But what sticks out to me most is the extreme patience that he has shown me, whether I hit a snag in some detail of the research or my experiments failed and weeks of work went down the drain. Ravi consistently offered encouragement amidst the failures, gave undeserved praise for the successes, and provided me with the guidance and time I needed to grow as a scientist and put together a worthwhile thesis. Truly, none of this would have been accomplished without him.

I am also incredibly grateful to the rest of my committee: Kaushik Bhattacharya, Mike Mello, and Joe Shepherd. Kaushik has always made time to chat and offer insightful ideas for research, and he welcomed me as an honorary Kaushik group member when Ravi was on leave. I will be continually grateful for the Ravi-Kaushik group meetings where I learned to think critically about mechanics, ask the right questions, see past the window dressing, and become a confident presenter of research myself. I think it is safe to say that Kaushik is the driving force of those meetings and is responsible for much of what I have learned there.

I am thankful to Mike for his mentorship as well, and for generously sharing his enthusiasm toward my research. He has always been willing to help in whatever way possible, whether with research, career advice, or otherwise. Mike has also shown me what it looks like to invest in the next generation through

his excitement and passion for teaching and mentorship, which inspires me to exemplify those qualities as well.

I appreciate Joe's kindness in showing enthusiasm for my research and his willingness to chat anytime we pass each other in the Guggenheim hallways. His sharp insight into the world of experimental mechanics has been an inspiration and has greatly aided my thesis work as well.

I also gratefully acknowledge the funding support of DOE/NNSA award nos. DE-NA0003957 and DE-NA0004229. The support of the Army Research Laboratory under the Cooperative Agreement Number W911NF-12-2-0022 for the acquisition of the high-speed camera used in these investigations is also acknowledged.

I want to thank my lab-mate, mentor, and dear friend, Vatsa Gandhi for all his help and support, especially when I was a young student. Vatsa allowed me to follow him around the lab for months as he patiently answered my seemingly endless list of questions. He taught me to carefully design experiments, to examine every possibility and assumption, and to pick myself up after failure, formulate a new plan, and regain my optimism. I'm incredibly grateful to have had Vatsa as a source of wisdom, a sounding board, and a friend throughout my PhD and beyond. Some highlights of our time at Caltech include our first successful windowed iron and pore collapse shots, many conference adventures, late nights finishing papers, elevator rides after successful experiments, boba and ramen runs, and tennis games.

I am also continually grateful to my undergraduate advisor, Veronica Eliasson, who gave me a chance as a young undergraduate to start doing research, inspired my interest in experimental mechanics, and has been a continual support of my goals. I would not be here without her help. I would also like to thank Suraj Ravindran for his kind support. He has continually checked in on my research progress and encouraged me along in both my research and career aspirations.

This journey at Caltech was made possible (and enjoyable) by the many friends who I had the pleasure of trudging alongside. I would not have survived the first year without our study group of Kevin Nakahara, Flora Xia, and Ozair Rajani. Kevin and I also navigated the Zoom-learning first year together as roommates, and he later gave me a glimpse into the world of nanoarchitected

materials through his research. I will always appreciate our friendship and all that I have learned from him. My good friends, Aakila Rajan, Sathvik Sanagala, and Adeline Wihardja have also been continual sources of knowledge, encouragement, and good times, whether through studying for quals, struggling through research, enjoying overcooked hangouts, sharing good food, etc. Likewise, I am grateful for the friendships built among the group in the GT 305 office. Vatsa Gandhi, Jack Weeks, Andy Akerson, Eric Ocegueda, and Shengduo Liu have been excellent mentors, who were critical to my success through quals and candidacy. Likewise, the other group members: Amanda Toledo Barrios, Carter Cocke, Mayank Raj, Theresa Tsaggaris, Maximo Cravero, Aditya Shedge, Keyang Yang, and Hi'ilei Dikilato have made the office and lab a great place to work, learn, and collaborate.

I have to give a special shoutout to all those who graciously came to sit in the lab for hours as a safety buddy while I ran my shots. I would not have been allowed (literally) to complete my research without your help!

This research would not have been possible without the help of the Galcit Shop machinists: Ali Kiani and Brandon Niles. Their incredible timing and precision on all my jobs has been a huge help, especially for samples with 800 μm pores aligned perfectly together, for which Ali has always delivered. I could also always count on Ali for a friendly "who's there" and warm smile when I came by the shop, which I will miss.

Likewise, I am grateful to Petros Arakelian for his help in the lab, providing his expertise to troubleshoot equipment and tracking down items that we needed for our experiments. I am also grateful to Donna Mojahedi for her continual help with travel arrangements and my incessant purchase requests for parts in the lab. Jenni Campbell has also been a huge help in navigating the program and coordinating logistics, and she has been kind to regularly ask how life is going. The help of the rest of the staff is greatly appreciated as well. Lynn Seymour and Jamie Meighen-Sei have kept things running smoothly, even amidst the chaos of basement floods, fires, and perpetual construction; Christine Ramirez and Stacie Takase have been greatly helpful as well.

My church community, both in San Diego and here in Los Angeles, have helped me to be rooted in Christ throughout this journey. I am indebted to the leaders, who have cared for my soul and have sought to understand the unique challenges of this PhD program. The friends there—too many to list

here—have been invaluable: providing a constant source of joy, encouragement and strength to work well and for God's glory. Their wisdom and experience in life have been an enormous help to me as I walk through this stage of life. They have also graciously learned more about dynamic experiments than they probably ever cared to.

My family: Dad, Mom, Conor, Wesley, and Fiona have whole-heartedly supported me along this entire journey, for which I am so grateful. My parents truly deserve all the credit for this accomplishment. They raised me to pursue excellence with integrity, to accept failure without excuse, and to never shy away from the hard work required to do things the right way. I want to give a special acknowledgement to my dad, who has been my inspiration to pursue a PhD and make the best use of the gifts that God has given me. He is an example of a man who works faithfully unto the Lord, strives for integrity in all that he does, and allows his actions and results to speak for themselves. My family by marriage: Isabel, Elizabeth, Father-in-law, Mother-in-law, Anita, James, Briana, Jun, and Miranda have been a great support and encouragement as well, for which I am thankful.

My wonderful wife, Erica, deserves my warmest acknowledgement. She has been with me throughout this entire journey and has been an unwavering support. She is my comforter in times of research despair, my joy amidst stressful seasons, my reminder that there is much more to life than work and research, and my partner as we tackle all that life brings us. Though she has not been trained as an engineer, she has happily listened to all my research problems, rejoiced with me after finding exciting results, listened to my presentations, and sought to learn my thesis research and explain it to her friends. Words cannot describe how fortunate I am to have married her, and I am eternally grateful for her love and support.

Finally, and most importantly, I would like to thank my Heavenly Father, who has sustained me all these years and who deserves all the glory. When I am weak, He strengthens me; when I am confused, He is gracious to illumine my mind; when I am weary, He gives me endurance. Most importantly, He saved me and He has given me eternal hope that puts into perspective all the challenges and failures throughout life and this PhD program. It's been a privilege and pleasure to spend these years studying His marvelous creation.

The heavens declare the glory of God,
and the sky above proclaims his handiwork.
Day to day pours out speech,
and night to night reveals knowledge.
There is no speech, nor are there words,
whose voice is not heard.
Their voice goes out through all the earth,
and their words to the end of the world.

–Psalm 19:1-4

ABSTRACT

Porosity in solids is ubiquitous throughout engineering applications: inherent in energetic materials and exaggerated upon degradation, incorporated into shock-absorbing structures via materials such as metallic foams and metamaterials, and arising through manufacturing defects—especially in metal additive manufacturing methods. In these applications, many phenomena at both the macro- and meso-scale are critical to the operation under dynamic compression. Macroscopic shock wave structure, including shock attenuation and disruption are important for engineered structures like metallic foams, while mesoscopic localized shear deformation near porous defects can be a cause of failure in structures and is thought to be a mechanism for mechanically-induced hot spots in energetic materials which can dictate their ignition behavior. While the macroscopic shock response of porous materials has been well studied, the mesoscopic response has received less attention. Recent studies have improved the understanding through sophisticated numerical simulations and pore collapse experiments leveraging innovative high-speed imaging technologies, but many details of the mesoscopic response remain unclear.

This thesis is focused on the mesoscopic domain, with an overarching goal of characterizing local details of pore collapse, such as the rate of collapse, pore geometry (asymmetry) evolution, deformation induced in the material surrounding the pore, localization/failure mechanisms, and interactions between pores. Fundamental understanding of these mesoscopic phenomena is a critical step toward unraveling the physics which couple the mesoscale and macroscale responses, enabling predictive modeling for the dynamic response of porous materials/structures, and developing innovative engineering designs with porous materials.

The first part of this thesis develops a novel internal digital image correlation (DIC) technique for use in full-scale dynamic laboratory experiments, which enables investigation of phenomena which occur under confinement or are sensitive to boundary effects. The technique consists of manufacturing transparent specimens with an internally embedded speckle pattern, which is then dynamically deformed via the experiment of choice. During dynamic loading, the internal speckle pattern is visualized with a high-speed camera, after which DIC software is used to process the images and compute the displacement, ve-

locity, and strain fields. The technique is implemented and validated using polymethyl methacrylate (PMMA) specimens under compression with split-Hopkinson (Kolsky) pressure bar and plate impact experiments—providing validation under both uniaxial stress and uniaxial strain conditions, at strain rates of $10^3 - 10^6\,\mathrm{s}^{-1}$ and impact stresses up to 0.65 GPa.

The second part of the thesis implements the internal DIC technique to investigate the mechanics of a single spherical pore during collapse induced by weak shock loading up to 1 GPa impact stress in PMMA. The first of its kind internal strain measurements reveal concentrations around the collapsing pore, which are approximately consistent with elastostatic theory. Equivalent shear strain measurements uncover a transition from classical strain concentrations to the development of shear bands at 0.6 GPa, and raw deformation images show the development of fracture at 0.8 GPa—representing two distinct failure mechanisms arising within a small range of impact stresses. The shear bands arise due to large stress concentrations near the pore, which leads to plastic deformation and heating. Thermal softening generates local material instabilities, which can grow into regions of large, localized deformation. These bands are captured via explicit finite element analysis through a thermo-viscoplastic material model. The numerical simulations further indicate the crack to be a shear crack propagating through the weakened material of an adiabatic shear band. Finally, theoretical approaches elucidate the mechanics which govern the initiation of, spacing between, and preferred paths for these failure modes.

The third part of the thesis follows a natural extension toward real porous media, investigating the collapse of pore arrays in PMMA with a focus on the role of interactions between pores on the localization and failure response. Experiments are conducted on pairs of pores in vertical and horizontal configurations. By utilizing internal DIC and shadowgraphy, the evolution of shear bands and cracks is visualized and measured. Further, apparent interactions between pores are identified through shifts in impact stress thresholds for failure initiation and through delayed crack growth. Baroclinicity, and accompanying baroclinic torque, is identified as the driving mechanism for crack propagation in these experiments. Finally, shear diffraction waves initiate upon plane wave interaction with pores and propagate toward neighboring pores. This is considered as a possible interaction mechanism between pores which alters the failure response.

The work presented in this thesis enabled the first *in-situ* observation of adiabatic shear banding during pore collapse in addition to a much-improved spatiotemporal characterization of crack propagation compared to previous works. Analysis of the experimental results revealed the ability of theoretical and numerical (FEA) models to capture many details of shear localization in pore collapse. Further analysis unraveled mechanisms governing pore collapse and associated failure modes, including the importance of pore asymmetry during collapse as well as planar shock interaction with the pore and the resultant baroclinicity and diffracted shear waves.

PUBLISHED CONTENT AND CONTRIBUTIONS

[1] B. P. Lawlor, V. Gandhi, and G. Ravichandran, "An internal digital image correlation technique for high-strain rate dynamic experiments," Experimental Mechanics **65**, 407–419 (2025),
Contributions: B.P.L. participated in the conception of the project, developed the technique, performed the experiments, analyzed the experimental data, and wrote the manuscript.

[2] B. P. Lawlor, V. Gandhi, and G. Ravichandran, "Full-field quantitative visualization of shock-driven pore collapse and failure modes in PMMA," Journal of Applied Physics **136**, 225901 (2024),
Contributions: B.P.L. participated in the conception of the project, performed the experiments, conducted the numerical simulations, integrated the theoretical analysis, analyzed the results, and wrote the manuscript.

[3] B. P. Lawlor and G. Ravichandran, "Mechanics of collapse in pore arrays and their interaction in shock compressed PMMA," (In Preparation) (2025),
Contributions: B.P.L. participated in the conception of the project, performed the experiments, conducted the numerical simulations, integrated the theoretical analysis, analyzed the results, and wrote the manuscript.

CONTENTS

LIST OF FIGURES

LIST OF TABLES

Chapter 1

INTRODUCTION

1.1 Motivation

Characterizing the response of materials under extreme conditions has been of great importance for the better part of the last century, whether under extreme pressures, temperatures, deformation rates, or other conditions. In that time, the number of engineering applications operating at extreme conditions has only grown. Dynamic loading in these applications, which generates both high-strain rates and high pressures, requires accurate material characterization across a large range of strain rates and pressures. Such applications, listed in approximate order of increasing strain rate, include: dropped electronics; collisions and impacts in sports and combat, for which protective gear (especially helmets) is designed; automobile collisions; debris impact onto wind-turbines, automobiles, trains, or aircraft; bird strike events on aircraft fuselages, windshields, or engines; blast, explosive, and implosive loading; armor and anti-armor, ballistics; energetic materials; micro-meteorite or orbital debris impact onto spacecraft; and laser shocks, inertial confinement [1].

Various experimental techniques have been developed for the purpose of high-strain rate material characterization, such as drop tower testing, split-Hopkinson (Kolsky) pressure bar [2, 3], plate impact [1, 4, 5], pulsed power accelerators [6], hyper-velocity impact, and laser-driven shock [7]. Investigations using these techniques have revealed various complex behaviors of materials under high-strain rates. From a macroscopic perspective, different constitutive relations have been characterized, including the effects of strain rate hardening, thermal softening (adiabatic conditions at high rates), pressure-dependent strength, and shock-induced phase transitions [1]. At the local scale, many failure modes have been observed such as dynamic fracture [8], adiabatic shear banding [9], spall failure [1, 10], and other localized deformations (e.g., jetting).

Given the demand for engineering designs which can withstand the extreme loads imposed during dynamic impacts, it is necessary to approach the problem from both material and structural perspectives. To this end, it is necessary to develop the ability to accurately and predictively model both the macroscopic

response and local failure involved in such impact scenarios. Additionally, one needs a deep grasp of the fundamental mechanics and physics at play in order to design materials and structures to achieve desirable qualities while mitigating failure, and to do so without resorting to a trial-and-error approach. This has been the continued focus and accomplishment of the vast research conducted in this domain.

1.2 Shock Compression of Porous Media

1.2.1 Porous Media Applications

Porous media have exhibited many unique qualities and behaviors, especially in the dynamic impact regime. Under static loading, pores are generally considered to be stress concentrators and potential locations for failure—a poor quality for structural integrity. However, in the dynamic regime, pores have been identified as sources of both material property enhancement and degradation, depending on the property in question, as illustrated through examples in Fig. 1.1. Among the beneficial qualities of porous materials for impact loading is shock attenuation, accomplished through energy absorption due to the large plastic deformation required to close the pores [11–14], and shock disruption, or widening of the shock, via micro-inertial and wave-scattering effects [15, 16]. Conversely, during pore collapse, pores have been identified as the site for failure via localization such as jetting and cracking [17]. It has also been suggested that collapsing pores can nucleate adiabatic shear bands at the pore surface [18] which was later demonstrated to be true in this thesis [19] and other concurrent works [20, 21]. Finally, the influence of porosity on spall strength of materials has been more enigmatic, sometimes improving the spall strength and other times degrading it, depending on the base material properties and details of the initial porosity [14, 22, 23].

Porosity in engineered structures is highly prevalent, both as a design feature and as a defect in manufacturing processes, as shown in Fig. 1.1. Engineered materials, such as metallic foams or metamaterials, have intentionally incorporated porosity, often with the intention of being used for energy absorption. On the other hand, additive manufacturing processes, especially powder-bed metal printing, result in porosity as a primary defect type [26]. In fact, even traditional material processes such as casting suffer from porosity, though typically to a lesser degree. Another manufacturing technique, shock compaction

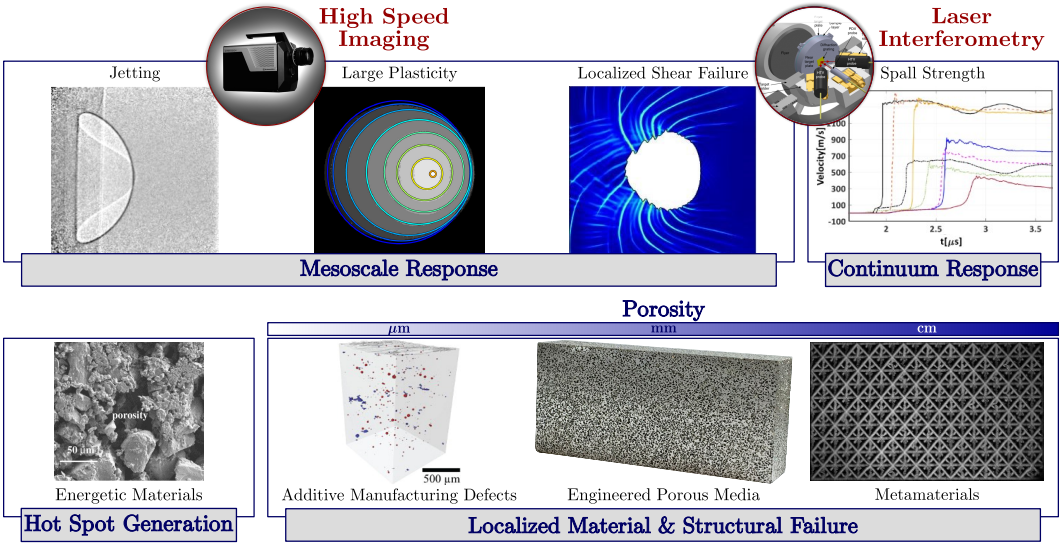

Figure 1.1: Pore collapse phenomena (top); applications and failure concerns for porous media (bottom). Top row, from left to right: jetting phenomena observed in collapsing pores in PMMA [17], large plastic deformation during shock-induced collapse of holes in copper [24], predicted shear localization near a shock loaded pore in PMMA via numerical simulations [18], increased spall strength in porous additive manufactured aluminum 6061 [23]. Bottom row, left to right: degraded LX-14 energetic material displaying substantial porosity [25], porosity in electron beam melted Ti-6Al-4V [26], aluminum foam sample, octet-truss lattice structure [27]. Figures reproduced with permission from publishers.

of powders, uses dynamic compression to form bulk materials with unique properties [28] (e.g., polycrystalline diamond [29, 30]) from powders [1, 31–33]. Here, pore collapse plays a critical role in the manufacturing process, but may also be a cause of the local imperfections generated during manufacturing, such as cracks. Further, in the energetics community, porosity is a common feature, especially in energetic materials that have undergone mechanical or thermal degradation [25].

Given the opportunities for engineered material enhancement via porosity, the ubiquity of pores as manufacturing defects, and the role of pores in reaction initiation for energetics, it is critical to learn how to leverage the beneficial qualities while simultaneously mitigating the harmful ones. To do this, one must fundamentally understand the mechanisms which govern the local and macroscopic behaviors of porous media under impact loading. Such understanding may help answer practical questions such as those regarding: the size of pore which can be tolerated, the impact loads for which a design can be

rated, the sensitivity of energetic materials to impact, and the level of porosity and pore connectivity which is acceptable.

1.2.2 Macroscopic Response

Shock compression of porous media has received extensive treatment at the macroscale. From the theoretical perspective, Herrmann developed the $P-\alpha$ model which incorporated porosity (α) into the equation of state for pressure (P) [11], although they assumed symmetric collapse of pores. Shortly thereafter, Carroll and Holt implemented an analytical form of the α (porosity) term [34], and Butcher et al. incorporated deviatoric stress, work-hardening, initial pore size, and viscosity into the model, leading to the discovery of micro-inertial and viscous effects in delaying pore collapse [35]. Numerous theoretical, numerical, and experimental studies followed, which continued to improve the ability to describe the macroscopic response of porous materials under dynamic loads [15, 16, 33, 36, 37]. Yet, connecting the macroscale with the meso/microscales remains a challenge [33].

1.2.3 Mesoscopic Response

Experimental investigations of pore collapse at the mesoscale, or scale of the pores themselves, have only recently been undertaken. This area of focus began with the introduction of the hole closure experiment in which specimens with cylindrical holes are impacted to induce collapse of the hole. Initial experiments relied on post-mortem hole size measurements and inverse methods to estimate constitutive model parameters [38], while later work implemented phase contrast imaging to extract *in-situ* measurements of the hole geometry during collapse [24]. These early hole closure experiments were focused on constitutive modeling at high-strain rates, but further investigations observed indications of shear localization in Tantalum [39] and Ti-6Al-4V [20, 21]. Similar experiments were conducted on PMMA with spherical pores under a wide range of impact stresses which revealed hints of shear localization as well as clear evidence of cracking and jetting [17]. The work presented in this thesis serves to provide novel, *in-situ* quantitative measurements of pore collapse at the mesoscale which builds upon the aforementioned observations.

1.2.4 Bubble Collapse

The groundwork for the present pore collapse studies was laid in the fluid dynamics community through the shock-bubble interaction, or bubble collapse, experiments. Throughout this work, the bubble collapse literature has been a source of motivation for the methodology developed herein and has been instructive with respect to governing mechanisms and behaviors that are analogous between bubble collapse and pore collapse. Single bubble collapse experiments have revealed the development of many instabilities and vortices owing to shock interaction with the bubble geometry [40–43]. Shock interaction with spherical geometries notably creates concentrations in baroclinicity, which operates as the primary mechanism for vorticity generation during bubble collapse. Bubble collapse and cavity collapse experiments—essentially hole closure in gels, which are fluid-like in their mechanical response—on multiple bubbles or cavities demonstrated the importance of interactions between voids. Distinctly asymmetric collapse responses were observed for multiple voids [44–46] along with interactions occurring due to wave reflections, leading to both collapse-triggering and collapse-shielding events. These types of interactions, observed within approximately one void diameter spacing, suggest similar interactions to be significant in governing the collapse mechanics of pores in solids as well. However, there are relatively few studies that account for the strength of the material.

1.2.5 Diffraction of Shock Waves in Solids

At the heart of the pore collapse phenomenon is the three-dimensional interaction of a shock wave with a pore, or cavity inside a solid material. In the setting of elastic wave propagation, many closed form solutions have been developed for plane wave scattering or diffraction by various heterogeneities, including spherical and cylindrical cavities and inclusions [47–49] as well as slits or cracks [8, 50]. However, minimal experimental investigation of these interactions have been completed, and extension to shock wave propagation and diffraction is an entirely different matter, requiring numerical solutions rather than closed form solutions.

Experimental investigation of shock wave propagation in solids, and the corresponding deformation response of solids, have generally been restricted to one-dimensional, planar wave propagation [1, 10]. Important steps have been

taken to explore multi-dimensional loading, such as through the pressure shear plate impact (PSPI) experiment [51]. However, while the PSPI experiment captures the material response under decoupled longitudinal and shear loading, the loading remains inherently planar, via a planar longitudinal wave and a planar shear wave. Even in inhomogeneous solids such as composites or porous media, in which the initially-planar shock wave is diffracted by interaction with material interfaces, the experiments are conducted such that the shock wave becomes steady and approximately planar, and homogenized theories are implemented, enabling analysis of effective properties of those materials [52–56]. This has led to a state in which planar shock wave interaction with curved interfaces in solid materials is not well understood, both in terms of the diffraction behavior and the inhomogeneous deformation response of the material. Some notable exceptions exist, such as in the interaction of shock waves with cracks in the dynamic fracture setting [57], analytical investigation of shock wave diffraction in condensed matter [58], and local shock structure measurements in particulate composites [55, 59]. Overall, this remains an open area of research. This thesis will attempt to provide some insight into the effects of shock wave diffraction at solid-pore interfaces.

1.3 Experimental Techniques for Dynamic Compression

Throughout this thesis, two primary experimental platforms for dynamic compression are implemented: the split-Hopkinson (Kolsky) pressure bar (SHPB) [2] and the plate impact experiment [4]. These experiments enable dynamic compression at strain rates of $10^2 - 10^4\,\mathrm{s}^{-1}$ and $10^5 - 10^6\,\mathrm{s}^{-1}$, and under dynamic states of uniaxial stress and uniaxial strain, respectively. Traditional instrumentation for these techniques (strain gages and interferometers) and the corresponding analysis result in one dimensional measurements, which is suitable for high-fidelity material characterization under controlled loading states. However, in the case of the local response of two- or three-dimensional defects (e.g., holes or pores), the loading state and deformation modes become complex, requiring full-field measurements. Thus, the traditional experimental platforms are coupled with high-speed imaging and full-field visualization techniques such as digital image correlation (DIC) [60] and shadowgraphy [61]. These techniques are summarized below.

1.3.1 Split-Hopkinson (Kolsky) Pressure Bar

The split-Hopkinson pressure bar, also known as the Kolsky bar, is a commonly used experimental apparatus for dynamic characterization of materials [2, 3]. In this experiment, a small specimen of interest is compressed between two slender, elastic bars while strain measurements on the bars enable extraction of the macroscopic mechanical state (stress-strain) in the specimen at strain rates of $10^2 - 10^4\,\mathrm{s}^{-1}$. The technique is particularly useful for determining the dynamic strength of materials at intermediate- to high-strain rates. Figure 1.2 depicts the experimental setup with the addition of a high-speed camera used to visualize the deformation of the sample.

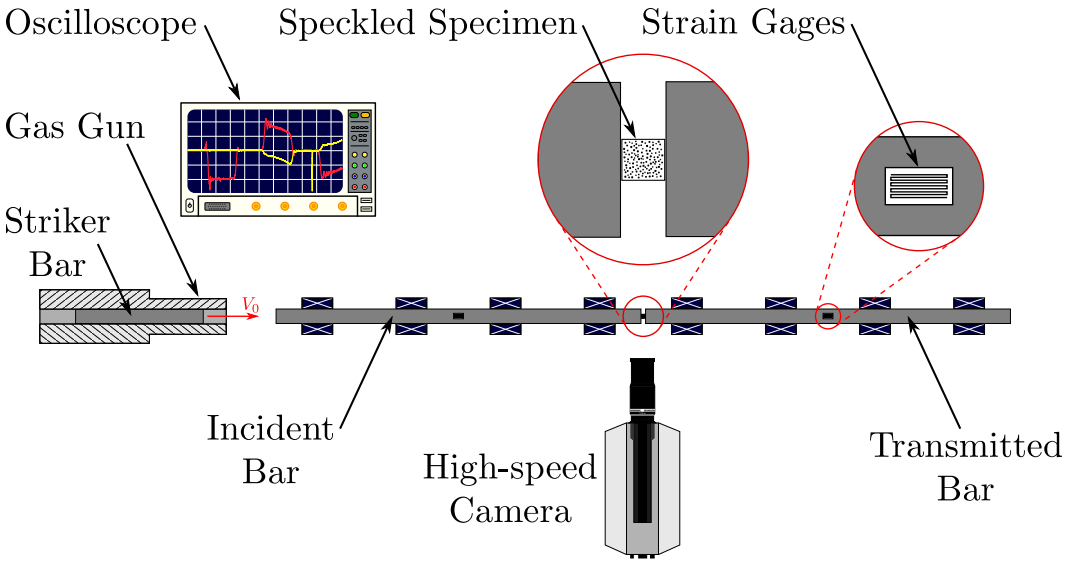

Figure 1.2: Split-Hopkinson (Kolsky) Pressure Bar experimental setup. The setup can be coupled with high-speed imaging and digital image correlation (DIC) for full-field quantitative visualization.

Dynamic compression in the sample is initiated by a striker bar, usually propelled by a gas gun, which impacts the incident bar and generates a stress wave that carries a finite-duration pulse (dictated by the striker bar wave speed and length). When the stress wave arrives at the bar-specimen interface, it partially transmits into the lower-impedance specimen and partially reflects. Inside the specimen, the wave reverberates between the two specimen-bar interfaces until dynamic equilibrium is achieved—generating a state of uniaxial stress in the specimen. The resulting stress waves which reflect back to the strain gage on the incident bar and transmit forward to the strain gage on the transmitted bar are measured via the induced strain in the bars. Finally,

one dimensional elastic wave analysis is leveraged to extract the bar-specimen interface velocities and the force in the transmitted bar, which are used to calculate the macroscopic strain and stress, respectively, through one dimensional wave analysis.

In this study, the SHPB experimental setup is used in Chapter 2 for validation of the internal DIC technique on transparent PMMA, before translating the DIC technique to plate impact experiments.

1.3.2 Plate Impact

The plate impact experiment is a conventional technique for shock compression studies, used extensively for material characterization at high-strain rates ($10^5 - 10^6\,\mathrm{s}^{-1}$) and pressures up to 1 TPa. The experiment consists of launching a flyer plate which impacts a target plate at high speeds, ranging from $0.1 - 10\,\mathrm{km/s}$ [62], and generates a planar shock wave upon impact [1, 4, 5], as depicted in Fig. 1.3. While the SHPB experiments maintained a state of uniaxial stress, plate impact experiments impose a state of uniaxial strain due to lateral confinement, which is achieved through the sample geometry. When the shock wave transits the sample thickness, release waves initiate from the outer boundary of the sample, propagating radially inward toward the sample center. Prior to the arrival of these boundary release waves, the material is laterally confined by the surrounding material; thus, measurements are typically taken at the center of the sample free surface—the location at which boundary waves arrive the latest—and target plate geometries are designed to optimize the duration of confinement. Typically, free surface velocity measurements are conducted using interferometric techniques such as VISAR [63] or photonic Doppler velocimetry (PDV) [64], although embedded stress gauges have also been implemented [65]. The plate impact experiment has been used in many modified forms to extract pressure-dependent measurements of material properties such as: equation of state (EOS), dynamic strength, phase transformations, spall strength, and wave speeds [1]. In this work, normal plate impact experiments are utilized to generate a controlled, planar shock wave in the target specimen, which subsequently interacts with the embedded pore(s) and drives pore collapse.

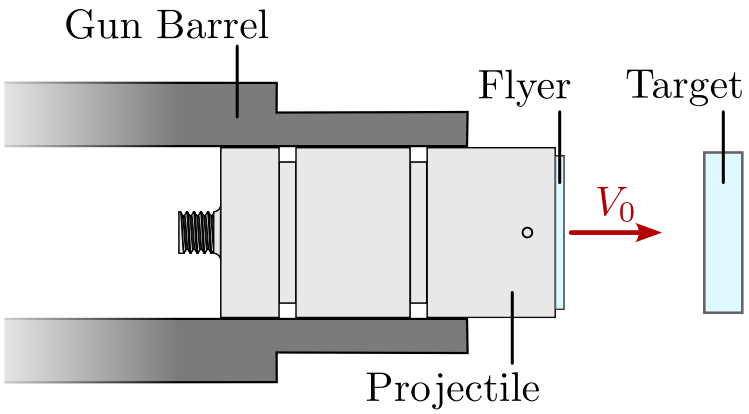

Figure 1.3: Normal plate impact experimental setup. Depicted is the projectile assembly (projectile and flyer plate) exiting the gun barrel at impact velocity, V_0, to impact the target plate.

1.3.3 Digital Image Correlation (DIC)

Digital image correlation (DIC) is a widely used quantitative visualization technique in solid mechanics, particularly valued for its non-invasive, complete characterization of in-plane deformations [60, 66]. The technique is illustrated in Fig. 1.5. In general, DIC requires the application of a grayscale speckle pattern to the surface of the solid object of interest, which is then tracked via images of the solid body before and during deformation. To postprocess the images, the undeformed (reference) image is segmented into subsets, typically at least 9x9 pixels in size to ensure each subset possesses a unique grayscale identifier (the combination of grayscale values of all pixels inside the subset). These subsets are subsequently used in pattern matching algorithms to map the deformed speckle pattern back to the original undeformed pattern. This mapping provides a measurement of the full displacement field in the image. There are several algorithms available through commercial and non-commercial software codes to characterize the full-field displacement. The measured displacements can then be used to compute strains and particle velocities for mechanical analysis of the deformation. By providing full-field strain measurements, DIC enables characterization of complex deformation fields which has previously been unattainable through classical point-wise, one-dimensional measurements. While the earliest applications of DIC were for quasi-static deformation, it has seen increasing use, via high-speed imaging, in dynamic settings [27, 67, 68] and has recently been extended to the shock compression domain [59, 69]. This technique is implemented in this work, and

further extended to capture deformation fields surrounding collapsing pores inside of solid materials.

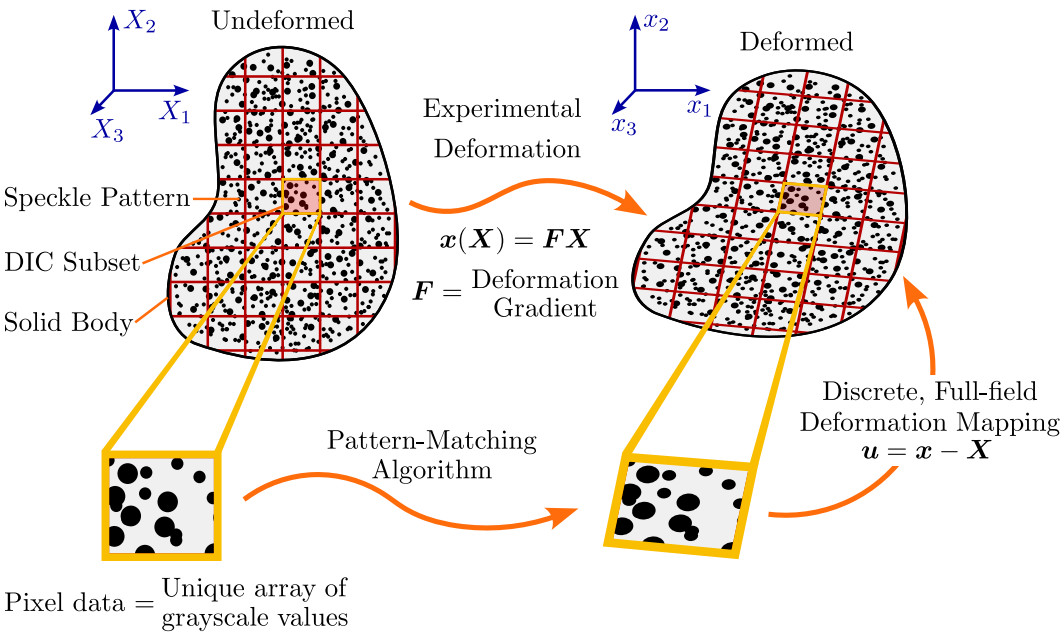

Figure 1.4: Schematic of digital image correlation (DIC) technique. The deformation of a speckled body is illustrated, along with the corresponding deformation measurement process.

1.3.4 Shadowgraphy

Shadowgraphy is a qualitative imaging technique for use in transparent media, which highlights variance in material density through its sensitivity to the second spatial gradient of refractive index [61]. The technique typically utilizes collimated light shining through the medium of interest and onto a screen or into a camera. In a perfectly homogeneous medium, the image would be uniformly illuminated. However, when a material interface exists or density disturbance occurs, light deflects at the interface with large density gradient. The deflected light subsequently creates regions of higher and lower light intensity—bright spots and shadows—on the screen or camera sensor. These shadows can then be identified in the images and related to physical features with large density disturbances during the experiment. In this work, shadowgraphy is leveraged to identify shear bands and cracks during the pore collapse process.

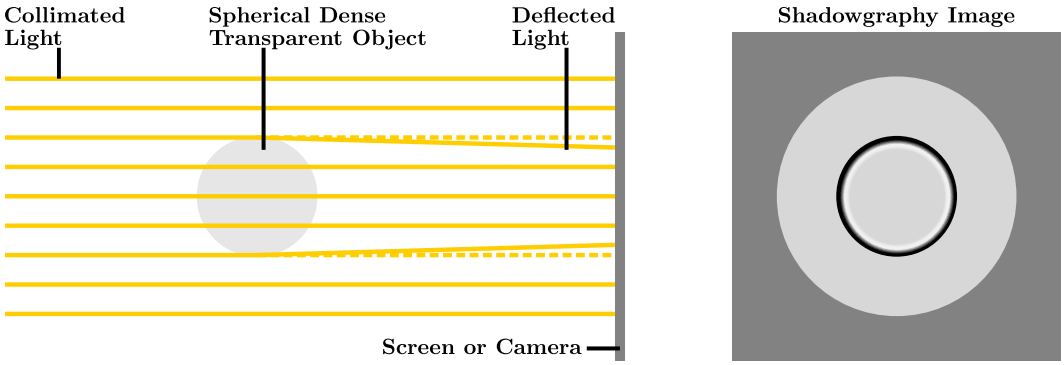

Figure 1.5: Illustration of shadowgraphy operating principle as described by Settles [61]. Deflected light at the boundary of the object casts a shadow onto the image at its boundary.

1.4 Scope of Thesis

The primary goal of this thesis is to realize spatio-temporal characterization of shock-induced pore collapse via full-field, quantitative high-speed imaging. To accomplish this, plate impact experiments are utilized as the platform to drive collapse of embedded pores in transparent target plates. Digital image correlation (DIC) and shadowgraphy are implemented for quantitative and qualitative visualization, respectively, of the collapsing pore and associated material response around the pore. Because pore collapse occurs under shock loading with lateral confinement, the spherical pores must be internally embedded and visualization must be conducted at an internal plane as well. Thus, before investigating the pore collapse phenomenon, an internal DIC technique is developed for use in dynamic laboratory experiments and is validated in both SHPB and plate impact experiments in Chapter 2.

After developing the necessary techniques to study pore collapse in the aforementioned manner, one must confront the multiphysics nature of the pore collapse problem which includes strongly coupled mechanical, thermal, and chemical influences [25, 33]. This concept is sketched in Fig. 1.6 which identifies many phenomena associated with pore collapse that are coupled, to different degrees, to these three disciplines. For the purposes of this work, one chooses to focus on mechanically-driven phenomena and to perform strictly mechanical measurements. Further, the scope is restricted to thermo-mechanical phenomena by working with an inert solid, namely PMMA, which has no known phase transition in the impact stress regime of interest. In this setting, the primary thermo-mechanical coupling is through plastic heating which intro-

duces competition between thermal softening, strain hardening, and strain rate hardening, particularly in the context of adiabatic shear localization [9]. The possibility of adiabatic shear localization has strong implications for structural integrity of engineered components and for mechanically-induced hot spot generation in porous energetic materials, which will be discussed in the ensuing chapters.

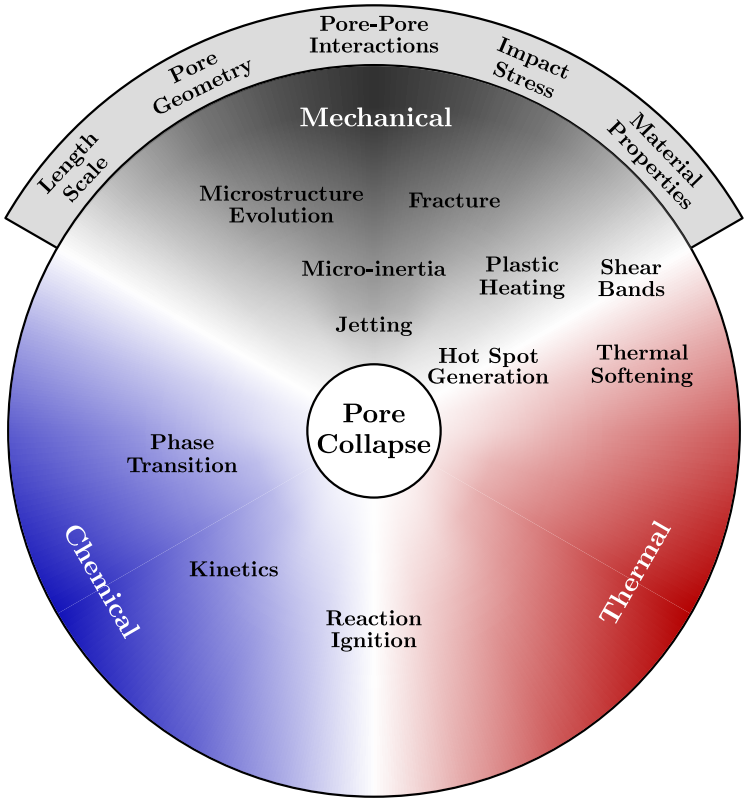

Figure 1.6: Multiphysics nature of pore collapse problem, including strong mechanical, thermal, and, especially in the case of energetic materials, chemical effects. Important phenomena are listed inside the circle, with relevant, driving mechanical contributions listed across the top banner.

Thus, the scope is reduced to a manageable context: measurements of pore geometry evolution, deformation surrounding collapsing pores, and associated failure mechanisms. One sets out to investigate behaviors such as the rate and extent of pore collapse, strain concentrations surrounding shocked pores, possible localization through jetting or adiabatic shear banding, and fracture. It is expected that these deformation responses are driven by various mechanical parameters, such as those set across the top banner of Fig. 1.6.

The role of impact stress—varied across the strength-dominated regime—and pore-pore interactions are of greatest interest for this study. Other parameters are fixed, in some cases for physical reasons and others for practical purposes. For the constitutive material, PMMA is selected as a model material which is a common engineering material, a good simulant for energetic materials, and has minimal complicating microstructural effects to consider. It also has desirable experimental properties of being transparent under shock and easily manufacturable. For the best comparison to real porous media, spherical pores are chosen in favor of cylindrical holes, and the length scale is set to $800\,\mu$m to achieve minimal pore size while maintaining manufacturability and working within experimental resolution limitations. Fixing these parameters enables one to probe the role of impact stresses across the strength-dominated regime from $0.4-1.0\,$GPa, where collapse is more strongly resisted and unique deformation and failure modes arise. Further, investigation of pore arrays is undertaken to improve understanding of real porous media which consist of neighboring pores and porous networks.

The thesis outline is as follows: Chapter 2 develops and validates the high-speed internal DIC technique across uniaxial stress and uniaxial strain dynamic experiments, Chapter 3 investigates the deformation and failure modes during the collapse of a single spherical pore in PMMA, and Chapter 4 considers the collapse of pore arrays and associated interactions between pores. Final concluding remarks are given in Chapter 5 along with discussion of future directions and open areas of research.

References

[1] M. A. Meyers, *Dynamic behavior of materials* (John Wiley & Sons, Ltd, Sept. 1994).

[2] H. Kolsky, "An investigation of the mechanical properties of materials at very high rates of loading," Proceedings of the Physical Society. Section B **62**, 676–700 (1949).

[3] W. W. Chen and B. Song, *Split Hopkinson (Kolsky) bar: Design, testing and applications* (Springer Science & Business Media, 2010).

[4] M. Rice, R. G. McQueen, and J. Walsh, "Compression of solids by strong shock waves," Solid State Physics **6**, 1–63 (1958).

[5] K. T. Ramesh, "High rates and impact experiments," in *Springer handbook of experimental solid mechanics* (Springer, 2008), pp. 929–960.

[6] D. Sinars, M. Sweeney, C. Alexander, D. Ampleford, T. Ao, J. Apruzese, C. Aragon, D. Armstrong, K. Austin, T. Awe, et al., "Review of pulsed power-driven high energy density physics research on Z at sandia," Physics of Plasmas **27**, 070501 (2020).

[7] R. Trainor, J. Shaner, J. Auerbach, and N. Holmes, "Ultrahigh-pressure laser-driven shock-wave experiments in aluminum," Physical Review Letters **42**, 1154 (1979).

[8] L. B. Freund, *Dynamic fracture mechanics* (Cambridge University Press, 1990).

[9] Y. L. Bai and B. Dodd, *Adiabatic shear localization: Occurrence, theories, and applications* (Pergamon Press, London, 1992).

[10] L. Davison, *Fundamentals of shock wave propagation in solids* (Springer, Berlin Heidelberg, 2008).

[11] W. Herrmann, "Constitutive equation for the dynamic compaction of ductile porous materials," Journal of Applied Physics **40**, 2490–2499 (1969).

[12] F. Lu, S. Huan, and J. Ding, "Viscoplasticity and porosity effects on the shock propagation in PMMA and porous aluminum oxide," AIP Conference Proceedings **309**, 1013–1015 (1994).

[13] S. Bonnan, P.-L. Hereil, and F. Collombet, "Experimental characterization of quasi static and shock wave behavior of porous aluminum," Journal of Applied Physics **83**, 5741–5749 (1998).

[14] E. Chiu, A. Needleman, S. Osovski, and A. Srivastava, "Mitigation of spall fracture by evolving porosity," Mechanics of Materials **184**, 104710 (2023).

[15] C. Czarnota, A. Molinari, and S. Mercier, "The structure of steady shock waves in porous metals," Journal of the Mechanics and Physics of Solids **107**, 204–228 (2017).

[16] Z. Lovinger, C. Czarnota, S. Ravindran, A. Molinari, and G. Ravichandran, "The role of micro-inertia on the shock structure in porous metals," Journal of the Mechanics and Physics of Solids **154**, 10.1016/j.jmps.2021.104508 (2021).

[17] E. M. Escauriza, J. P. Duarte, D. J. Chapman, M. E. Rutherford, L. Farbaniec, J. C. Jonsson, L. C. Smith, M. P. Olbinado, J. Skidmore, P. Foster, T. Ringrose, A. Rack, and D. E. Eakins, "Collapse dynamics of spherical cavities in a solid under shock loading," Scientific Reports **10**, 10.1038/s41598-020-64669-y (2020).

[18] N. K. Rai, E. M. Escauriza, D. E. Eakins, and H. S. Udaykumar, "Mechanics of shock induced pore collapse in poly(methyl methacrylate) (PMMA): Comparison of simulations and experiments," Journal of the Mechanics and Physics of Solids **143**, 10.1016/j.jmps.2020.104075 (2020).

[19] B. P. Lawlor, V. Gandhi, and G. Ravichandran, "Full-field quantitative visualization of shock-driven pore collapse and failure modes in PMMA," Journal of Applied Physics **136**, 225901 (2024).

[20] Z. Lovinger and R. Kositski, "Shear localization as a damage mechanism in pore collapse under shock compression," International Journal of Impact Engineering **193**, 10.1016/j.ijimpeng.2024.105039 (2024).

[21] J. Lind, M. Nelms, M. Kumar, and N. Barton, "Observation of shear band localization in Ti-6Al-4V through in-situ imaging under dynamic compression conditions," in AIP Conference Proceedings, Vol. 3066, 1 (AIP Publishing, 2024).

[22] R. G. Kraus, D. J. Chapman, W. G. Proud, and D. C. Swift, "Hugoniot and spall strength measurements of porous aluminum," Journal of Applied Physics **105**, 10.1063/1.3133237 (2009).

[23] Z. Lovinger, C. Czarnota, S. Ravindran, C. Kettenbeil, A. Molinari, and G. Ravichandran, "Shock structure and spall behavior of porous aluminum," in AIP Conference Proceedings, Vol. 2272 (Nov. 2020).

[24] J. Lind, M. D. Nelms, A. K. Robinson, M. Kumar, and N. R. Barton, "Examining material constitutive response under dynamic compression and large plastic strains using in situ imaging of hole closure," Acta Materialia **206**, 10.1016/j.actamat.2020.116584 (2021).

[25] M. R. Baer, "Modeling heterogeneous energetic materials at the mesoscale," Thermochimica Acta **384**, 351–367 (2002).

[26] R. Cunningham, A. Nicolas, J. Madsen, E. Fodran, E. Anagnostou, M. D. Sangid, and A. D. Rollett, "Analyzing the effects of powder and post-processing on porosity and properties of electron beam melted Ti-6Al-4V," Materials Research Letters **5**, 516–525 (2017).

[27] J. S. Weeks, V. Gandhi, and G. Ravichandran, "Shock compression behavior of stainless steel 316L octet-truss lattice structures," International Journal of Impact Engineering **169**, 104324 (2022).

[28] K.-I. Kondo, S. Soga, A. Sawaoka, and M. Araki, "Shock compaction of silicon carbide powder," Journal of Materials Science **20**, 1033–1048 (1985).

[29] P. S. DeCarli and J. C. Jamieson, "Formation of diamond by explosive shock," Science **133**, 1821–1822 (1961).

[30] R. A. Graham and A. B. Sawaoka, *High pressure explosive processing of ceramics* (Trans Tech Publications Ltd, 1987).

[31] N. N. Thadhani, "Shock-induced chemical reactions and synthesis of materials," Progress in Materials Science **37**, 117–226 (1993).

[32] R. Prummer, *Explosive compaction of powders and composites* (CRC Press, 2006).

[33] L. Davison, Y. Horie, and M. Shahinpoor, *High-pressure shock compression of solids iv*, edited by L. Davison, Y. Horie, and M. Shahinpoor (Springer, New York, 1997).

[34] M. M. Carroll and A. C. Holt, "Static and dynamic pore-collapse relations for ductile porous materials," Journal of Applied Physics **43**, 1626–1636 (1972).

[35] B. M. Butcher, M. M. Carroll, and A. C. Holt, "Shock-wave compaction of porous aluminum," Journal of Applied Physics **45**, 3864–3875 (1974).

[36] W. Tong and G. Ravichandran, "Dynamic pore collapse in viscoplastic materials," Journal of Applied Physics **74**, 2425–2435 (1993).

[37] C. Czarnota, S. Mercier, and A. Molinari, "Modelling of nucleation and void growth in dynamic pressure loading, application to spall test on tantalum," International Journal of Fracture **141**, 177–194 (2006).

[38] V. S. Glazkov, O. N. Ignatova, A. N. Malyshev, S. S. Nadezhin, A. M. Podurets, V. A. Raevsky, and O. A. Tyupanova, "Peculiarities of high-rate deformation of copper upon convergence of cylindrical channels by action of shock waves," in AIP Conference Proceedings, Vol. 1195 (2009), pp. 735–738.

[39] M. Nelms, J. Lind, J. Margraf, S. B. Qamar, J. Herrington, A. Robinson, M. Kumar, and N. Barton, "High-rate strength response of tantalum from dynamic hole closure experiments," Journal of Applied Physics **132**, 10.1063/5.0107391 (2022).

[40] G. H. Markstein, "A shock-tube study of flame front-pressure wave interaction," Symposium (International) on Combustion **6**, Sixth Symposium (International) on Combustion, 387–398 (1957).

[41] G. Rudinger, "Shock wave and flame interactions," in Combustion and propulsion, third agard colloquium (Pergamon Press, London, 1958), pp. 153–182.

[42] J. F. Haas and B. Sturtevant, "Interaction of weak shock waves with cylindrical and spherical gas inhomogeneities," Journal of Fluid Mechanics **181**, 41–76 (1987).

[43] J. J. Quirk and S. Karni, "On the dynamics of a shock–bubble interaction," Journal of Fluid Mechanics **318**, 129–163 (1996).

[44] Y. Tomita, A. Shima, and T. Ohno, "Collapse of multiple gas bubbles by a shock wave and induced impulsive pressure," Journal of Applied Physics **56**, 125–131 (1984).

[45] J. P. Dear and J. E. Field, "A study of the collapse of arrays of cavities," Journal of Fluid Mechanics **190**, 409–425 (1988).

[46] A. B. Swantek and J. M. Austin, "Collapse of void arrays under stress wave loading," Journal of Fluid Mechanics **649**, 399–427 (2010).

[47] C. Ying and R. Truell, "Scattering of a plane longitudinal wave by a spherical obstacle in an isotropically elastic solid," Journal of Applied Physics **27**, 1086–1097 (1956).

[48] M. Chao-Chow and P. Yih-Hsing, "The diffraction of elastic waves and dynamic stress concentrations," The Rand Corporation (1971).

[49] R.-S. Wu and K. Aki, "Scattering characteristics of elastic waves by an elastic heterogeneity," Geophysics **50**, 582–595 (1985).

[50] J. Achenbach, *Wave propagation in elastic solids* (Elsevier, 1973).

[51] R. Clifton and R. Klopp, "Pressure shear plate impact testing," in *Metals handbook*, Vol. 8 (American Society for Metals, 1985), pp. 230–239.

[52] R. R. Boade, "Compression of porous copper by shock waves," Journal of Applied Physics **39**, 5693–5702 (1968).

[53] F. Collombet, S. Bonnan, and P. L. Héreil, "A mesomechanical modelling of porous aluminum under dynamic loading: Comparison experiment-calculation," Journal De Physique. IV : JP **7**, 10.1051/jp4:19973110 (1997).

[54] J. L. Jordan, L. Ferranti, R. A. Austin, R. D. Dick, J. R. Foley, N. N. Thadhani, D. L. McDowell, and D. J. Benson, "Equation of state of aluminum-iron oxide-epoxy composite," Journal of Applied Physics **101**, 093520 (2007).

[55] M. B. Rauls and G. Ravichandran, "Structure of shock waves in particulate composites," Journal of Applied Physics **127**, 10.1063/1.5125449 (2020).

[56] D. B. Bober, E. B. Herbold, Y. Toyoda, B. Maddox, and M. Kumar, "A description of structured waves in shock compressed particulate composites," Journal of Applied Physics **127**, 10.1063/5.0002425 (2020).

[57] G. Ravichandran and R. Clifton, "Dynamic fracture under plane wave loading," International Journal of Fracture **40**, 157–201 (1989).

[58] A. Gonor, J. Gottlieb, and I. Hooton, "Shock wave diffraction over wedges, cylinders, and spheres in gases, liquids, and condensed matter," Journal of Applied Physics **95**, 1577–1585 (2004).

[59] S. Ravindran, V. Gandhi, B. Lawlor, and G. Ravichandran, "Mesoscale shock structure in particulate composites," Journal of the Mechanics and Physics of Solids **174**, 10.1016/j.jmps.2023.105239 (2023).

[60] M. A. Sutton, J. J. Orteu, and H. Schreier, *Image correlation for shape, motion and deformation measurements: Basic concepts, theory and applications* (Springer US, 2009), pp. 1–321.

[61] G. S. Settles, *Schlieren and shadowgraph techniques: Visualizing phenomena in transparent media* (Springer Science & Business Media, 2001).

[62] X. Wang, C. Dai, Q. Wang, L. Hao, J. Bai, Y. Yu, Q. Wu, H. Tan, J. Hu, G. Luo, Q. Shen, and L. Zhang, "Development of a three-stage gas gun launcher for ultrahigh-pressure hugoniot measurements," Review of Scientific Instruments **90**, 013903 (2019).

[63] L. Barker and R. Hollenbach, "Laser interferometer for measuring high velocities of any reflecting surface," Journal of Applied Physics **43**, 4669–4675 (1972).

[64] O. T. Strand, D. R. Goosman, C. Martinez, T. L. Whitworth, and W. W. Kuhlow, "Compact system for high-speed velocimetry using heterodyne techniques," Review of Scientific Instruments **77**, 083108 (2006).

[65] Z. Rosenberg and Y. Partom, "Lateral stress measurement in shock-loaded targets with transverse piezoresistance gauges," Journal of Applied Physics **58**, 3072–3076 (1985).

[66] M. Sutton, W. Wolters, W. Peters, W. Ranson, and S. McNeill, "Determination of displacements using an improved digital correlation method," Image and Vision Computing **1**, 133–139 (1983).

[67] P. Malchow, B. Koohbor, S. Ravindran, and A. Kidane, "In-situ quantification of intra and intergranular deformation in pure magnesium using full-field measurements at low and high strain rates," Mechanics of Materials **126**, 36–46 (2018).

[68] P. L. Reu and T. J. Miller, "The application of high-speed digital image correlation," The Journal of Strain Analysis for Engineering Design **43**, 673–688 (2008).

[69] S. Ravindran, V. Gandhi, A. Joshi, and G. Ravichandran, "Three-dimensional full-field velocity measurements in shock compression experiments using stereo digital image correlation," Review of Scientific Instruments **94**, 10.1063/5.0131590 (2023).

Chapter 2

INTERNAL DIGITAL IMAGE CORRELATION FOR DYNAMIC EXPERIMENTS

B.P. Lawlor, V. Gandhi, and G. Ravichandran, "An internal digital image correlation technique for high-strain rate dynamic experiments," Experimental Mechanics **65**, 407-409 (2025)

Contributions: B.P.L. developed the methodology, performed the experiments, prepared the experimental data, and wrote the manuscript.

Abstract

Background: Full-field, quantitative visualization techniques, such as digital image correlation (DIC), have unlocked vast opportunities for experimental mechanics. However, DIC has traditionally been a surface measurement technique, and has not been extended to perform measurements on the interior of specimens for dynamic, full-scale laboratory experiments. This limitation restricts the scope of physics which can be investigated through DIC measurements, especially in the context of heterogeneous materials.

Objective: The focus of this study is to develop a method for performing internal DIC measurements in dynamic experiments. The aim is to demonstrate its feasibility and accuracy across a range of stresses (up to 650 MPa), strain rates (10^3-$10^6\,\mathrm{s}^{-1}$), and high-strain rate loading conditions (e.g., ramped and shock wave loading).

Methods: Internal DIC is developed based on the concept of applying a speckle pattern at an inner-plane of a transparent specimen. The high-speed imaging configuration is coupled to the traditional dynamic experimental setups, and is focused on the internal speckle pattern. During the experiment, while the sample deforms dynamically, in-plane, two-dimensional deformations are measured via correlation of the internal speckle pattern. In this study, the

viability and accuracy of the internal DIC technique is demonstrated for split-Hopkinson (Kolsky) pressure bar (SHPB) and plate impact experiments.

Results: The internal DIC experimental technique is successfully demonstrated in both the SHPB and plate impact experiments. In the SHPB setting, the accuracy of the technique is excellent throughout the deformation regime, with measurement noise of approximately 0.2% strain. In the case of plate impact experiments, the technique performs well, with error and measurement noise of 1% strain.

Conclusion: The internal DIC technique has been developed and demonstrated to work well for full-scale dynamic high-strain rate and shock laboratory experiments, and the accuracy is quantified. The technique can aid in investigating the physics and mechanics of the dynamic behavior of materials, including local deformation fields around dynamically loaded material heterogeneities.

2.1 Introduction

Traditional non-contacting, qualitative imaging techniques, such as conventional imaging, shadowgraphy, schlieren [1], and others have played a significant role in understanding the occurrence of many general mechanics phenomena, including characterizing deformation and failure mechanisms. However, these methods are inadequate to quantitatively capture local details of deformations. Full-field, quantitative imaging techniques have revolutionized the fields of experimental mechanics and mechanical behavior of materials, providing detailed insight into the stress or strain fields, especially in those experiments with complicated, non-uniform deformations. Some popular techniques have included photoelasticity [2], coherent gradient sensing (CGS) [3], and digital image correlation (DIC) [4–6], which provide powerful complements to traditional pointwise interferometric and other measurement techniques. DIC, which is currently the most popular choice among the mechanics community, is a methodology used to extract full-field displacement measurements based on pattern matching between grayscale images of the deformed and undeformed state of an object with a speckled surface [6]. While traditionally focused on quasi-static strain rates, recent advances in high-speed camera technology have enabled accurate implementation of DIC during high-strain rate dynamic experiments [7–11], and most recently has been extended to the shock com-

pression regime via full-field free surface velocity measurements [12]. True to its intended purpose of measuring spatially varying deformations, the DIC technique for shock compression experiments has even been utilized to study the non-uniform shock structuring arising in plate impact experiments on particulate composite materials [13]. Yet, it is recognized that there remains a need in the study of heterogeneous materials for *in-situ* characterization of the dynamic deformation field at the source of the heterogeneity—i.e., at the material boundary/interface and at the length scale of the heterogeneity itself. These boundaries/interfaces have often been found to be the location of failure via delamination [14], fracture [15], dynamic instabilities (e.g., jetting [16, 17]), shear localization [18], etc. Hence, accurate characterization of the deformation evolution at these boundaries is critical. Since these boundaries, such as those associated with defects (e.g., voids/pores and inclusions), are predominantly located inside of the matrix material, a DIC technique that enables these difficult measurements to be performed under dynamic loading conditions is much in need. Furthermore, for the purpose of capturing features at the small length scale of these heterogeneities, high-magnification imaging for this technique is often desired. Of particular interest are the problems of pore collapse and interaction between particles/fibers and matrix in composites. Besides use on heterogeneous materials, this technique would also be relevant for unraveling the three dimensional nature of experiments. Such scenarios, in which internal deformation measurements would be especially useful, include: (i) the state of deformation is neither plane strain nor plane stress, (ii) the physics of interest must be studied under confinement (e.g., lateral confinement of plate impact experiments), and (iii) the mechanics problem is sensitive to boundary effects. One interesting example is the study of internal crack propagation and interaction with the free surface.

While DIC is traditionally a surface measurement, the internal DIC concept has been previously applied in a few investigations. Berfield et al. were the first to demonstrate internal DIC in the quasi-static regime, and did so across the nm to μm length scales [19]. They developed a methodology for internal DIC in polymers, demonstrated its accuracy, and applied it to investigate the deformation fields around silica micro-spheres embedded inside an elastomer. In addition, internal DIC has been implemented in the dynamic strain rate regime for different loading conditions. For example, Huang et al. [20] conducted plate impact experiments in conjuction with internal DIC to study

properties of a failure wave in PMMA, though the accuracy of the technique was not verified. Recently, internal DIC has also been developed for dynamic visualization of laser-induced cavitation experiments in gels [21], for which the specimen is dynamically loaded while situated under a microscope.

The previous dynamic internal DIC endeavors have been restricted by the absence of comparison to ground truth data for the purpose of evaluating the techniques. Additionally, the experimental platforms have limited the physics which are accessible for investigation. This work addresses these issues by developing an internal DIC framework for use in traditional dynamic experiments such as split-Hopkinson (Kolsky) pressure bar (SHPB) and plate impact experiments, which possess well-prescribed loading conditions (uniaxial stress and uniaxial strain, respectively). This provides a suitable deformation (strain) state for comparison, against which the error is quantified. Additionally, the experimental setups used are general and adaptable to many loading conditions depending on the problem being addressed. Further, the internal DIC technique is not limited to these two experimental setups, but can be implemented in many full-scale laboratory experiments and should be applicable for optically transparent materials of interest.

The experimental setup is discussed in Section 2.2, with application to SHPB and plate impact experiments. In Section 2.3, validation experiments for both experimental setups are presented, the accuracy of the approach and corresponding experimental noise are quantified, and possible sources of error are identified. Finally, concluding remarks and future directions are given in Section 2.4.

2.2 Materials and Methods

The premise of the proposed internal DIC technique is to manufacture transparent target specimens with an internally embedded speckle pattern. Next, a series of deformation images are captured during dynamic compression of these target specimens using a high-speed imaging setup configured to visualize the internal speckle pattern through the transparent target. These images capture the in-plane displacements, which are computed through DIC, and strains, which are subsequently calculated from the displacement measurements. In this study, a series of split-Hopkinson (Kolsky) pressure bar (SHPB) [22] and plate impact [23] experiments were conducted to demonstrate the in-

ternal DIC framework, and comparisons were made with experimental and theoretical measures to quantify the accuracy of the method.

2.2.1 Sample Preparation

For the experiments presented, three different target specimen configurations were utilized, which are depicted in Fig. 3.1. Each sample was manufactured from stock PMMA material obtained from E&T Plastics (Long Island City, New York). Figure 3.1a shows a classical cubic sample used for SHPB experiments, for which the speckle pattern is applied to the external surface. This sample type is denoted as "bulk." Samples in Fig. 3.1b-c are used for internal DIC, and are manufactured out of two separate half-samples which are speckled and glued together, and will be called "inner-plane" samples.

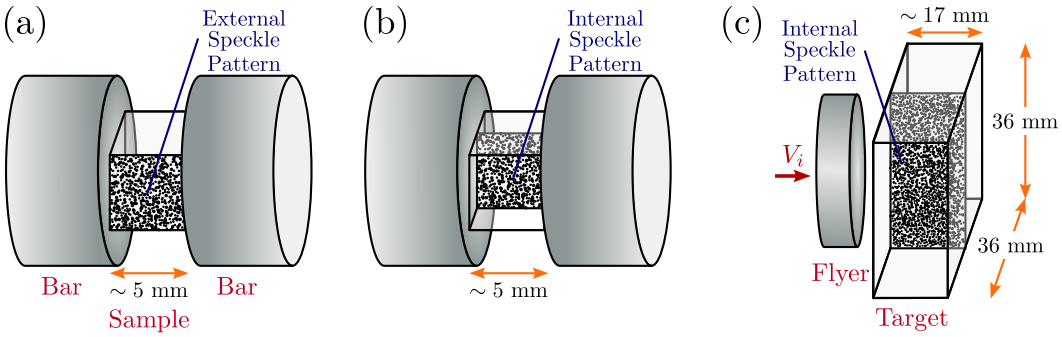

Figure 2.1: Specimen geometries: (a) Bulk cubic SHPB specimen which provides ground truth comparison. (b) Inner-plane cubic SHPB specimen used to validate the internal DIC technique. (c) Plate impact inner-plane specimen used to capture the shock response in PMMA and assess the accuracy of the internal DIC technique.

The half-samples for inner-plane specimens shown in Fig. 3.1b-c are carefully lapped together in pairs to ensure identical dimensions, which aids precise gluing. Lapping also creates flat surfaces at the glue interface and load/impact surface, which are crucial to ensure a strong glue bond, uniform loading (for SHPB), and planar shock structure (for plate impact) during the experiments. Additionally, the half-sample surfaces are polished along the visualization direction to create maximum transparency for imaging. A speckle pattern, discussed in Section 2.2.4, is then applied to the inner surface of one half-sample and allowed to dry for 24 hours, after-which the two pieces are sandwiched together with a thin layer of two-part epoxy glue, EpoxAcast 690 from SmoothOn (Macungie, Pennsylvania), at the speckle interface. The samples are precisely

aligned using a confining apparatus, and weighed down to squeeze out air bubbles and excess glue. After the glue has set for the manufacturer-specified 24 hours, the weights are removed and the sample is taken out of the confining apparatus. Excess glue is removed from the sides of the sample, and the intact sample surfaces are re-lapped in the load/impact direction until the variation in thickness measurements is below $50\,\mu$m for SHPB specimens, which ensures uniform load in the sample and improves repeatability of experiments. For plate impact specimens, the restriction is tightened to require less than $20\,\mu$m thickness variation, and the surface flatness, as measured by Fizeau rings under monochromatic light, is required to be less than $1\,\mu$m. These specifications ensure that a planar shock wave is generated upon impact during the plate impact experiments. Final assembled SHPB samples are approximately $5 \times 5 \times 5$ mm cubes, while plate impact samples are 36×36 mm square plates with approximately 17 mm thickness. It is worth noting that the aforementioned glue was selected for its strong bonding properties while possessing similar mechanical properties to PMMA. Alternatively, for soft materials, the glue must be chosen carefully to avoid introducing a stiffening effect if the modulus of the glue exceeds that of the base material.

For plate impact experiments, circular flyer plates made of aluminum 7075 are also prepared, with typical dimensions of 35 mm diameter and 13 mm thickness. They are similarly lapped until they satisfy requirements of less than $10\,\mu$m thickness variation and less than $0.5\,\mu$m surface flatness on the impact side of the flyer.

Electrical shorting pins are utilized in plate impact experiments to trigger diagnostics upon impact and simultaneously measure impact tilt (planarity). After the target has been prepared as described above, tilt pins are glued into four holes which correspond with the perimeter of the flyer. After gluing, these pins are sanded down and the surface is lapped one final time to ensure the pins are flush with the impact surface. Next, the pins are wired into a digital logic circuit whose output is connected to a high-speed digital oscilloscope, and the target is mounted onto the target holder, which is affixed to a six-degree-of-freedom gimbal. Lastly, the assembly is transferred to the vacuum chamber to begin the alignment process.

2.2.2 Split-Hopkinson Pressure Bar Experimental Setup

High-strain rate experiments were conducted using the split-Hopkinson pressure bar (SHPB) experimental apparatus [24]. The technique relies upon the propulsion of a striker bar using a pressurized gas gun, which impacts an incident bar and generates a stress wave. The wave propagates through the incident bar into the sample, which is sandwiched between the incident and transmitted bars, and reverberates inside the sample. When using the appropriate bar material and sample geometry, dynamic equilibrium is quickly achieved. This enables traditional analysis of the sample's mechanical state via strain gage measurements on the bars, leveraging elastic wave theory and the assumption of force balance, i.e., specimen equilibrium [23]. For this work, the conventional SHPB experimental apparatus is complemented by a high-speed imaging setup, which is configured to capture deformation images of the sample, which is depicted in Fig. 2.2. Post-processing of the deformation images via DIC enables extraction of the strain evolution in the sample. The strain gage measurement system and high-speed imaging are simultaneously triggered when the stress wave is detected by the strain gages on the incident bar.

In this work, aluminum 7075 bars are used, with the striker bar measuring 0.46 m in length, incident and transmitted bars both having a length of 1.83 m; all with diameter 19.05 mm. Two strain gages, Omega SGD-2D/350-LY11 (Norwalk, Connecticut), are mounted at the midpoint of each bar (diametrically opposed to one another, to average out any bending strains), the voltage signal is conditioned by a Vishay 2310B signal conditioning amplifier (Malvern, Pennsylvania), and the signal is recorded with a four-channel, 1 GHz, Agilent MSO-X 4104A digital oscilloscope (Santa Clara, California). The high-speed imaging setup is composed of a Shimadzu HPV-X2 camera (Kyoto, Japan) equipped with an 100 mm Tokina AT-X Pro lens (Tokyo, Japan) and a Cavitar Cavilux incoherent laser illumination source (Tampere, Finland), which is setup to visualize the sample during dynamic compression. Details of the DIC speckle pattern and analysis are provided in Section 2.2.4.

2.2.3 Plate Impact Experimental Setup

High-strain rate, normal plate impact experiments were conducted with a powder gun facility at Caltech, equipped with a 3 m long keyed barrel with an inner

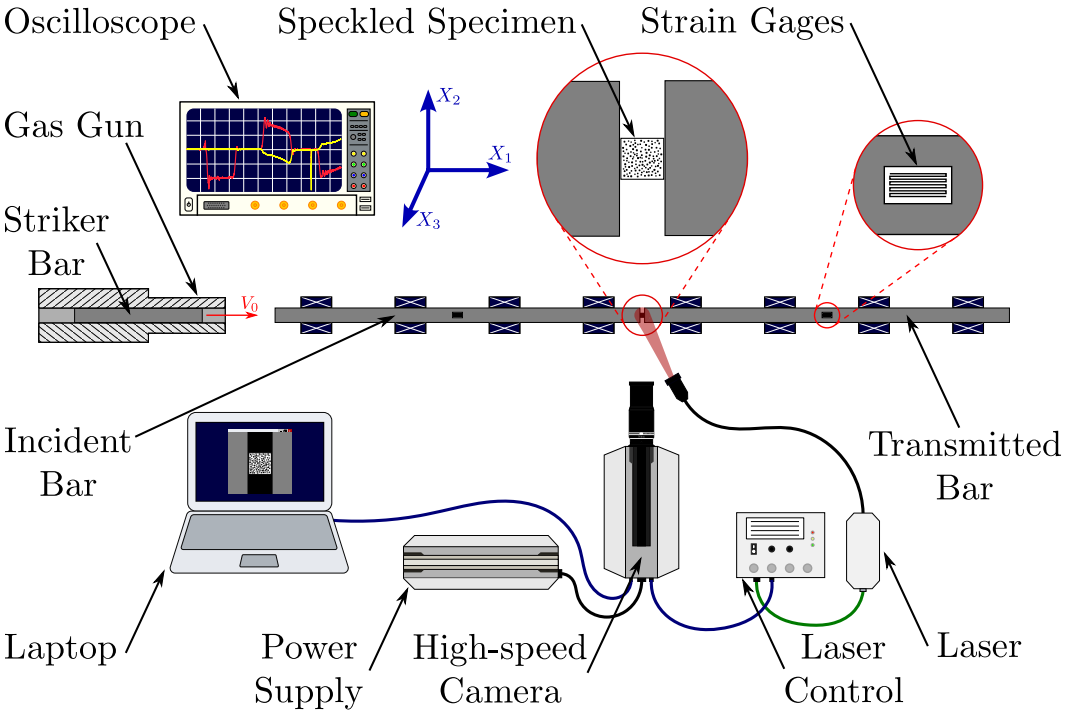

Figure 2.2: Experimental setup for split-Hopkinson (Kolsky) pressure bar (SHPB) experiments. The setup consists of the traditional components: gas gun, striker bar, incident bar, transmitted bar, strain gage system, oscilloscope, and sample. Additionally configured is the high-speed imaging setup which incorporates the high-speed camera and light source for imaging, in addition to speckle patterns used for DIC.

diameter of 38.7 mm. After sample preparation is finished and the target is mounted onto the six-degree-of-freedom gimbal, it is placed into the vacuum chamber for alignment. The flyer plate is glued to the projectile, which is placed into the end of the gun barrel. Next, the target plate is aligned in translational and rotational directions to minimize impact tilt. Then, the imaging diagnostics are set up, and the chamber is closed before final preparations are made to fire the projectile assembly.

The impact event is generated by igniting a gun-powder charge immediately behind the projectile. The resulting pressure build-up accelerates the projectile down the barrel, until it makes planar contact with the target specimen in the vacuum chamber. Upon impact, tilt pins in the target are shorted, triggering the diagnostics and measuring the impact time at four locations on the target. Based on time of impact and measured impact velocity, the angle between the flyer and target at impact (tilt) is calculated. Simultaneously, a shock wave initiates at the impact interface in both the flyer and the target, the effect of

which is captured by the diagnostics. Classical experiments utilize free surface velocity measurements at the rear of the sample, along with one-dimensional shock wave theories, to extract the material response under shock compression. Instead, here, high-speed imaging is used to visualize the shock propagation from left to right in the field of view, along with the resulting deformation behind the shock. The details of this visualization approach are discussed in Section 2.2.4, and a schematic of the experimental setup is shown in Fig. 3.2a. In addition to high-speed imaging, which captures the deformation in the target, the impact velocity is measured via two precisely spaced laser gates which measure the difference in time at which the projectile passes each laser and breaks the laser gates, just prior to impact.

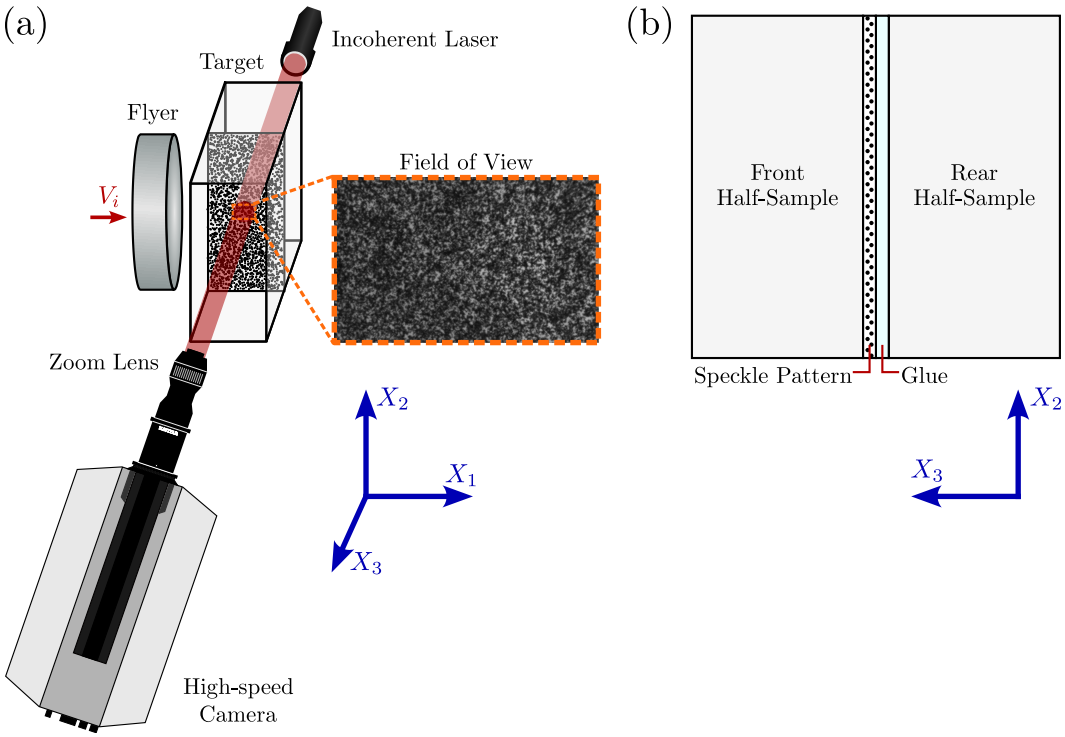

Figure 2.3: Plate impact experimental setup and target assembly orientation. (a) Experimental setup for plate impact experiments. Depicted is the flyer plate approaching the target. Also shown is the high-speed, high-magnification imaging setup, complete with backlit laser illumination, and an example field of view (see inset). (b) Schematic of target assembly and orientation relative to camera. This configuration, with the speckle pattern closer to the camera than the glue layer, is consistent for both SHPB and plate impact experiments. Note, the thickness of the speckle pattern and glue layer are exaggerated for illustrative purposes.

2.2.4 High-speed imaging and Digital Image Correlation (DIC)

While the high-speed imaging setup in the SHPB configuration follows conventional practices, translation of such a setup to plate impact experiments introduces several challenges. The same camera (Shimadzu HPV-X2) and light source (Cavitar incoherent laser) are used, but a number of issues must be addressed, including higher framing rates, in-material refractive index changes under shock compression, and the addition of high-magnification imaging. These details are discussed below, in addition to the DIC speckling and post-processing.

To begin with, high-magnification imaging was performed for the plate impact validation to ensure the internal DIC technique is applicable at fine length scales. This is relevant for many heterogeneous materials (e.g., porous media with pores on the order of μm$-$mm), and also provides sufficient DIC resolution to capture strain localization which may occur during dynamic loading. This was accomplished by using a Navitar $0.7-4.5$x zoom lens and 2x adapter tube assembly (Rochester, New York), which achieved a typical field of view of 2.8×1.75 mm (400×250 pixels, $7\,\mu$m/pixel). Compared to the SHPB experiments, for which the field of view in each experiment was approximately 7.2×4.5 mm ($18\,\mu$m/pixel), this is 2.6 times higher magnification. However, this gives rise to several issues. First, because of significant lens curvature inherent in the zoom lens, distortions are introduced to the images. This is remedied by taking a series of images in which the specimen undergoes rigid body motion in both horizontal and vertical translation directions, and applying a distortion correction function to regain the uniform displacement field. The same correction function can then be applied to each deformation image during the experiment. Second, the framing rate is increased from $2,000,000$ fps (SHPB) to $10,000,000$ fps (plate impact). This ultra-high speed imaging, in conjunction with the high magnification, creates a severely light-starved situation. Typically, the synchronized pulsed laser illumination source (50 ns pulse) used in this work provides sufficient light at this framing rate [12, 13], but here it is additionally necessary to configure the light source in a back-lit configuration (Fig. 3.2a) to maximize light captured by the zoom lens.

Preliminary experiments also revealed that when the shock wave passes through the field of view, the steep density gradient causes temporary loss of trans-

parency in the PMMA, which is quickly recovered behind the shock wave. However, an artificial rigid body motion was observed behind the wave, owing to the sharp change in refractive index of the material across the shock wave. Because the visualization plane is inside the PMMA target which is undergoing shock compression (i.e., light must carry information through the PMMA before arriving at the camera), this change in refractive index can cause optical distortions. The distortion can be mitigated by aligning the camera such that the lens is parallel to the target window surface (the outer, polished surface of the target which is parallel to the speckle plane). To this end, mirrors are mounted to the target window surface and extension tube, alignment is checked using an auto-collimator, and the alignment is fine-tuned using a five-degree-of-freedom optical stage for the camera. In theory, when these are perfectly aligned, the refractive index change would have no influence on the deformation images; in practice, there remains a small distortion which is primarily uniform (hence minimal influence in the strain measurements). The error associated with the technique is quantified through validation experiments in Section 2.3. It is worth noting that each inner-plane experiment was configured such that the speckled half-sample is nearer to the camera than the un-speckled half-sample, as is depicted in Fig. 3.2b. This ensures that the camera visualizes the internal speckle pattern without looking through the glue layer, and thus prevents any influence of the glue layer on the images.

Much attention, rightly, goes to the careful setup of the visualization system. However, the speckle pattern and the post-processing procedures also play a significant role in quantitative visualization. For each SHPB experiment (except IP4, Table 2.1), the speckle pattern is applied with an airbrush, applying black speckles onto the sample surface. This pattern is then covered with a thin, white, spray-painted background layer. The airbrush patterning generated suitable speckle sizes for low magnification imaging ($30-100\,\mu$m/speckle and $18\,\mu$m/pixel). In preparation for the plate impact experiment, toner powder was used in place of airbrushed black paint for one SHPB experiment (IP4) to ensure that black paint and toner powder are interchangeably non-intrusive for inner-plane specimens. For plate impact experiments, the toner powder was suspended inside a transparent paint which was airbrushed onto the internal surface, with no white background. This method generated $10-20\,\mu$m speckles, which is ideal for high-magnification DIC with a resolution of $7\,\mu$m/pixel.

After capturing experimental deformation images, DIC post-processing [6] was carried out using Correlated Solutions Vic-2D software (Columbia, South Carolina). Prior to analysis, distortion correction was carried out with the built-in correction algorithm. DIC analysis extracted in-plane (two-dimensional) full-field displacements from the deformation images using a subset size of 21 pixels along with a step size of 1 pixel. These DIC correlation settings were used for all experiments presented in this study. Following this, full-field strains were computed through discrete differentiation of the displacement field. For all SHPB experiments presented, the strain is computed in the Vic-2D software as the Lagrangian strain,

$$\varepsilon_{ij} = \frac{1}{2}\left(\frac{\partial u_i}{\partial X_j} + \frac{\partial u_j}{\partial X_i} + \frac{\partial u_k}{\partial X_i}\frac{\partial u_k}{\partial X_j}\right) \tag{2.1}$$

where u_i is the displacement component in the X_i direction and repeated indices indicate summation. Additionally, an inherent 90% center-weighted Gaussian spatial filter with a 15 pixel filter size is applied. Alternatively, for the plate impact experiment, to present the closest comparison to one dimensional shock theory, the one dimensional engineering strain (ignoring higher order terms in the Lagrangian strain metric) is computed below with a uniform spatial filter with a 15 pixel filter size.

$$\varepsilon_{11}^{Eng.} = \frac{\partial u_1}{\partial X_1} \tag{2.2}$$

2.3 Results

Validation experiments for the internal DIC technique were performed, first for SHPB experiments at two different strain rates, and then for plate impact experiments at a selected impact stress. The purpose of these experiments is three-fold: (i) to ensure the inner-plane specimen geometry does not introduce a non-physical material response, (ii) to confirm the ability to capture internal deformation fields using the proposed technique, and (iii) to quantify errors associated with the technique.

2.3.1 Split-Hopkinson Pressure Bar Experiments

SHPB experiments were conducted at strain rates of approximately 1500 and 3700 s^{-1}, corresponding to impact velocities of approximately 11.7 and 19.7 m/s, respectively, with two bulk SHPB (Fig. 3.1a) and two inner-plane SHPB

(Fig. 3.1b) samples tested at each strain rate (impact velocity). In these experiments, a nominally uniaxial stress loading condition is imposed. Hence, the deformation response should be uniform through the thickness of the sample, and the internal DIC measurements from inner-plane samples can be directly compared to the surface DIC measurements from bulk samples under nearly identical loading conditions (same impact velocity). The high-speed imaging was conducted at 2 million fps with a resolution of 18 μm/pixel to attain a field of view of 7.2×4.5 mm (400×250 pixels).

Table 2.1: Summary of SHPB experiments.

Experiment Number	Sample Type	Impact Velocity (m/s)	Speckle Type	**Sample Dimensions***		
				L_1 (mm)	L_2 (mm)	L_3 (mm)
B1	Bulk	11.7	Airbrush	4.529 ± 0.003	5.001 ± 0.040	4.805 ± 0.004
B2	Bulk	11.6	Airbrush	4.548 ± 0.003	4.837 ± 0.003	4.838 ± 0.003
B3	Bulk	19.7	Airbrush	4.532 ± 0.003	4.812 ± 0.005	4.557 ± 0.005
B4	Bulk	19.7	Airbrush	4.564 ± 0.002	4.548 ± 0.005	5.021 ± 0.031
IP1	Inner-Plane	11.7	Airbrush	4.814 ± 0.003	4.845 ± 0.006	5.003 ± 0.004
IP2	Inner-Plane	11.6	Airbrush	4.772 ± 0.005	4.801 ± 0.024	4.990 ± 0.005
IP3	Inner-Plane	19.7	Airbrush	4.648 ± 0.004	4.539 ± 0.019	4.911 ± 0.007
IP4	Inner-Plane	19.7	Toner Powder	4.780 ± 0.004	4.652 ± 0.016	$4.965 \pm$ NA

*L_1 is the thickness of the sample in the direction of compression. L_2 and L_3 are the dimensions of the cross-section, corresponding to the coordinate system in Fig. 2.2.

In total, eight SHPB experiments are presented, the details of which are summarized in Table 2.1. An example comparison between experiments B1 (bulk) and IP1 (inner-plane) is shown in Fig. 2.4 with a time series of selected images and overlaid DIC strain (ε_{11}) fields. Both the experiments were conducted under nearly identical conditions, with a striker bar impact velocity of 11.7 m/s. By visual inspection, both experiments show uniformity and minimal noise in the strain field. In addition, there is excellent agreement between the experiments, with the only notable difference being slight non-uniformity near the front and back faces of the sample, which are in contact with the incident and output bars, respectively. This feature is present in both B1 and IP1, but more significant in the inner-plane experiment (IP1). One can quantify the agreement, uniformity, and noise by investigating the strain evolution with time inside a 3 mm diameter circular region at the center of the sample, shown in Fig. 2.5a. The average longitudinal strains (ε_{11}) of the two experiments coincide very closely with one another, and the error bounds, denoting one standard deviation from the mean, are shown to be small. The distribution of full-field strain measurements for experiments B1 and IP1 is further

visualized for one arbitrary time instance, $t = 20\,\mu$s, in Fig. 2.5b. In this particular comparison (experiments B1 and IP1), the inner plane experiment is observed to be less noisy than the bulk; however, this result proves to be largely dependent on the quality of the speckle pattern and lighting of the particular experiment. In general, when comparing all SHPB experiments, the inner-plane DIC measurements have approximately equal levels of noise to the bulk DIC measurements The results in experiments B1 and IP1 represent the largest noise among the eight experiments.

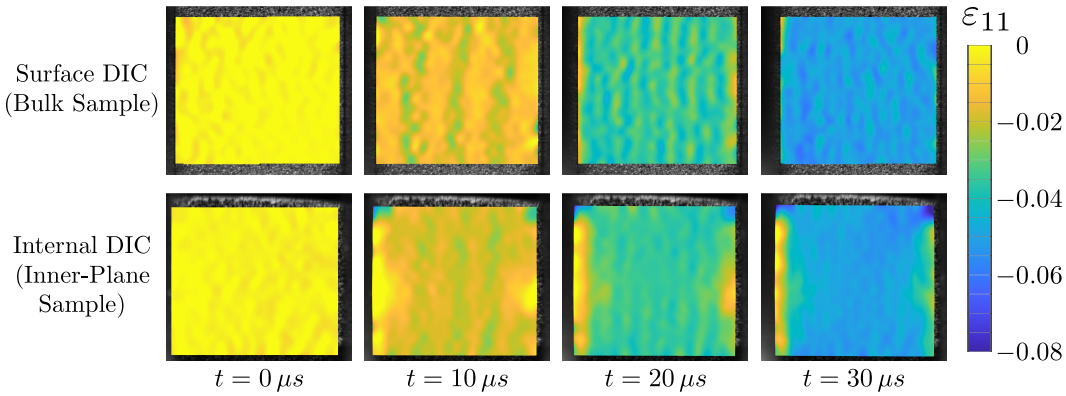

Figure 2.4: Frame-by-frame visualization of longitudinal strain on the surface and inner-plane of PMMA samples under SHPB loading at identical striker bar impact velocity, 11.7 m/s. Experiments B1 and IP1 are shown on top and bottom, respectively. Time, t = 0 corresponds to the arrival of the loading pulse at the interface between the incident bar and the front of the specimen. The overlaid DIC strain fields are each approximately $4.5 \times 4\,$mm.

A similar quantitative comparison among all eight experiments is made in Fig. 2.6, neglecting to include error bars for the sake of visibility, in which the time evolution of longitudinal (ε_{11}) and lateral (ε_{22}) strains, as well as the traditional stress-strain response, are compared. The averaged strain response from DIC is plotted in Fig. 2.6a-b, while the stress-strain response shown in Fig. 2.6c is derived through a combination of DIC strain measurements and engineering stress measurements via strain gage recordings on the transmitted bar, calculated as

$$\sigma(t) = \frac{A_b}{A_s} E_b \varepsilon_T(t). \tag{2.3}$$

Here, A_b and A_s are the cross-sectional areas of the bar and sample, respectively, E_b is the Young's modulus of the bar material (aluminum 7075) ($E_b = 71.7\,$GPa), and $\varepsilon_T(t)$ is the strain measurement on the transmitted bar. One observes close agreement (among experiments with the same im-

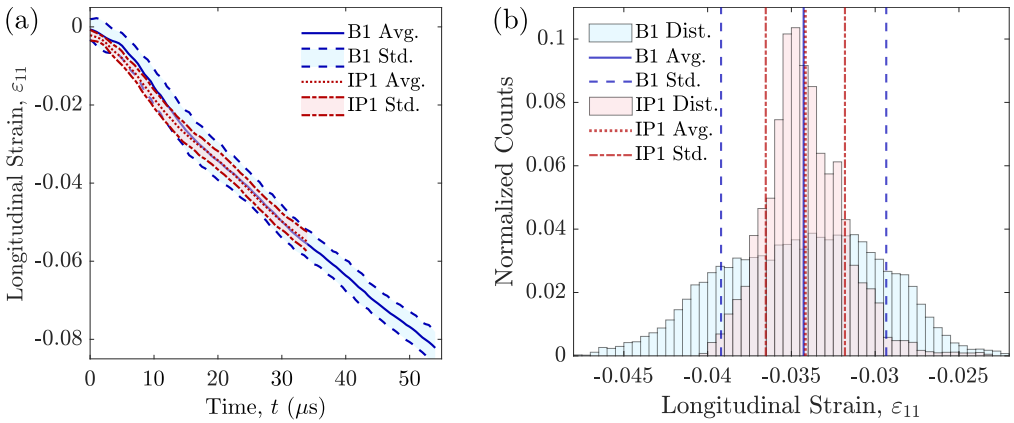

Figure 2.5: Error analysis of SHPB experiments B1 and IP1. Results for other experiments are similar and are omitted for the sake of clear visualization. (a) Longitudinal strain evolution, averaged over the area of interest, with shaded bounding curves representing one standard deviation from the mean. (b) Full histogram comparison at one time instance, $t = 20\,\mu$s, comparing the spatial distribution of longitudinal strain measurements for B1 and IP1. Note the spread is largely dependent on the quality of the speckle pattern. In general the inner-plane samples possess equal or better error bounds when compared with bulk samples for the SHPB experiments.

pact velocity) in the longitudinal and lateral strain measurements, regardless of specimen type or speckle type, indicating the technique works exceptionally well in the SHPB regime to characterize material deformation. However, at large strains the specimens begin to fail through brittle fracture. This is where notable differences arise, with the inner-plane specimens fracturing earlier than their bulk counterparts, because the internal DIC and glue interface supplies nucleation sites for fracture to occur. The stress-strain curves (Fig. 2.6c) make this difference clear, as the end of the curves, which mark the failure of the material, show consistent failure in the inner plane specimens at $4.4 - 5.5\%$ longitudinal strain, while the bulk specimens endure $7.6 - 8.2\%$ strain before failure. While this does pose a limitation on the technique for alternative applications, the current interest in these experiments lies only in the homogeneous deformation regime, not the failure regime.

In the following section the technique is extended to plate impact experiments, which feature a uniaxial strain state of deformation and maintain an overall compressive loading state due to lateral confinement, thus preventing the occurrence of brittle fracture. Hence, the SHPB experiments provide sufficient proof of concept to transition the technique from SHPB to plate impact. For

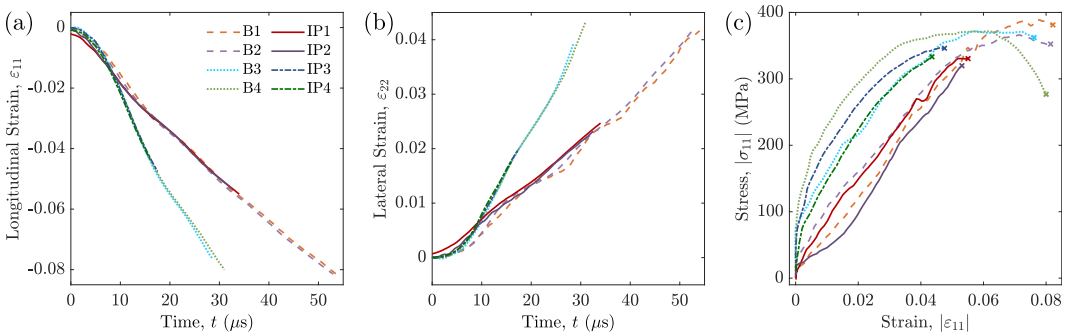

Figure 2.6: Summary of all eight SHPB experiments, including two different loading rates (Table 2.1). (a) Average longitudinal strain evolution, (b) Average lateral strain evolution, (c) Stress-strain curves. One can observe the close agreement of the strain evolution for each repeated impact velocity, regardless of specimen type (bulk or inner-plane). Stress-strain curves also show reasonable agreement during initial deformation (prior to failure). Note that the stress-strain curves are composed of DIC measurements of strain and strain gage measurements of stress. Dynamic equilibrium is estimated to occur after five reverberations of the compressive wave in the samples, corresponding to $16 - 18\,\mu$s.

applications interested in the failure regime of the SHPB experiments, alternative sample preparation techniques should be implemented which incorporate an internal speckle pattern without introducing a material interface. One such technique is the embedded speckle plane patterning technique [19, 21], though it has limitations for the study of pre-existing heterogeneities.

2.3.2 Plate Impact Experiment

To validate the effectiveness of the internal DIC for shock experiments, a normal plate impact experiment is conducted at 0.64 GPa impact stress on a PMMA target plate, with an internal speckle pattern, by impacting the target with an aluminum 7075 flyer. The target's internal speckle pattern was imaged via high-speed imaging at a framing rate of 10 Mfps with an image resolution of $7\,\mu$m/pixel and field of view of 2.8×1.75 mm (400×250 pixels). The experimental parameters for the experiment are summarized in Table 3.1.

While the uniaxial stress state in the SHPB experiments enabled direct comparison between strain measurements of the surface and inner-plane, the same does not hold in the case of plate impact experiments. Plate impact experiments undergo nominally uniaxial strain conditions at the interior of the sample, while the deformation state at the surface is changed by the lateral release

Table 2.2: Summary of normal plate impact experiment.

Flyer Material	Target Material	Flyer Thickness (mm)	Target Thickness (mm)	L_{FOV}* (mm)	Impact Velocity V_0 (m/s)	Impact Stress σ_{11} (GPa)	Tilt (mrad)
Al 7075	PMMA	12.799 ± 0.001	16.089 ± 0.014	5.0	219 ± 5	0.64 ± 0.02	3.4

*L_{FOV} indicates the distance from the impact surface to the center of the field of view (FOV).

waves which initiate from the free surfaces. Instead of making a direct experimental comparison, one can compute a theoretical shock strain [25], under the assumption of uniaxial strain deformation, against which the experimental result can be compared:

$$\varepsilon_{11}^{\text{Theory}} = \frac{u_p}{U_s}. \tag{2.4}$$

The particle velocity (u_p) can be computed from the measured impact velocity (V_0) and empirically known equations of state (EOS) relating the shock velocity (U_s) to the particle velocity ($U_s - u_p$ relation). This well-established methodology is known as impedance matching, which is well summarized by Meyers [25]. Tabular EOS data, for use in this technique, is readily available for both the flyer and target materials, aluminum 7075 [26] and PMMA [27], respectively. The linear $U_s - u_p$ relation (Eq. (3.5)) has been fit to the tabular data for each material, and the fitted material parameters, C_0 and S, are shown in Table 3.3.

$$U_s = C_0 + S u_p \tag{2.5}$$

Table 2.3: Equation of state parameters.

Material	Density, ρ_0 (kg/m^3)	C_0 (m/s)	S
PMMA [27]	1186	2770	2.11
Aluminum 7075 [26]	2804	5022	1.99

To evaluate the performance of the technique for plate impact experiments, one begins by considering the full-field longitudinal strain measurements. Figure 2.7 shows selected time instances during the experiment, where the area of interest (AOI) is marked by a white dashed box. This area of interest is determined by carefully selecting the front and back boundaries through inspection of the raw deformation images: selecting only the regions which are free of blurriness, which distorts the DIC-computed strain fields. Blurriness arises, in

part, from the steep density gradients associated with the shock wave (strong discontinuity in stress) and release waves which follow after the shock. In this experiment the shock wave, which travels from left to right, arrives in the field of view (FOV) at time, $t = 0$, and can be seen exiting the FOV at $t = 0.9\,\mu$s. Similarly, a blurry front enters the FOV at $t = 1.3\,\mu$s and covers half the FOV at $t = 1.8\,\mu$s. It is not clear whether this blurry front arises due to release waves from the impact surface or boundaries of the target, or from another source. Alternative sources could include lateral relaxation at the boundary of the target plate or changing refractive index due to changes in the stress state in the PMMA material which the camera looks through. Both of these sources would contribute to shifting the optical focal plane, which would introduce blur or defocusing. Motion blur due to large velocities is not an issue, which is evidenced by the crisp image quality immediately behind the shock wave where peak particle velocity is achieved.

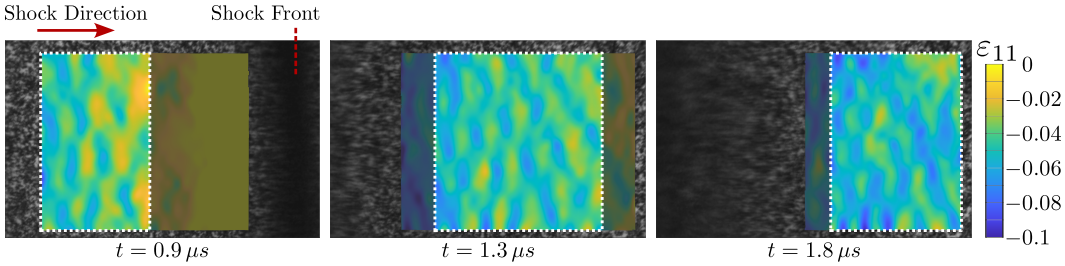

Figure 2.7: A series of images from the plate impact experiment, with longitudinal engineering strain, ε_{11}, overlaid. Time is shifted such that $t = 0$ coincides with the arrival of the shock wave in the field of view. The area of interest (region free from influence of wave distortion) is marked by the white, dashed box.

Examining the computed longitudinal strain field, it is apparent that within the AOI at each time step, the strain fields are fairly uniform, albeit with relatively large noise. This uniformity is an important feature, as the Hugoniot steady shocked state should possess constant, uniform strain behind the shock wave. Further, the averaged strain response in the AOI is displayed in Fig. 2.8a where the steady shocked state is shown to be nearly constant with respect to time, and approaches the theoretical shock strain. For the majority of the time instances, the error is less than 1% strain.

This experimental deviation from the theoretically predicted shock strain—measuring less than the theoretical value—is evidence of slight systemic error which may be attributed to small optical distortions arising from the defor-

mation of the transparent PMMA target which is being imaged through. The error may also be caused by possible deviation from the idealized uniaxial strain loading conditions assumed by theory. Additional noise is also inherent in these results, caused by several sources including DIC artifacts, rigid body motion arising from the temporary loss of correlation at the shock wave location, high-magnification imaging distortions, other optical distortions, and pixel interpolation used by the Shimadzu HPV-X2 camera at 10 Mfps imaging rate. To decouple the effects of the experimental configuration (e.g., camera, speckle pattern, DIC processing scheme, etc.) from those of the effects of shock compression (e.g., optical distortions), the strain noise should thus be compared with that of static, rigid body translation. The standard deviation for longitudinal strain is 0.0043 for static rigid body translation and 0.0116 under shock, meaning the experimental noise under shock compression is 2.7 times larger than that of ambient, static images. This result is visualized through a comparison of histograms for the data inside the AOI for a given time instance in the experiment (Fig. 2.8b) and for static, rigid body translation images (Fig. 2.8c). While not negligible, these error levels are deemed acceptable, especially for applications involving large, localized strains such as the shock compression of heterogeneous materials. The error can also be lowered through additional filtering (when suitable for the application) and through refinements of the technique such as improved speckle patterning, alignment, lighting, and camera hardware.

While the primary focus of the technique and the validation experiments is to perform internal strain measurements, a natural second validation metric is the internal particle velocity. For comparison, the theoretical particle velocity can be predicted through the impedance matching technique as described above. The experimentally measured particle velocity is then computed via central difference of the displacements measured with DIC. Figure 2.9a shows the average particle velocity in the area of interest for the duration of the experiment, compared with the theoretical particle velocity. The velocity measurements are relatively steady, as is expected for the post-shocked state, and demonstrate reasonable agreement with theory, with an error of approximately $10-30\,\mathrm{m/s}$. Interestingly, the particle velocity error percentage coincides closely with that of the strain measurements. This result provides additional confidence in the measurements, as shock strain and particle velocity are expected to scale proportionally with one another (Eq. (2.4)). It also suggests that the source of

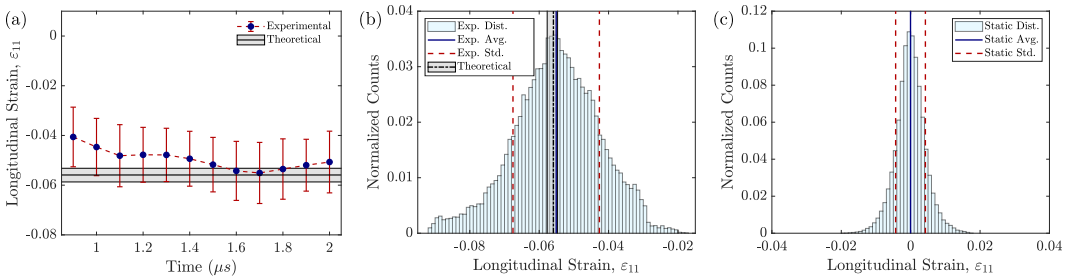

Figure 2.8: DIC results for the plate impact experiment inside the area of interest. (a) Averaged experimental longitudinal strain response compared with the theoretical shock strain (Eq. (2.4)) for the given impact conditions and material choice. Time is shifted such that $t = 0$ coincides with the arrival of the shock wave in the field of view. Error bars represent one standard deviation from the mean. (b) Histogram of local longitudinal strain measurements for a given time instance, $t = 1.7\,\mu$s, depicting the full measurement distribution in the area of interest. (c) Histogram of local longitudinal strain measurements for several static, rigid body translation images, using the same speckle pattern as in the experiment, to provide a noise floor for the DIC setup.

error could be a physical effect (as opposed to an optical distortion) such as deviation from the ideal uniaxial strain conditions which are assumed in one dimensional shock theory, as was mentioned previously. Alternatively, it is possible that the impedance matching technique over-predicts the theoretical strain and particle velocity for this experiment, owing to the unusual shock response of PMMA at low pressures [27–29] and possible variance in PMMA properties depending on the manufacturer. One must also note the importance of the scale calibration used to extract physical displacement measurements based on pixel values. While the strain measurements are insensitive to scale (being a non-dimensionalized quantity), the error in velocity measurements corresponds directly with the error in the calibration scale.

In addition to the particle velocity measurements, the shock front position is tracked and used to estimate the shock velocity (U_s) in the experiment. This is shown in Fig. 2.9b, which indicates a nearly constant shock velocity, and the associated linear fits estimate the value to be between $3.02 - 3.06$ km/s. This is in excellent agreement with the predicted shock velocity of 3.10 km/s.

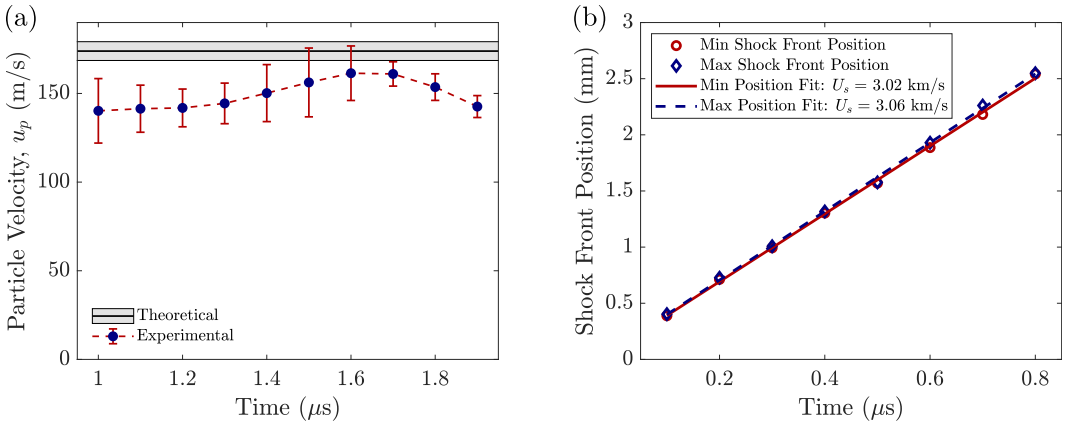

Figure 2.9: Velocity measurements for plate impact experiment. Time is shifted such that $t = 0$ corresponds with the arrival of the shock front in the field of view. (a) Averaged experimental particle velocity within the area of interest, computed from DIC displacement measurements via central difference. Experimental measurements are compared to the computed theoretical particle velocity, which is calculated through the impedance matching technique based on measured impact velocity and known material properties (see [25]). Experimental error bars include one standard deviation from the mean in addition to 2% error to account for error in the spatial scale. Theoretical error bars account for error in the impact velocity measurements and in the empirical equation of state data. (b) Shock front position measurements, estimated by manually identifying the location where the dark band (indicative of the shock front) begins. The linear fits to the position data provide an estimate of the shock front velocity, which is very close to the theoretically predicted value of 3.10 km/s.

The present validation experiment demonstrates the feasibility of the technique for application in shock compression of transparent materials. This technique, which is the first to enable accurate, full-field deformation measurements inside shocked materials, shows promise and presents significant opportunities to study the local material response near heterogeneities under dynamic loading conditions [30].

2.4 Conclusion

An experimental technique to perform internal DIC has been developed to characterize the large deformation strain fields inside of transparent specimens in the high-strain rate regime with traditional full-scale, dynamic, high-strain rate laboratory experiments. The technique is demonstrated in PMMA for both SHPB and normal plate impact experiments, but it should be possible

to implement with many transparent materials and in conjunction with most laboratory dynamic experiments. This represents a critical experimental development enabling investigation of complex phenomena occurring under extreme dynamic loading, such as the deformation and failure of heterogeneous materials at the mesoscale, the local material response under complex loading states, and the evolution of failure modes which are sensitive to boundary effects.

Validation experiments were performed to determine the feasibility and accuracy of the technique. It was found to be quite accurate (0.2% strain noise, which approaches the noise floor of conventional static DIC) in SHPB experiments during the initial deformation period, though the duration for DIC measurements was shortened by the brittle fracture response of the inner-plane specimens. In the future, this issue could be mitigated for homogeneous samples by adopting the embedded speckle plane patterning technique used elsewhere [19, 21], though clever solutions would be necessary when using that patterning method for heterogeneous materials. When the current internal DIC technique was applied to plate impact experiments, it was found to be accurate to within about 1% strain and viable up to approximately 0.65 GPa impact stress. Several possible error sources are identified, and solutions are presented where applicable. Different material systems, larger specimen size (diameter of the gun barrel), alternative magnifications, improved camera hardware, and better speckle patterning may enable improvement of the technique by mitigating the aforementioned sources of error, thus improving image quality and DIC resolution. Still, the accuracy achieved and the stress regime accessed for the experiments were sufficient to demonstrate the feasibility of the technique in extreme environments, which push the limit of state of the art high-speed cameras.

Future work will focus on extending this technique beyond 0.65 GPa impact stress, incorporating modifications to minimize the error, and implementing the technique in various alternative experimental setups and with different transparent materials. Further, the internal DIC technique will be used to study the local shock response of heterogeneous materials. Namely, interest lies in examining porous materials through investigation of the pore collapse phenomenon [16, 18, 30], and particulate composites through study of the material response and interaction at the interface between hard inclusions and polymer matrix.

References

[1] G. S. Settles, *Schlieren and shadowgraph techniques: Visualizing phenomena in transparent media* (Springer Science & Business Media, 2001).

[2] J. W. Dally, "An introduction to dynamic photoelasticity," Experimental Mechanics **20**, 409–416 (1980).

[3] H. V. Tippur, S. Krishnaswamy, and A. J. Rosakis, "A coherent gradient sensor for crack tip deformation measurements: analysis and experimental results," International Journal of Fracture **48**, 193–204 (1991).

[4] W. H. Peters and W. F. Ranson, "Digital imaging techniques in experimental stress analysis," Optical Engineering **21**, 10.1117/12.7972925 (1982).

[5] M. Sutton, W. Wolters, W. Peters, W. Ranson, and S. McNeill, "Determination of displacements using an improved digital correlation method," Image and Vision Computing **1**, 133–139 (1983).

[6] M. A. Sutton, J. J. Orteu, and H. Schreier, *Image correlation for shape, motion and deformation measurements: Basic concepts, theory and applications* (Springer US, 2009), pp. 1–321.

[7] L. Bodelot, J. P. Escobedo-Diaz, C. P. Trujillo, D. T. Martinez, E. K. Cerreta, G. T. Gray, and G. Ravichandran, "Microstructural changes and in-situ observation of localization in OFHC copper under dynamic loading," International Journal of Plasticity **74**, 58–74 (2015).

[8] P. Malchow, B. Koohbor, S. Ravindran, and A. Kidane, "In-situ quantification of intra and intergranular deformation in pure magnesium using full-field measurements at low and high strain rates," Mechanics of Materials **126**, 36–46 (2018).

[9] P. L. Reu and T. J. Miller, "The application of high-speed digital image correlation," The Journal of Strain Analysis for Engineering Design **43**, 673–688 (2008).

[10] J. Seidt, V. Kuokkala, J. Smith, and A. Gilat, "Synchronous full-field strain and temperature measurement in tensile tests at low, intermediate and high strain rates," Experimental Mechanics **57**, 219–229 (2017).

[11] A. Keyhani, R. Yang, and M. Zhou, "Novel capability for microscale in-situ imaging of temperature and deformation fields under dynamic loading," Experimental Mechanics **59**, 775–790 (2019).

[12] S. Ravindran, V. Gandhi, A. Joshi, and G. Ravichandran, "Three-dimensional full-field velocity measurements in shock compression experiments using stereo digital image correlation," Review of Scientific Instruments **94**, 10.1063/5.0131590 (2023).

[13] S. Ravindran, V. Gandhi, B. Lawlor, and G. Ravichandran, "Mesoscale shock structure in particulate composites," Journal of the Mechanics and Physics of Solids **174**, 10.1016/j.jmps.2023.105239 (2023).

[14] M. Wisnom, "The role of delamination in failure of fibre-reinforced composites," Philosophical Transactions of the Royal Society A: Mathematical, Physical and Engineering Sciences **370**, 1850–1870 (2012).

[15] S. Abrate, *Impact on composite structures* (Cambridge University Press, 1998).

[16] E. M. Escauriza, J. P. Duarte, D. J. Chapman, M. E. Rutherford, L. Farbaniec, J. C. Jonsson, L. C. Smith, M. P. Olbinado, J. Skidmore, P. Foster, T. Ringrose, A. Rack, and D. E. Eakins, "Collapse dynamics of spherical cavities in a solid under shock loading," Scientific Reports **10**, 10.1038/s41598-020-64669-y (2020).

[17] B. Branch, A. Ionita, B. E. Clements, D. S. Montgomery, B. J. Jensen, B. Patterson, A. Schmalzer, A. Mueller, and D. M. Dattelbaum, "Controlling shockwave dynamics using architecture in periodic porous materials," Journal of Applied Physics **121**, 10.1063/1.4978910 (2017).

[18] Z. Lovinger and R. Kositski, "Shear localization as a damage mechanism in pore collapse under shock compression," International Journal of Impact Engineering **193**, 10.1016/j.ijimpeng.2024.105039 (2024).

[19] T. A. Berfield, J. K. Patel, R. G. Shimmin, P. V. Braun, J. Lambros, and N. R. Sottos, "Micro-and nanoscale deformation measurement of surface and internal planes via digital image correlation," Experimental Mechanics **47**, 51–62 (2007).

[20] J. Y. Huang, Y. Li, Q. C. Liu, X. M. Zhou, L. W. Liu, C. L. Liu, M. H. Zhu, and S. N. Luo, "Origin of compression-induced failure in brittle solids under shock loading," Physical Review B - Condensed Matter and Materials Physics **92**, 10.1103/PhysRevB.92.144101 (2015).

[21] A. McGhee, J. Yang, E. C. Bremer, Z. Xu, H. C. Cramer, J. B. Estrada, D. L. Henann, and C. Franck, "High-speed, full-field deformation measurements near inertial microcavitation bubbles inside viscoelastic hydrogels," Experimental Mechanics **63**, 63–78 (2023).

[22] W. W. Chen and B. Song, *Split Hopkinson (Kolsky) bar: Design, testing and applications* (Springer Science & Business Media, 2010).

[23] K. T. Ramesh, "High rates and impact experiments," in *Springer handbook of experimental solid mechanics* (Springer, 2008), pp. 929–960.

[24] H. Kolsky, "An investigation of the mechanical properties of materials at very high rates of loading," Proceedings of the Physical Society. Section B **62**, 676–700 (1949).

[25] M. A. Meyers, *Dynamic behavior of materials* (John Wiley & Sons, Ltd, Sept. 1994).

[26] S. P. Marsh, *LASL shock hugoniot data*, Vol. 5 (University of California Press, 1980).

[27] L. M. Barker and R. E. Hollenbach, "Shock-wave studies of PMMA, fused silica, and sapphire," Journal of Applied Physics **41**, 4208–4226 (1970).

[28] D. Lacina, C. Neel, and D. Dattelbaum, "Shock response of poly [methyl methacrylate] (PMMA) measured with embedded electromagnetic gauges," Journal of Applied Physics **123**, 10.1063/1.5023230 (2018).

[29] J. L. Jordan, D. Casem, and M. Zellner, "Shock response of polymethylmethacrylate," Journal of Dynamic Behavior of Materials **2**, 372–378 (2016).

[30] B. P. Lawlor, V. Gandhi, and G. Ravichandran, "Full-field quantitative visualization of shock-driven pore collapse and failure modes in PMMA," Journal of Applied Physics **136**, 225901 (2024).

Chapter 3

QUANTITATIVE VISUALIZATION OF A SINGLE PORE UNDER SHOCK COMPRESSION

B.P. Lawlor, V. Gandhi, and G. Ravichandran, "Full-field quantitative visualization of shock-driven pore collapse and failure modes in PMMA," Journal of Applied Physics **136**, 225901 (2024).

Contributions: B.P.L. participated in conception of the project, performed the experiments, conducted the numerical simulations, integrated the theoretical analysis, analyzed the results, and wrote the manuscript.

Abstract

The dynamic collapse of pores under shock loading is thought to be directly related to hot spot generation and material failure, which is critical to the performance of porous energetic and structural materials. However, the shock compression response of porous materials at the local, individual pore scale is not well understood. This study examines, quantitatively, the collapse phenomenon of a single spherical void in PMMA at shock stresses ranging from $0.4 - 1.0$ GPa. Using a newly developed internal digital image correlation technique in conjunction with plate impact experiments, full-field quantitative deformation measurements are conducted in the material surrounding the collapsing pore for the first time. The experimental results reveal two failure mode transitions as shock stress is increased: (i) the first *in-situ* evidence of shear localization via adiabatic shear banding and (ii) dynamic fracture initiation at the pore surface. Numerical simulations using thermo-viscoplastic dynamic finite element analysis provide insights into the formation of adiabatic shear bands (ASBs) and stresses at which failure mode transitions occur. Further numerical and theoretical modeling indicates the dynamic fracture to occur along the weakened material inside an adiabatic shear band. Finally, analysis of the evolution of pore asymmetry and models for ASB spacing elucidate the

mechanisms for the shear band initiation sites, and elastostatic theory explains the experimentally observed ASB and fracture paths based on the directions of maximum shear.

3.1 Introduction

Porous materials such as energetic (e.g., polymer bonded explosives) and structural (e.g., foams) materials feature in many applications. When such materials are dynamically loaded (e.g., shocked), a pore collapse phenomenon occurs, the physics of which has great implications for both these material classes. Generally, in energetic materials, the main concern is with mechanically-induced hot spot generation via stress waves, which likely dictates the ignition response of the material [1–5] and may lead to detonation. This has often been linked to pore collapse [6–8]. Thus, it is desirable to understand the mechanical response of pore collapse, which may provide insights to the hot spot generation mechanisms and aid in preventing accidental detonations.

For structural materials, porosity may be either intentional, as is the case for metallic foams and architected metamaterials, or unintentional through defects in manufacturing processes such as in additive manufacturing. Additionally, in these examples the length-scale of porosity ranges from nanometers through centimeters, making the material response of porous media a rich topic of study. The primary issue with these structures lies in the localized material and structural failure which is often driven by stress concentrations in the neighborhood of pores. Some porous media can be treated as continuum materials through the investigation of the effective or homogenized response when the pore scale is far smaller than the application scale. However, for the most effective prediction of failure in these structures, it is critical to also characterize the failure response of the material, and to understand it from a fundamental, local perspective at the individual pore scale.

The focus of this study is to quantitatively characterize the deformation and failure response surrounding a single collapsing spherical pore. This is accomplished through generation of shock-induced pore collapse via plate impact experiments, and measurements are conducted with high-speed imaging and internal digital image correlation (DIC) to capture the *in-situ* full-field deformation response. Previous studies have extensively investigated the macroscopic dynamic response of porous materials through pointwise measurements,

in addition to several works at the local scale which use qualitative imaging techniques or post-mortem analysis to understand the physics of pore collapse at the local scale. The rich literature, discussed below, leaves a substantial need for full-field quantitative analysis of the pore collapse problem, which is addressed in this study.

The macroscopic, or continuum, response of porous materials under dynamic loading has been studied at great length. In general, porous materials have been shown to possess favorable qualities such as shock disruption via micro-inertial effects [9, 10] and shock attenuation due to the large plastic work required to fully close pores [11]. However, the spall strength has been shown to depend on the initial porosity, in some cases decreasing (compared to its fully dense counterpart)[12], and others increasing [11, 13]. This dependence has been shown to depend on the bulk material properties and initial porosity. The many mechanisms involved in their shock response makes design with porous materials a complicated task. Theoretical approaches, assuming symmetric collapse of pores, originated with the work of Herrmann which enabled the introduction of porosity to the equation of state for materials in what is known as the $P - \alpha$ theory [14]. Carroll and Holt subsequently developed an analytical form for the α parameter [15] through the analysis of a thick spherical shell. Following this work, many modifications were made to the $P - \alpha$ theory. For example, Butcher et al. incorporated the influence of deviatoric stress, work-hardening, initial void size, and material viscosity [16] which revealed the effect of micro-inertia and viscosity on delaying the void collapse. Furthermore, extensive analytical, numerical, and experimental investigations have followed to understand the macroscopic response of porous solids under dynamic loading conditions [9, 10, 17, 18].

While the macroscopic (continuum) response to shock loading, measured through traditional interferometric techniques, has been well investigated to characterize the equation of state and shock structure, studies on the deformation and failure at the local length scale of individual pores have been sparse. However, the advances in high-speed imaging technologies in the last few decades have begun to enable full-field investigation at the local scale. Early experiments were limited to qualitative characterization of the collapse of cylindrical holes in transparent gels [19, 20] through high-speed imaging, and later were extended to quantitative characterization via particle image velocimetry [21].

These authors observed jetting at higher stresses and clear evidence of shock shielding and amplification effects for arrays of holes.

Recently, access to advanced x-ray synchrotron sources has enabled internal imaging of opaque structural materials during plate impact/shock experiments. Investigation, using x-ray phase contrast imaging (PCI), of additively manufactured lattice structures under shock revealed insights into the jet initiation (simple cubic) and mitigation (face centered tetragonal) phenomena which were controlled by the details of the lattice structures [22]. Further, the role of material parameters, lattice length scales, and impact velocity on jetting transitions was systematically investigated via experiment and simulation [23]. Similar experiments demonstrated that a pore in the shape of an elongated triangle behaved as a shock diode: promoting jetting when impacted from one direction, while disrupting the shock from the other direction [24]. These experiments also investigated the shock shielding properties of a series of holes.

A close experimental analog to the spherical pore collapse phenomena is the hole closure experiment, in which specimens with cylindrical holes are dynamically loaded via plate impact. Glazkov et al. used these experiments, with pre- and post-mortem hole size measurements, to infer material response at high-strain rates [25]. Lind et al. performed similar hole closure experiments in copper [26], now using PCI to capture the evolution of the area of the hole, *in-situ* during closure. They primarily used the rich and complicated loading state in these experiments to calibrate material models at high-strain rates and large strains. However, the inverse analysis also offers insights into the physics of pore collapse, as the rate of closure and final collapsed volume were shown to be highly dependent on the strain rate hardening of the material. Further analysis of these experiments could inform parameters for analytical continuum models such as the $P - \alpha$. Follow-up experiments on tantalum [27] served a similar role for model parameter calibration, while also observing possible shear localization (an important failure and hot-spot generation mechanism) near the closed hole through post-mortem electron backscatter diffraction (EBSD) analysis.

To investigate the physics of pore collapse, Escauriza et al. conducted plate impact experiments on PMMA with a spherical pore [28]. Using PCI they captured the pore collapse evolution—observing a transition from strength

dominated (low pressure) to hydrodynamic (high pressure) regimes, the development of cracks at low pressures, and jetting instabilities at high pressures. Complementary numerical simulations predicted the development of adiabatic shear bands during these collapse events [29]. Recently, Lovinger and Kositski carried out cylindrical pore collapse experiments in Ti-6Al-4V specimens, leveraging plate impact with a soft-catch setup, which enabled post-mortem analysis of the specimens [30]. Their work revealed the first definitive evidence of shear localization in pore collapse via adiabatic shear banding and shear cracking. They further explored the role of pore size and spacing on failure initiation and connectivity, respectively. While the aforementioned works have all been limited by sample fabrication and experimental resolution to pores near the mm scale, a new technique has been recently developed which uses PCI to capture the collapse of spherical pores on the order of several 10s of microns [31]. This technique promises future understanding of pore collapse at very fine spatial scales which are relevant to many commonly occurring pores. These experimental efforts and complementary computational endeavors have enriched our understanding of the pore collapse phenomena. However, to understand the details of shear localization and failure thresholds, a need still remains for quantitative full-field measurements during the pore collapse phenomena under shock compression.

To quantitatively characterize the deformation field around a pore under shock compression, it is proposed to perform plate impact experiments on PMMA samples with a single, embedded, spherical pore, in conjunction with high-speed digital image correlation (DIC) [32]—a non-contact quantitative imaging technique. Plate impact experiments require measurements to be performed at the center of the target plate, such that the uniaxial strain condition is maintained throughout the measurement, until the time at which release waves arrive. Hence, the embedded pore must be located at the center of the sample, and DIC performed internally at the mid-plane of the pore. This is essential to capture the true deformation response and failure mechanisms during the pore collapse event, as opposed to alternative approaches of making surface measurements and leveraging computational tools to infer the internal response. Further, this approach enables a more physically relevant investigation of spherical pores undergoing collapse, as opposed to cylindrical holes.

In this study, the internal DIC technique [33] for shock compression experiments is implemented to study pore collapse at shock stresses ranging from $0.4 - 1.0\,\mathrm{GPa}$. The internal DIC method is briefly summarized, and details regarding sample preparation, plate impact experiments, and high-speed imaging are described in Section 3.2. Results for the experiments and initial DIC analysis are presented in Section 3.3. Simulations are then conducted, replicating the loading conditions of the experiments in Section 3.4, and the physics governing failure mechanisms are discussed and supported with theoretical models in Section 3.5. Lastly, concluding remarks are given in Section 3.6.

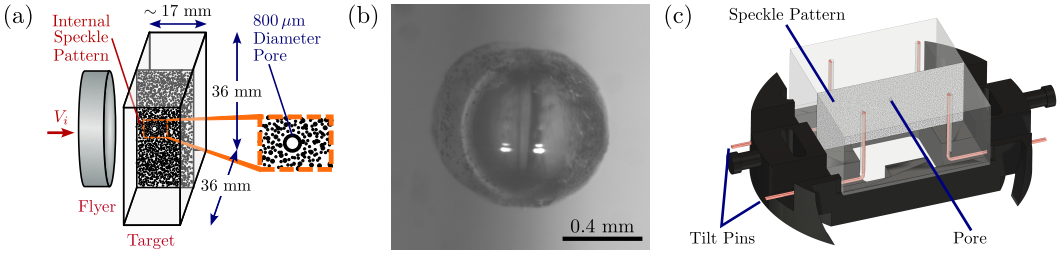

Figure 3.1: Details of the specimen preparation. (a) Plate impact pore collapse flyer and target specimens. (b) Microscope image of the spherical pore inside the target plate. Glue interface is slightly visible at the center of the pore. (c) CAD schematic of target plate, mounted onto the front of the target holder and equipped with electrical shorting pins. The top surface is the impact plane.

3.2 Materials and Methods

3.2.1 Quantitative Imaging of Displacements

Digital image correlation (DIC) is a non-contact, full-field, quantitative imaging technique, which measures the displacement field of a body undergoing deformation by correlating, or pattern matching, a unique grayscale speckle pattern which is applied to the specimen prior to deformation [32]. Images taken before and throughout the deformation then contain the necessary information for correlation to extract the displacement field with respect to the reference (undeformed) configuration, which can be converted to full-field strain measurements through discrete differentiation. The technique is traditionally restricted to surface measurements; however, in this work an internal DIC framework is employed to capture deformation around a collapsing pore under shock compression. The concept of internal DIC has been successfully implemented previously in the quasi-static regime [34] and in dynamic laser-induced cavitation experiments in gels, conducted under a microscope [35].

Recently, this technique was extended to be used in full-scale dynamic experiments, demonstrating its feasibility and accuracy for application to both split-Hopkinson (Kolsky) pressure bar and plate impact shock experiments. Details of the development of the internal DIC technique are presented elsewhere [33], and are only briefly summarized here. The optical technique involves embedding a speckle pattern at the internal plane of the transparent sample. By visualizing through the transparent sample (shifting the camera's focal plane to the internal plane), in-plane deformation is captured in the images (i.e., the direction of compression is in the same plane as the speckle pattern, in this case, horizontally). Here, normal plate impact experiments were conducted on PMMA samples, coupled with ultra-high speed imaging and digital image correlation (DIC) [32, 36, 37] to extract full-field quantitative strain measurements surrounding the pore during deformation.

3.2.2 Sample Preparation

Specimen preparation for plate impact experiments is a stringent process, requiring precise, detailed steps to ensure the specimens are suitable for the experiments. The target specimens for all experiments in this study, depicted in Fig. 3.1a, were manufactured from PMMA stock material obtained from E&T Plastics (Long Island City, New York). To embed the internal DIC speckle pattern and spherical pore, the target is manufactured from two cuboidal half-samples with rectangular cross section of nominal dimensions, 36 mm $\times$ 18 mm and 17 mm thick. Both half-samples are carefully lapped together in the impact and visualization directions to ensure identical dimensions and create ideal bonding surfaces. The visualization surfaces (all surfaces which are parallel to the speckle pattern plane) are then mirror polished to maximize transparency, and matching hemispheres of radius 0.4 mm are milled into each half-sample such that they precisely align to their counterpart to generate a nearly perfect spherical pore when combined. Next, the DIC speckle pattern is applied to the inner surface of one half-sample by airbrushing a thin layer of transparent paint and blowing toner powder onto the wet paint, before adding a second layer of transparent paint to seal the speckle pattern.

After the paint is allowed to dry for at least 24 hours, the half-samples are glued together with a two-part epoxy, EpoxAcast 690 (SmoothOn, Macungie, Pennsylvania). Confining plates are used to precisely align the two hemi-

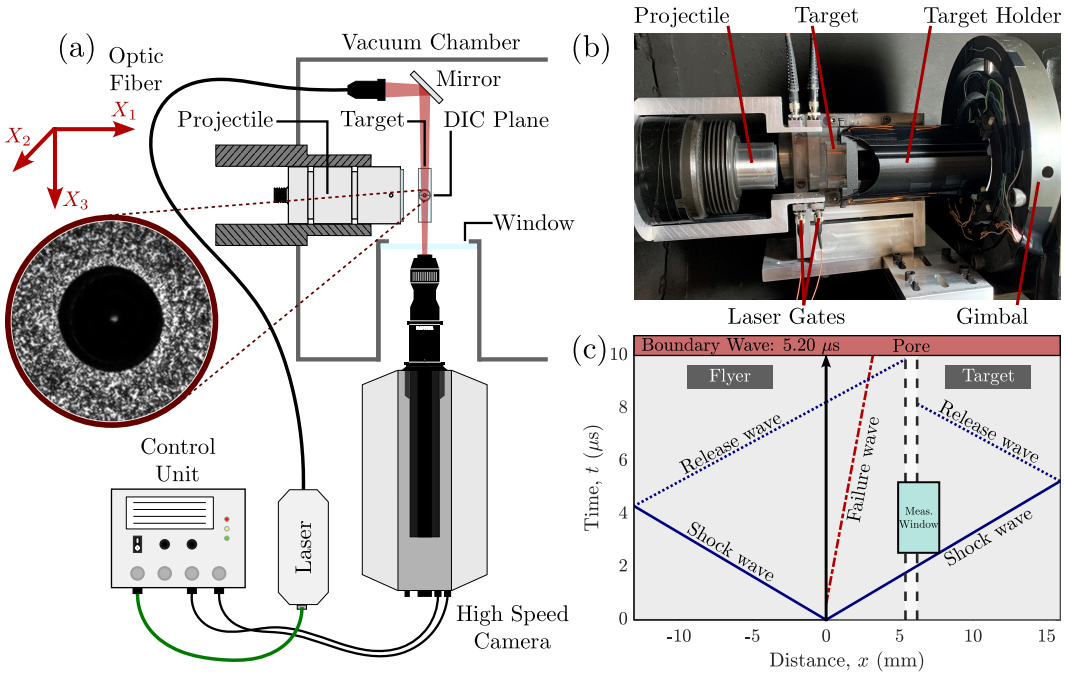

Figure 3.2: Experimental setup for plate impact experiments. (a) Schematic of experimental components set up in and around the vacuum chamber. Depicted is the projectile with flyer plate affixed, approaching the target plate. Also shown is the high-speed, high-magnification imaging setup, complete with backlit laser illumination. An example image of the pore and the surrounding region is shown in the inset. (b) Photo of the chamber setup for a shot. Six-DOF gimbal shown on the right side of the image, with the target mounted onto it via a long target holder. Also included is the housing for the laser illumination source behind the target. (c) Distance-time ($x - t$) diagram for Pore–0.4, used for experimental design to maximize measurement time window. Shock, release, and failure waves are labeled accordingly; the impact plane between flyer and target lies at $x = 0$; the pore is marked by two vertical, dashed lines. The "measurement window" is visualized by a light blue box, which is bounded in the x dimension to indicate the camera field of view and bounded in the t dimension to indicate the beginning and end of the measurement window.

spheres to generate a pristine spherical pore, and weights are applied to the sandwiched sample to squeeze out excess glue and thus maximize the glue bond strength. Once the sample has settled for approximately ten minutes, the weights are removed, the sample is carefully disassembled, and any glue which has filled the pore is removed. The assembly is then reset with confinement and weights, without additional glue, to ensure the pore is filled with air, rather than glue. Finally, after the glue cures for 24 hours, the now-intact sample is removed, re-lapped in the impact direction to meet specifications for the experiment, and the alignment of the pore is inspected under a microscope. Figure 3.1b shows an example of the pore alignment. Additionally, because of the precise restrictions on the half-sample geometry and careful alignment during gluing, residual stresses arising from the gluing process are estimated to be orders of magnitude smaller than the imposed shock stress in the experiments. Hence, these effects are considered to be negligible in the outcome of the experiments. The final restrictions for the target sample are less that $30\,\mu$m variation in thickness and less than $1\,\mu$m surface flatness as measured by Fizeau rings under monochromatic light with a quartz optical flat. After the target is assembled, the final specimens are nominally 36×36 mm square plates which are 17 mm thick.

Flyer plates made of PMMA or aluminum (7075 alloy) are more straightforward to manufacture, starting with machined cylindrical samples of 35 mm diameter and 13 mm thickness. They are lapped until the thickness variation is less than $10\,\mu$m and the surface flatness is less than $0.5\,\mu$m. These restrictions on the target and flyer plates ensure planar shock wave generation upon impact. Finally, the flyer plate is glued into the projectile and inserted in the gun barrel.

Electrical shorting pins are used in these experiments to trigger diagnostics and to measure the angle of inclination (tilt) between the flyer and target at impact. These pins are inserted into holes in the target plate which correspond with the perimeter of the flyer, and are glued in place, as shown in Fig. 3.1c. They are then sanded down, and lapped until flush with the impact surface. Finally, the target plate is glued to the target holder, the shorting pins are wired into a logic circuit box that is connected to a digital oscilloscope, and the target holder is mounted onto a six-degree-of-freedom gimbal which is moved into the vacuum chamber for alignment.

3.2.3 Plate Impact Experimental Setup

Normal plate impact experiments were performed using a powder gun facility at Caltech, which consists of a 38.7 mm diameter keyed barrel of 3 m length. Before running the experiment, the projectile is placed at the end of the gun barrel, and brought close to the target, which is mounted to the gimbal in the vacuum chamber. Careful translational and rotational alignment, using an auto-collimator, is performed to ensure perfect alignment between the impact surfaces of the two plates. This is critical to minimize the impact tilt between the flyer and target plates during the shot and ensure plane wave propagation. The high-speed camera is also optimally configured and aligned parallel to the target visualization surface closest to the camera, after which the field of view and focal plane are set. A schematic of the full experimental setup is provided in Fig. 3.2a, and an image of the setup inside the vacuum chamber is shown in Fig. 3.2b. The experiment begins when the gunpowder charge is ignited behind the projectile, propelling it down the barrel where it impacts the target plate, situated in the vacuum chamber at the end of the barrel. Upon impact, shorting pins trigger the high-speed imaging diagnostics to begin recording. Simultaneously, a planar shock wave is generated in both the target and flyer, and the camera captures images of the shock propagation and the in-plane deformation of the target plate. To measure the impact velocity, a laser system composed of two precisely spaced laser gates captures the moment at which the projectile breaks each laser plane. In some experiments, which do not use a conductive flyer (Pore–0.4), the laser gate system is also used to trigger the camera to record.

Plate impact experiments require careful design to ensure the desired loading state is applied and the material response is measured prior to the arrival of release waves. Flyer plate materials and impact velocities are selected to generate the desired shock stresses in the target material. For a given impact velocity (V_i), the imposed particle velocity (u_p) in the target material is determined through the impedance matching technique [38] based on the known ambient material density (ρ_0) and equation of state ($U_s - u_p$ relation, where U_s is the shock wave speed, given in Eq. (3.5)) for both the flyer and target materials. From there, shock stress is calculated using Eq. (3.1).

$$\sigma_{11} = \rho_0 U_s u_p \tag{3.1}$$

The timing of several release waves must also be calculated, including those initiating from the flyer free surface, the target free surface, and the perimeter/boundary of the target plate because of traction-free conditions. The design can be visualized through a distance-time ($x - t$) diagram which plots the propagation of all relevant stress waves in the experiment. Further discussion of wave propagation and $x - t$ diagrams can be found elsewhere [38]. An example $x - t$ diagram is shown in Fig. 3.2c for the 0.41 GPa shock stress pore collapse experiment. Upon impact at time, $t = 0$, a normal shock wave is generated in both the target (forward-propagating) and flyer (backward-propagating), which induces pore collapse after passing the pore at 2.03 μs. The "measurement window" begins when the shock wave passes the camera field of view at 2.54 μs and ends when the field of view is disturbed by the arrival of either a free surface release, boundary release, or "failure wave" observed previously in PMMA [39]. These waves alter the uniaxial strain loading conditions, occlude the field of view, or both. This measurement window can be maximized for a given shock stress by using a thick flyer and target (to delay the arrival of free surface release waves), and optimizing the distance of the pore away from the impact surface to balance competition between boundary wave and failure wave arrival. Flyer diameter and target width could also be used to delay boundary wave arrival, but are limited by the size of the powder gun barrel. In the example used in Fig. 3.2c, the measurement window is closed by the arrival of boundary release waves at 5.20 μs, producing a predicted window of 2.66 μs for Pore–0.4. Unfortunately, the failure wave speed increases with shock stress [39], making experiment design difficult at higher stresses by significantly shortening the maximum measurement window.

3.2.4 High-Speed Imaging and Digital Image Correlation (DIC)

To capture clear images of the speckle pattern during the dynamic event, precise visualization setup is necessary. The high-speed imaging setup is composed of the HPV-X2 camera (Shimadzu, Kyoto, Japan) set to capture images at 10,000,000 frames/second (100 ns inter-frame time, 50 ns exposure time) along with the CAVILUX Smart pulsed, incoherent laser light source (Cavitar, Tampere, Finland) which is synchronized to the camera exposures and pulsed for 50 ns durations. To perform high-magnification imaging with sufficient resolution to capture fine features of deformation at the internal plane,

the camera is equipped with a $0.7 - 4.5$x zoom lens and 2x adapter tube (Navitar, Rochester, New York), which achieved a typical field of view of approximately 2.8×1.8 mm (400×250 pixels). For such a small field of view, the camera is also mounted to a five-degree-of-freedom optical stage which allows precise alignment of the camera's field of view. The high-magnification lens also produces a highly light-starved environment, which is remedied by configuring the laser light source in a back-lit setup to maximize illumination. Additionally, the large curvature of the zoom optic generates image distortions, which are addressed through standard distortion correction procedures. Images are taken of the rigid body translation of the target at several vertical and horizontal distances, and a correction function is computed which regains uniform displacement fields. This correction function is subsequently used for the experimental images as well. Finally, as was discussed in previous work [33], some optical distortions arise resulting from the change in refractive index across the shock front. This is mitigated by aligning the camera lens to the target visualization surface closest to the camera to maximize the parallelism between the two.

Having established a basis for capturing clear images of the speckle pattern in this setting, one must also consider the details of the quantitative imaging technique, DIC. As mentioned above, the internal speckle pattern is generated by randomly distributing toner powder inside a layer of transparent paint, which produces a typical speckle size of $10 - 20\,\mu$m. This is an ideal size compared to the camera's spatial resolution of $7\,\mu$m/pixel. Correlation of the speckle pattern images is performed with the Vic-2D software [40] (Correlated Solutions, Columbia, South Carolina) along with the built-in distortion correction algorithm mentioned earlier. For the sake of consistency between experiments, the same correlation parameters are used to post-process each experiment: 21 pixel subset size (SS), 1 pixel step size (ST), and strain is computed using a 15 pixel, 90% center-weighted, Gaussian strain window (SW). Using these settings to correlate ambient, rigid body translation images, the noise floor for the DIC measurements is computed to be 0.4% strain (based on the standard deviation of the longitudinal strain distribution). Further, the effects of the subset size, step size, and strain window size can be summarized through the virtual strain gage length [41] (L_{VSG}), computed as

$$L_{\mathrm{VSG}} = (SW - 1)ST + SS \tag{3.2}$$

which is representative of the total filtering applied to the physical features during the DIC analysis. This parameter is used in Section 3.3 and Appendix 3.B to discuss DIC measurements of fine features such as shear bands.

Table 3.1: Summary of pore collapse experiments.

Shot Number	Flyer Material	Flyer Thickness [mm]	Target** Thickness [mm]	L_{Pore}*** [mm]	Impact Velocity V_i [m/s]	Shock Stress σ_{11} [GPa]	Shock Speed U_s [m/s]	Tilt [mrad]
Pore–0.4	PMMA	13.069 ± 0.002	15.938 ± 0.027	5.4	227 ± 7	0.41 ± 0.01	3036 ± 6	N/A
Pore–0.6*	Al 7075	12.893 ± 0.003	22.878 ± 0.004	7.1	213 ± 5	0.62 ± 0.02	3106 ± 4	0.78
Pore–0.8	Al 7075	12.845 ± 0.002	15.793 ± 0.022	5.2	263 ± 10	0.78 ± 0.03	3130 ± 4	3.8
Pore–1.0	Al 7075	12.945 ± 0.002	16.492 ± 0.008	5.1	334 ± 8	0.99 ± 0.02	3144 ± 1	3.4

*An Al 7075 buffer plate (thickness 0.601 ± 0.001 mm) was glued to the target impact surface for this experiment.

**All target plates were manufactured from PMMA.

***L_{Pore} indicates the distance from impact surface to the front edge of the pore.

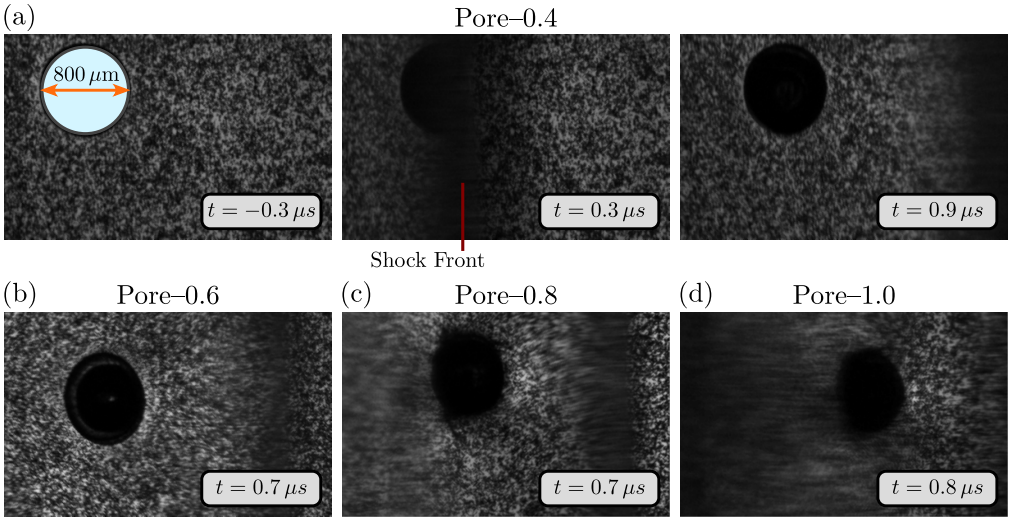

Figure 3.3: Deformation images at the internal mid-plane for all pore collapse experiments. Each experiment is performed with a single spherical pore that is 800 μm in diameter. (a) Experiment Pore–0.4. Three time instances are shown: before shock (left), during shock (middle), and after shock (right). (b-d) Pore–0.6, Pore–0.8, and Pore–1.0 after shock loading. $t = 0$ corresponds to the time of arrival of the shock at the pore.

3.3 Results

Four pore collapse experiments were conducted at shock stresses ranging from $0.4 - 1.0$ GPa. The shock conditions were controlled primarily by varying the impact velocity, as well as changing the flyer plate material as-needed. For all the experiments, the pore size was kept constant at 800 μm diameter while the shock stress was varied. Details of the specimen geometries and loading

conditions are summarized in Table 3.1. The naming convention adopted for numbering the experiments indicates the experiment type and nominal shock stress (e.g., Pore–0.6 refers to the pore collapse experiment under nominally 0.6 GPa shock stress).

3.3.1 Deformation Images, Longitudinal and Lateral Strain, and Pore Volume

For each experiment, the entire shock loading process is captured via high-speed imaging, beginning with the ambient unshocked state and ending with the arrival of release waves which concludes the measurement window. A representative set of images for all four experiments is shown in Fig. 3.3, and Fig. 3.3a illustrates the evolution of Pore–0.4. From left to right, one can see the unshocked (ambient) condition, the shock wave (dark band) passing the pore (propagating from left to right), and the shocked state. Though not shown here, it is also possible to briefly visualize the radial wave reflection off of the pore surface. Similarly, Fig. 3.3b-d show one frame of the shocked state for each of the remaining experiments, as the details of evolution are generally difficult to ascertain from the deformation images alone. DIC analysis will reveal more insight to the evolution of the shocked state. In general, the deformation images reveal a clear progression from nearly indiscernible collapse in Pore–0.4 to significant collapse in Pore–1.0. They also show development of fracture at the pore interface in Pore–0.8, which will be discussed further in Section 3.3.3.

After capturing deformation images with a clear speckle pattern after shock arrival, the images were processed via DIC, computing the displacement field and subsequently the Lagrangian strain measures. While blurry regions (and fracture, in the case of Pore–0.8) obscured the speckle pattern in Pore–0.8 and Pore–1.0, the image quality in Pore–0.4 and Pore–0.6 enabled excellent correlation. To analyze the strain concentrations around the collapsing pore, line slices are taken vertically and horizontally through the center of the pore. A schematic of this concept is shown in Fig. 3.4a along with an example using full-field DIC data from Pore–0.4. The results for longitudinal (ε_{11}) and lateral (ε_{22}) strain along both the vertical and horizontal lines are presented in Fig. 3.4b. The plots summarize the shocked material response (unshocked measurements of zero strain are omitted). Data for each experiment is visu-

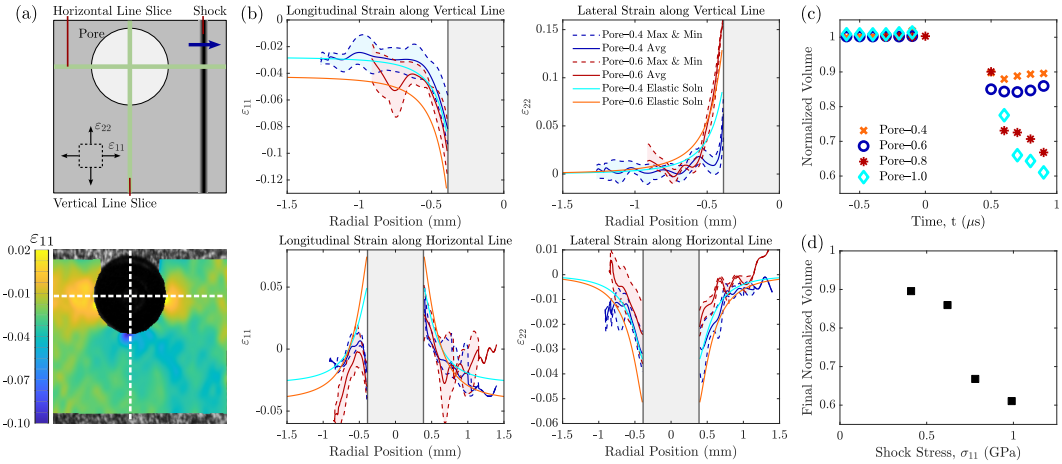

Figure 3.4: Line slice comparison to elastic solution and pore volume analysis. (a) Schematic of pore, shock direction, and line slices; DIC snapshot of longitudinal strain (ε_{11}) with line slice locations overlaid. (b) Experimental strain measurements (ε_{11}, ε_{22}) taken along line slices and plotted along with corresponding static elastic solution (Appendix 3.A). Experimental data of the shocked material state at each radial location along the line slice is averaged over all time instances after shock-loading (solid curve) and bounded by the minimum and maximum measurements (dashed curves). (c) Normalized pore volume evolution for each pore collapse experiment. Data is missing from $t = 0\,\mu$s to $t = 0.4\,\mu$s because the shock front occludes the camera vision of the pore during these time instances, preventing volume measurements. (d) Final measured normalized volume for each experiment.

alized by the strain averaged over the shocked time instances at each spatial location along the line slice (solid curve) and the shaded envelope of all measurements in time, which is bounded by the maximum and minimum (dashed curves). Each plot includes the experimental results combined from all time instances after the shocked state was achieved, along with the static, elastic solution for uniaxial strain compression of a spherical pore. This is determined using the elastic solution for static uniaxial stress loading imposed on a spherical pore, first derived by Southwell [42]. The solution is superposed to incorporate the shock stress and lateral confining stress (Appendix 3.A, Eq. (3.A.5)) associated with the plate impact experiment's uniaxial strain loading condition. Elastic parameters for PMMA under dynamic compression with confinement are used [43]; further details can be found in Appendix 3.A.

The line slice plots reveal good overall agreement between experimental and theoretical results, demonstrating the ability to accurately capture strain concentrations as large as 16%. In particular, Pore–0.4 is expected to be nearly

completely elastic because the nominal 0.41 GPa loading is well below the Hugoniot elastic limit of 0.8 GPa [44]. The resulting strain measurements reinforce this assumption, as they coincide very closely with the elastic solution. The quality of the DIC data is particularly good along the vertical line, while more noise is present along the horizontal line. This likely arises due to diffraction and the shock reflections off the pore at the front and back, leading to a complex deformation state. While agreement with the elastic solution provides confidence in the experimental result, deviations from the elastic solution are more instructive. In particular, the longitudinal strain along the horizontal line reveals a significant discrepancy from the elastic solution. The strain near the back of the pore (positive radial position) coincides with the theory, but material near the front of the pore (surface upon which the shock impinges first) undergoes much more significant compressive strain in both Pore–0.4 and Pore–0.6. This is a clear indication of the shielding effect generated by the pore when a shock wave interacts with it. That is, the front of the pore is subjected to the full extent of the shock stress, but the pore diffracts (reflects) the wave because of the traction-free boundary condition at the pore surface (owing to the impedance mismatch between PMMA and void). This leaves the region immediately behind the pore shielded from the shock, thus experiencing much less of the imposed loading. This phenomena is consistent with the prior observations of stress wave loading in gels [21].

Turning briefly to the collapsing pore itself, rather than the near-field deformation, it is worth noting that the collapsed geometry is close to an ellipsoid rather than a spheroid. This occurs, especially in this strength-dominated, low pressure regime because the shock stress is rather large compared to the lateral confining stress, leading to significantly larger deformation in the horizontal (shock) direction than the vertical (transverse) direction. An estimate for the lateral confining stress is given in Eq. (3.A.5) using elastic theory, though this only holds near the elastic regime where minimal inelastic deformation develops. This difference becomes less severe at higher stresses (e.g., Pore–1.0) where more substantial vertical collapse begins to develop. Yet even at very high pressures (hydrodynamic regime), as reported by Escauriza et al. for spherical pores in PMMA, the collapse in the shock direction is more drastic than the lateral directions, leading eventually to the development of jetting [28].

Additionally, it is possible to calculate the volume of the pore during its collapse. This is accomplished by thresholding the deformation images to produce a black and white image, from which the pore boundary can be identified using the MATLAB image processing toolbox [45]. The pore boundary is then fit to two partial ellipses, for the left and right sides, as depicted in Fig. 3.8a. Assuming axisymmetric deformation, the volume can be computed as the sum of two ellipsoidal caps. The calculated volume evolution, normalized by the initial volume of the pore, for all four experiments is plotted in Fig. 3.4c. The two lower stress (0.41 and 0.62 GPa) experiments appear to reach a final collapsed volume within the first 1 μs after shock arrival, while the two higher stress experiments may still be evolving. The final measured normalized volume is plotted against the shock stress in Fig. 3.4d. However, because of the limited time for measurements, it is difficult to establish an exact trend for the final collapsed volume. Additional data at higher stresses would be essential to establish a relationship between shock stress and collapsed volume. The work of Escauriza et al. on pores of a larger scale provides substantial discussion of the pore volume evolution at stresses up to 17 GPa, and observes that complete collapse occurs near 1.25 GPa [28].

3.3.2 Shear Localization

Returning to the deformation field surrounding the collapsing pore, the Tresca shear strain is computed,

$$\gamma_{\text{Tresca}} = \frac{\varepsilon_{\text{I}} - \varepsilon_{\text{III}}}{2} \tag{3.3}$$

which provides insights to possible localization mechanisms occurring. The symbols ε_{I} and ε_{III} denote the maximum and minimum principal strains. The full-field shear strain evolution is shown in Fig. 3.5. For Pore–0.4 (Fig. 3.5a), strain concentrations emerge which are reminiscent of the classical solution for stress concentrations in an infinite plate with a hole [46], indicating regions of maximum shear near the top and bottom of the pore. In the case of Pore–0.6 (Fig. 3.5b), similar strain concentrations appear after the shock passes the pore, at $t = 0.4 - 0.5\,\mu$s. But, in addition to these concentrations, small bands begin to appear, eventually giving rise, at $t = 0.7\,\mu$s, to a distinct pattern of shear bands emanating from the pore surface. The development of these bands indicates a mechanism of shear localization, via adiabatic shear banding, associated with pore collapse in PMMA. To the authors' knowledge, this work

represents the first *in-situ* observation of shear localization during dynamic pore collapse.

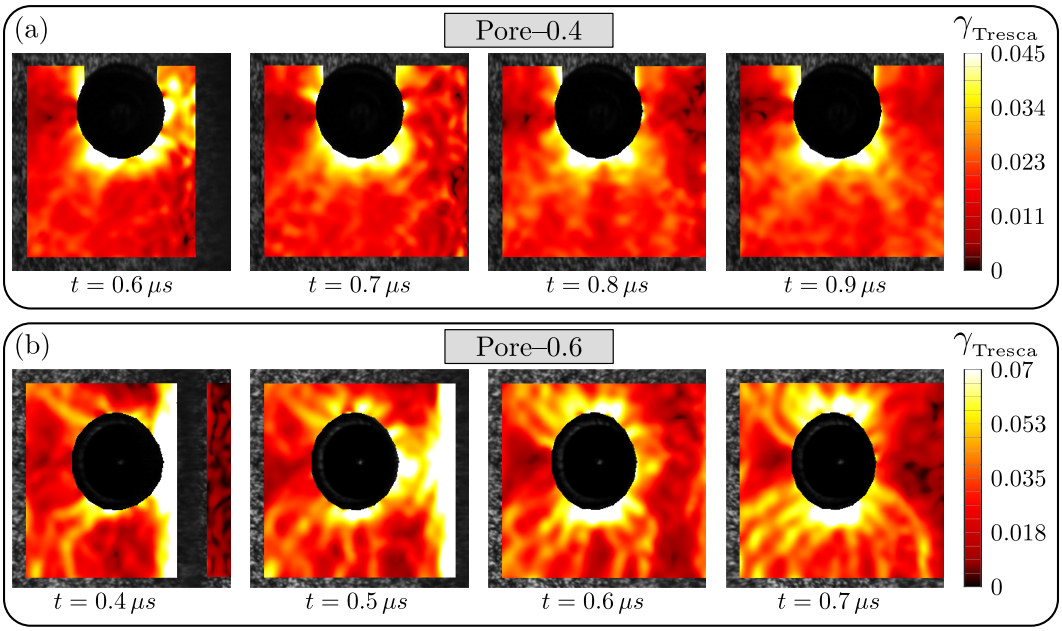

Figure 3.5: Tresca shear strain (γ_{Tresca}, Eq. (3.3)) evolution for two lower pressure experiments after shock loading. (a) Pore–0.4 shows classical strain concentrations developed after shock. (b) Pore–0.6 evidences similar strain concentrations along with the emergence of shear bands emanating from the pore surface.

Because adiabatic shear bands (ASBs) are very fine structures, with a thickness in PMMA of approximately $20\,\mu$m [43], even the high-magnification imaging used here is insufficient to capture the full details of these bands. Instead, using DIC, it is possible to capture the filtered deformation field. This is why the DIC measurements show bands of $\sim 6\%$ strain compared to expected strain of $\sim 100\%$ in ASBs. To confirm that the results shown here are consistent with the filtered deformation measurement of ASBs, a subset size analysis is performed. This analysis investigates the actual strain value by comparing DIC results with various correlation parameters. These correlation parameters (subset size, step size, and strain filter) influence the overall filtering influence of the DIC postprocessing, which is summarized by the virtual strain gage length [41], L_{VSG} (Eq. (3.2)). Results of the subset size analysis indicate that the bands are indeed physical features, and suggest that the actual strain magnitude is of the same order of magnitude as is expected for shear bands. Details of the analysis can be found in Appendix 3.B. Recent work has also identified shear

localization in hole closure experiments via post-mortem analysis for tantalum [27] and Ti-6Al-4V [30].

3.3.3 Fracture

As mentioned above, Pore–0.8 reveals fracture initiation at the pore surface, beginning in the first visible image after the shock passes the pore, which can be seen in Fig. 3.6b. While the emergence of a crack prevents DIC analysis for this experiment, the raw deformation images enable characterization of the dynamic crack evolution during pore collapse. Escauriza et al. have previously observed a similar fracture during pore collapse of PMMA [28]; however, it was unclear whether boundary release waves or wave reflections from the glue interface could have applied necessary tensile loading to initiate mode I fracture. Here, the experimental design enforces nominally uniaxial strain loading conditions during the measurement window. Though the pore introduces a non-uniform stress state, theoretical and computational analyses indicate that the development of localized tension, which could drive mode I fracture, is not possible. Hence, one can conclude the crack observed here arises from shear-driven fracture, which will be further addressed in Sections 3.4 and 3.5.

The crack is identified visually by the black band which propagates forward with increasing time increments. For each image after the shock passes, the crack path is traced and displayed in Fig. 3.6b along with a magnified view of the crack in the inset, where the crack can be seen most clearly. Additionally, the length of the crack as a function of time is shown in Fig. 3.6a. The average crack tip speed, $V_{\text{crack}} \approx 959\,\text{m/s}$ is found to fall between the Rayleigh wave speed and shear wave speed of PMMA (935 and 1000 m/s, respectively [47]). However, the experimental resolution for crack speed measurement is insufficient to distinguish between crack propagation at or just above the Rayleigh wave speed. Most likely, the crack speed has approached near to the Rayleigh wave speed, consistent with the understanding that crack speeds between the Rayleigh and Shear wave speeds are unstable [48, 49]. Further analysis of these results is necessary to unravel the mechanisms driving the fracture initiation point, path, as well as the modality of the fracture itself. This will be discussed in Section 3.5.

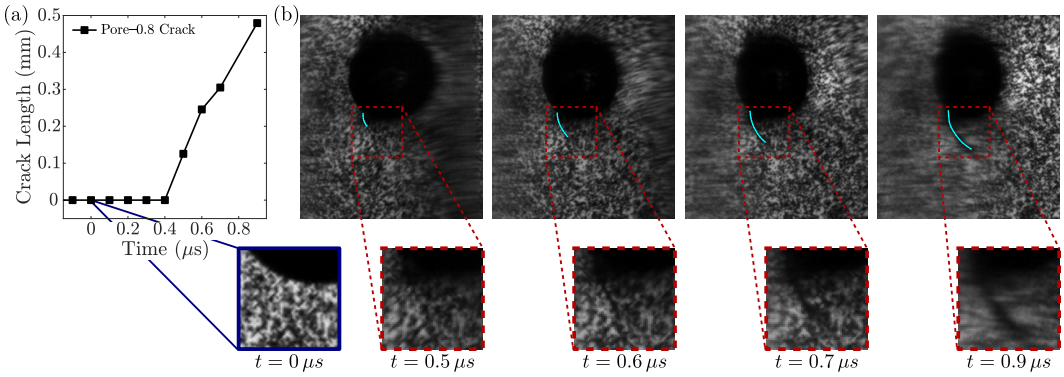

Figure 3.6: Time series of crack evolution in experiment Pore–0.8, with the tracked profile for each image. (a) Crack length evolution. The average crack speed is estimated to be $V_{\text{crack}} \approx 959\,\text{m/s}$. (b) Highlighted crack profile and a magnified view of the crack, provided in the inset.

The initial observations from the experimental results, presented above, indicates the intriguing presence of two failure mode transitions during pore collapse of PMMA which, until now, have not been conclusively observed *in-situ*. The physics governing these transitions will be investigated by carrying out numerical simulations in Section 3.4 along with theoretical modeling in Section 3.5.

3.4 Simulation

Numerical simulations were performed using the finite element software, Abaqus Explicit [50], to augment our understanding of the physics involved in these experiments by providing access to information otherwise unavailable in the experimental data.

3.4.1 Methodology

Simulations were set up with a 2D axisymmetric assumption, mirroring the loading conditions imposed in experiments Pore–0.4, Pore–0.6, and Pore–0.8. Simulation of the conditions in Pore–1.0 has not been conducted because the experiment did not provide information about the deformation or localization behavior with which to compare. Identical geometries were used for the pore size, while shrinking the target and flyer plate lateral dimensions to improve computational times. Because of the smaller lateral dimension, zero-displacement boundary conditions were applied to the lateral boundaries to maintain uniaxial strain and prevent boundary release waves. Additionally,

the flyer plate and target plate geometries were created such that they shared nodes at the impact surface, thereby ensuring perfect contact and zero tilt during the simulated impact. Finally, the model was meshed with quadrilateral elements (CAX4R) in such a way that mitigates computational cost and preserves relevant physics near the pore. This was done by refining the mesh (5 μm element size) near the pore interface such that the adiabatic shear bands observed in experiments could be captured, while coarsening the mesh (20 μm element size) in the remainder of the model geometry. Further details are available in Appendix 3.C. Because of the inherent length scale for localized shear features in finite element analysis (FEA), a mesh convergence study was performed. From this study, reasonable convergence was obtained with respect to the number, mode, and spacing of adiabatic shear bands for all simulations with element size at or below 5 μm. Additionally, axisymmetric simulations were performed because full 3D simulations are prohibitively expensive to perform with the converged mesh size. To confirm that the axisymmetric assumption is reasonable, 3D simulations were performed with a coarse mesh (20 μm) near the pore. This produced deformation and shear band patterns that were axisymmetric. Hence, 2D axisymmetric simulations are used throughout this study in place of full 3D simulations.

3.4.2 Material Models

To account for the thermomechanical behavior of PMMA, adiabatic heating (with Taylor-Quinney coefficient of 1) was implemented for the simulation, along with a calibrated Johnson-Cook plasticity model [51] (Eq. (3.4)) which relates the Mises yield strength (Y) to the equivalent plastic strain ($\bar{\varepsilon}^{pl}$), equivalent plastic strain rate ($\dot{\bar{\varepsilon}}^{pl}$), and temperature ($T$) through the material parameters A, B, n, C, and m. The model is also parameterized by the reference strain rate ($\dot{\varepsilon}_{ref}$), reference temperature (T_r), and melt temperature, (T_m). The Johnson-Cook model incorporates strain rate hardening, strain hardening, and thermal softening behaviors, and has been shown to effectively capture the high-strain rate material response of PMMA under confinement. Material parameters have been calibrated to fit the data of Holmquist et al. [52].

$$Y = \left[A + B\left(\bar{\varepsilon}^{pl}\right)^{n}\right]\left[1 + C\ln\frac{\dot{\bar{\varepsilon}}^{pl}}{\dot{\varepsilon}_{ref}}\right]\left[1 - \left(\frac{T - T_R}{T_m - T_R}\right)^{m}\right] \tag{3.4}$$

Johnson-Cook plasticity is also included for the aluminum 7075 flyer plates; however, it is worth noting that the plastic constitutive model for the flyer plate plays a minimal role in the deformation of the target plate during the window of time of interest. Instead, the standard material parameters for elasticity and wave speeds primarily govern the loading which is imposed on the target during the impact event. These quantities are all implemented in the form of shear modulus, density, and equation of state (EOS) ($U_s - u_p$ relation),

$$U_s = C_0 + Su_p \tag{3.5}$$

where U_s and u_p are the shock speed and particle velocity, respectively, and C_0 and S are material constants. The Mie-Grüneisen parameter, Γ_0, completes the EOS description. Tables 3.2 and 3.3 show all the material parameters implemented in the simulations. It is noted here that two equations of state are used for PMMA, named EOS 1 and EOS 2 to capture the non-linear profile of the shock Hugoniot data at low pressures reported by Barker [53], which is explained in Appendix 3.C. The simulations transition from EOS 1 to EOS 2 at the intersection point at $\sigma_{11} = 0.57\,\text{GPa}$. The EOS for Aluminum 7075 is also fit to appropriate low pressure data [54].

Table 3.2: Parameters for the Johnson-Cook plasticity model used in the simulations.

Material	Model parameters (Eq. (3.4))							
	A [MPa]	B [MPa]	n	C	m	$\dot{\varepsilon}_{ref}$ [1/s]	T_m [K]	T_r [K]
PMMA [52]	210	160	2.95	0.077	0.74	1	398	298
Aluminum 7075 [55]	546	678	0.71	0.024	1.56	1	903	298

3.4.3 Results

Results from the numerical simulations for shock stresses corresponding to the experiments are presented in Fig. 3.7 with the time shifted such that the shock wave arrives at the pore surface when $t = 0$. Equivalent plastic strain (shear strain) is plotted for several time instances to provide a comparison to the

Table 3.3: Material properties and equation of state parameters.

Material	Density ρ_0 [kg/m^3]	Specific Heat c [J/(kg·K)]	Shear Modulus G [GPa]	C_0 [m/s]	S	Γ_0
PMMA (EOS 1) [29, 52–54, 56]	1186	1466	2.19	2770	2.11	0.85
PMMA (EOS 2) [29, 52–54, 56]	1186	1466	2.19	3044	0.36	0.85
Aluminum 7075 [54, 56]	2804	N/A	26.9	5022	1.99	1.97

localized shear response observed in experiments. Upon initial observation, it is clear that the initiation of adiabatic shear bands (ASBs) is almost entirely absent for shock stress of 0.41 GPa (Fig. 3.7a), matching the response from experiment Pore–0.4. At 0.62 GPa shock stress (Fig. 3.7b), a substantial number of distributed ASBs develop. The right-most image in Fig. 3.7b reveals the maximum temperature in the simulated shear bands to be ~ 400 K which corresponds with the prescribed melting temperature in the thermal softening portion of the plasticity model. These features indicate that the first failure mode transition, from diffuse strain concentration in Pore–0.4 to localized shear via adiabatic shear banding in Pore–0.6, is governed simply through thermo-viscoplastic mechanics in the form of the Johnson-Cook model, which was implemented in FEA and replicated the transition. Given that the target material, PMMA, is amorphous, one would expect this to be the case, as the development of ASBs in PMMA cannot be affected by microstructure as has been suggested for polycrystalline metals [57].

Finally, the model at 0.78 GPa shock stress (Fig. 3.7c) evolves toward large deformation, growth of many shear bands, and development of what appears to be a dominant shear band with a very similar initiation point and trajectory as the crack observed in Pore–0.8. This dominant shear band suggests that the subsequent fracture observed experimentally is indeed shear-driven and occurs along the ASB path—enabled by the weakened material state which was realized after undergoing significant shear deformation [58]. The FEA model also reveals a triangular feature resulting from the intersection of two ASBs in Fig. 3.7c at $t = 0.7\,\mu$s. This feature is very similar in location and geometry to that observed experimentally in Pore–0.8 where the crack initiates, which is highlighted in Fig. 3.7d. Again, this reinforces the ability of the FEA

to capture the dominant ASB modes which lead to shear-driven fracture in the experiments. This fracture of a triangular chip has also been recently observed by Lovinger et al. [30] in cylindrical hole closure via post-mortem analysis.

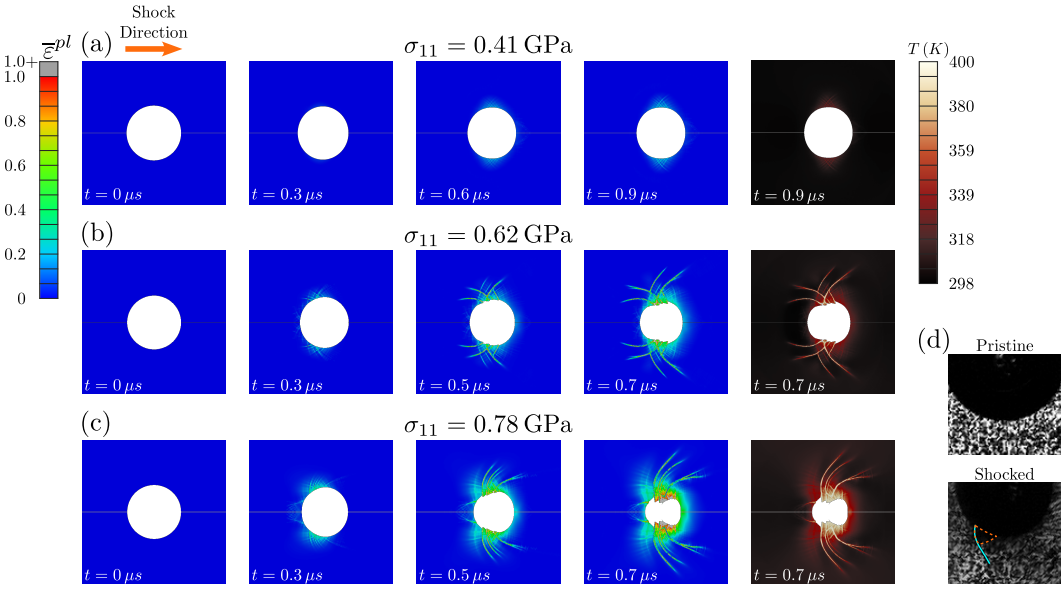

Figure 3.7: Results of numerical (FEA) simulations with loading conditions and measurement times consistent with experiments. (a), (b), and (c) correspond with experiments Pore–0.4, Pore–0.6, and Pore–0.8, respectively. For each simulation, the first four images depict the evolution of the pore and equivalent plastic strain, while the final image shows the temperature field at the last time instance. (d) Highlighted view of the triangular cutout which occurs during fracture in Pore–0.8 and can be compared to (c) at $t = 0.7\,\mu$s.

Regarding the actual distribution and curvature of the ASBs in the 0.62 GPa simulation, it is not clear why the patterns fail to match the experiments. One possible reason is that at a given material location, two orthogonal directions of maximum shear exist, but the mesh may give slight preference toward one direction over the other, leading to the predominant occurrence of shear bands which curve toward the shock loaded direction. While the exact ASB distribution for Pore–0.6 is not captured, and the FEA implementation used here does not attempt to incorporate fracture to compare directly with Pore–0.8, the qualitative replication of failure modes provides helpful insight to the physics of the failure mode transitions. Most notably, the simulations confirm that the transition to adiabatic shear banding is governed by thermo-viscoplastic mechanics, and reinforces the idea that the eventual failure via fracture is indeed shear-driven and is enabled by the weakened material along the dominant ASB. This discussion will be continued along with further in-

vestigation through theoretical modeling next, in Section 3.5, with the goal of understanding the ASB trajectories and driving mechanisms for fracture.

3.5 Discussion

The experiments conducted in this study, along with numerical simulations, have uncovered a distinct transition in failure modes with increasing shock stress. First, shear localization develops via many distributed adiabatic shear bands, and second, fracture occurs along a dominant adiabatic shear band which is enabled by material softening in the shear band. In these experiments on a single, 800 μm diameter pore in PMMA, the first transition was found to occur between 0.41 and 0.62 GPa shock stress, while the second is between 0.62 and 0.78 GPa. However, these transitions are certain to be material dependent, and may have additional dependence on (i) the pore shape and pore size, and (ii) the configuration of an array of pores. With the transitions observed in experiments and supported by simulations, one can now turn to the topic of the driving mechanisms for failure mode transition, initiation locations, and propagation/arrest.

3.5.1 Failure Mode Transitions

As discussed previously, it is clear that the transition to failure via adiabatic shear banding is governed by thermo-viscoplastic mechanics. In particular, even at relatively low shock stresses, the presence of a pore creates large stress concentrations, inducing significant plastic deformation leading to inelastic (plastic) heating and thermal softening [58]. These conditions are ideal for the development of adiabatic shear bands. However, the physics governing the transition from distributed ASBs to the dominance of a single ASB and subsequent fracture is less obvious. Toward understanding this transition, the symmetry of the pore collapse is analyzed, having visually observed a substantial asymmetry in the raw deformation images for Pore–0.8 (Fig. 3.3c). This is accomplished by fitting a partial ellipse to each side of the pore, as was described in Section 3.3.1 and shown in Fig. 3.8a for one image from Pore–0.8. Plotting the ratio of minor axes in Fig. 3.8b, a clear difference emerges between the lower pressure (Pore–0.4 and Pore–0.6) and higher pressure (Pore–0.8 and Pore–1.0) experiments. The lower pressure experiments exhibit fairly symmetric collapse, marked by a ratio of minor axes of the two ellipses (left

and right) close to 1. But the higher pressure experiments display substantial asymmetry, as the left side (on which the shock impinges first) compresses more than the right (which is shielded), leading to a ratio well below 1. It is noteworthy that the ratio does fluctuate, first dipping significantly below 1 in the first frame after the shock has passed the pore (the first data point after losing view of the pore), then rising as the right side compresses after being shock loaded, and finally settling back down as the pore approaches its final steady state shape. This asymmetric collapse behavior is another unique feature of shock compression of pores, compared to the classical symmetric theories [14, 15], static compression, or other transient loadings [35]. This large asymmetry coincides directly with the initiation of fracture in Pore–0.8, which nucleates and propagates a very short distance at $t = 0.5\,\mu$s as shown in Fig. 3.6a, corresponding to the time at which the axes ratio first is measured to be well below 1.

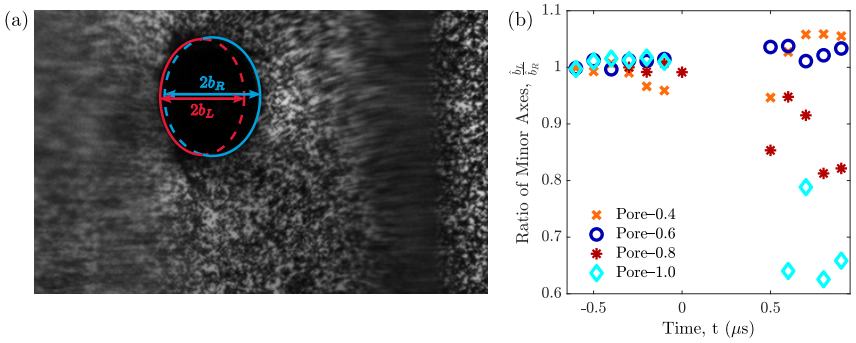

Figure 3.8: Pore collapse asymmetric shape analysis. (a) Example of partial ellipses fit to the collapsing pore to characterize volume and asymmetry of pore shape. b_L and b_R refer to the minor axis length for the left (shock impinging face, red) and right (blue) sides of the pore, respectively. The solid curves correspond to the actual partial ellipse fits to the pore outline, while the dashed curves depict the remaining portion of the ellipses which do not fit the pore outline. (b) The normalized ratio of the minor axes of the left and right ellipses, $\hat{b}_L/\hat{b}_R$, where $\hat{b} = b/b^0$, b_L^0 and b_R^0 are the minor axes lengths of the initial pore left and right sides, respectively; $b_L^0 \approx b_R^0 \approx R$ (nominal pore radius). Note, data is missing from $t = 0\,\mu$s to $t = 0.4\,\mu$s because the shock front occludes the camera vision of the pore during these time instances, preventing ellipticity measurements.

The asymmetry is driven in part by the transient nature of shock loading, in which the left side of the pore is deformed before the right side is fully loaded, leading inherently to a time shift in the amount of deformation on the right side compared to the left. These transients also would drive the failure

initiation location preferentially to the left, rather than the center where the maximum shear should develop in quasistatic loading. However, an additional mechanism, and the reason for which the shocked pore remains asymmetric even after reaching a steady state, are the kinematics imposed by wave interactions with the pore surface. In particular, upon arrival at the pore surface, the shock wave propagates forward, diffracting around the pore and leading to significant longitudinal stress at the top and bottom of the pore. However, at the front of the pore (left side), the shock wave reflects off the pore owing to the free surface (traction-free boundary condition). Associated with this release, and consistent with classical shock physics [59], the particle velocity at the front surface of the pore could be doubled compared to that of the top or bottom. This phenomena arising from wave interactions is the same one by which jets develop at much higher shock stresses, where momentum carries the front surface forward and impinges on the back surface of the pore. Along the surface of the pore between the front and top/bottom, where the surface is neither parallel nor perpendicular to the shock loading direction, a multiaxial response is generated with a partial release. In other material systems, such as copper [26], these kinematics are accommodated through large plastic deformations. Even in PMMA, in the hydrodynamic regime, it is known that spherical pores do eventually develop jets [28] at sufficiently high stresses, likely enabled by shock heating which melts the PMMA. In the most extreme case of the complete absence of strength in the matrix material (i.e., fluids), this phenomena has been well studied and clearly described through the shock bubble interaction problem [60–62]. Here in the strength-dominated regime, however, because of the more brittle nature of PMMA, the kinematic frustration generates large concentrations of shear strain. This leads to shear localization and eventual fracture, instead of developing more diffuse plastic deformation and uniform softening.

Understanding the influence of asymmetric collapse resulting from shock compression helps to explain the transition from distributed ASBs in Pore–0.6 to dominant ASB and shear fracture in Pore–0.8. Interestingly, Pore–1.0 also shows substantial asymmetry, indicating that shear fracture could be present; however, the experimental images are occluded, preventing any conclusive claims. Lovinger et al. observed post-mortem shear fracture in Ti-6Al-4V [30] during hole closure at various shock stresses, indicating that this phenomena is more widespread and not limited only to PMMA or a very specific shock

stress. However, in PMMA it is also possible that the brittle-to-ductile transition which occurs under significant confinement [43] may mitigate the fracture response at higher shock stresses. Coupled with material softening resulting from shock heating at higher shock stresses and the possible suppression of crack propagation via confining stress, another transition from shear fracture may be possible beyond 0.8 GPa shock stress. Finally, it is noteworthy that this fracture behavior could be highly dependent on the spatial scale. The transient loading mentioned above should become negligible for very small pores, and shear localization may become irrelevant when the pore scale approaches the inherent length-scale of ASBs in PMMA (20 μm [43]). Alternatively, at large pore scales (e.g., engineered structures and metamaterials), the effect would likely become more pronounced.

3.5.2 Adiabatic Shear Band Spacing and Paths

The next question to address is that of shear band spacing and paths, which should provide insight to the physics of ASB distribution and self-organization which is observed in Pore–0.6. To this end, the shear bands are tracked in the reference (Lagrangian or undeformed) configuration. This is done by manually estimating one point along each shear band from the DIC data, computing the location of the nearest local maximum shear strain, and tracking the local maxima (shear strain peaks) along the length of the shear bands. The final traced shear bands are overlaid on the Tresca shear strain (Eq. (3.3)) plot in Fig. 3.9b. From there, one can calculate the spacing between each shear band and its neighbors as a function of radial position. These results are presented in Fig. 3.9a along with a comparison to theory.

Following a similar approach as in previous studies [63–66], one calculates the theoretical spacing using the Grady-Kipp model [67]. During deformation, as adiabatic shear bands form, they weaken and flow to very large strains, resulting in an unloading process of the neighboring material. This is the notion which Grady and Kipp capture through a momentum diffusion model, determining the spacing based on the speed of the unloading front. The spacing prediction which results from their analysis [67] has been summarized by Nesterenko et al. [63] as follows:

$$L_{\mathrm{GK}} = 2\left(\frac{9kc}{\dot{\gamma}^3 a^2 \tau_0}\right)^{1/4} \tag{3.6}$$

where k and c are the thermal conductivity and specific heat capacity, respectively. The applied shear strain rate is $\dot{\gamma}$, the flow stress at room temperature is denoted τ_0, and the temperature dependence of the flow stress is characterized through the linear thermal softening parameter, a.

$$\tau = \tau_0[1 - a(T - T_0)] \tag{3.7}$$

Note that the flow stress is defined here as $\tau_0 = \sigma_0/2$, where σ_0 is the yield stress at room temperature under uniaxial stress loading. All relevant parameters are summarized in Table 3.4. The parameters related to thermal softening, τ_0 and a, are fit to the same dataset (yield stress as a function of temperature) used to calibrate the plasticity model for the numerical simulations [52]. Thermal properties, k and c, are taken from the literature [29, 68]. To estimate the applied strain rate, the numerical simulation framework from Section 3.4 is used to simulate the pore collapse event at 0.62 GPa shock stress. The maximum strain rate (near the pore surface) in the simulation is taken to be the estimate for the applied strain rate in the experiments. Because our interest here is in the applied strain rate, neglecting the strain rates inside shear bands, this simulations is conducted without thermal softening, to prevent shear localization.

Table 3.4: Parameters for Grady-Kipp adiabatic shear band spacing model.

Material	k [W/(m·K)]	c [J/(kg·K)]	$\dot{\gamma}$ [s^{-1}]	τ_0 [MPa]	T_0 [K]	a [K^{-1}]
PMMA [29, 52, 68]	0.19	1466	0.45×10^6	53	298	0.0061

Comparing the experimental results from Pore–0.6 to the Grady-Kipp model, one finds close agreement near the pore surface. This suggests that the momentum diffusion mechanism generally captures the physics which govern the spacing of ASBs at their most densely packed location (e.g., the pore surface) during symmetric collapse. This conclusion seems reasonable, at least for the analysis of ASBs which initiate, propagate outward from the pore surface, and attain sufficient strain magnitude such that they are captured via DIC. It remains possible that other ASBs initiate near the pore surface, but the loading and unloading mechanism allows some ASBs to fully develop while others die out. Such existence of very small ASBs which are unable to compete with the growth of neighboring ASBs is well known [64]. A numerical study [66] by

Zhou et al. distinguished between initiated ASBs and developed ASBs, finding the Grady-Kipp model to predict the spacing of developed shear bands, while other models [69, 70] performed better when considering the spacing between all initiated shear bands. Finally, considering the Pore–0.8 GPa experiment, one dominant ASB develops, and fracture occurs along this shear band (Figs. 3.6 and 3.7c). However, this does not preclude other ASBs from developing. This cannot be captured in experiment because the fracture prevents DIC analysis of the remaining deformation field. Additionally, one would expect that fracture would serve to unload the material even more effectively than shear bands, leading to the conclusion that other ASBs could possibly arrest in the presence of a dominant shear fracture, such as the one seen in Pore–0.8.

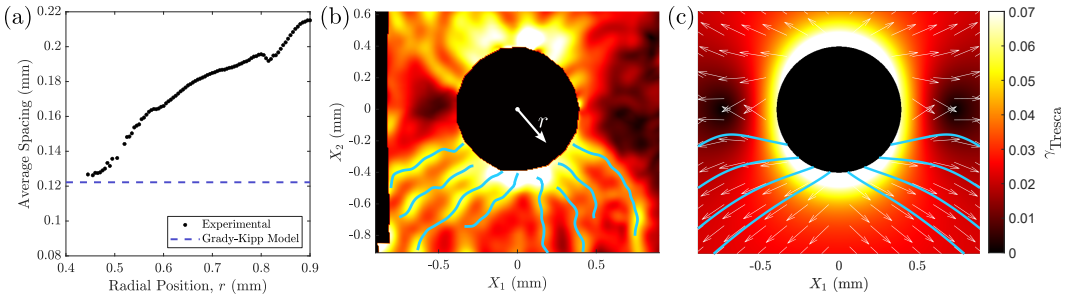

Figure 3.9: Comparison of shear band spacing and paths: experiments and theory. (a) Experimental data for the spacing between tracked, developed ASBs in Pore–0.6 are compared to the theoretical prediction of Grady and Kipp [67]. (b) DIC results for Tresca shear strain, γ_{Tresca}, in experiment Pore–0.6 at $t = 0.7\,\mu$s with traced ASB paths outlined in light blue. Results are shown in the reference (undeformed) configuration. (c) Elastic solution for Tresca shear strain, γ_{Tresca}. Directions of maximum shear indicated by white arrows. Light blue curves represent streamlines along the path of maximum shear, beginning at the estimated initiation sites for ASBs in experiment Pore–0.6.

Having considered throughout this section the topics of ASB and crack initiation as well as the spacing between shear band initiation sites, one can now turn to the topic of shear band paths. Recalling the elastic solution introduced along with the line slices in Fig. 3.4, the full field solution is considered, with a particular interest in the directions of maximum shear which would direct the shear band paths. Details of the elastic solution are provided in Appendix 3.A. Figure 3.9b-c summarizes the relevant results, first reproducing the representative experimental image of distributed shear bands in Pore–0.6

(Fig. 3.9b). Then the Tresca shear strain (Eq. (3.3)) deduced from the elastic solution is plotted in Fig. 3.9c for a far field loading, $\sigma_0 = 0.62$ GPa, along with corresponding lateral confining stress superposed. Additionally, the direction of maximum shear, the bisection of the first and third principal directions, is indicated by white arrows.

Qualitative agreement between the dynamic experimental and elastostatic theoretical Tresca strain field is clear to visualize, with major concentrations of similar magnitude on the top and bottom of the pore. The primary interest, however, is in the directions of maximum shear. To compare with experimental traces of the shear band patterns, the average angular spacing between the eight bands at the pore surface is calculated and found to be 16 degrees. Thus, initiation points are estimated to be evenly spaced 16 degrees apart, and symmetric across the X_2 axis. Streamlines are computed, initiating at these sites and following the path of maximum shear, and are plotted as blue overlaid curves. While not a perfect match to the experiments, it is interesting to see elastic theory capture the qualitative response of such complex phenomenon. Considering the differences in the initial shock compressed loading state to this static elastic solution, as well as the dynamic evolution involving the development of shear bands and subsequent unloading of the neighboring regions, it is expected that the actual response will not follow the elastic solution exactly. Still, it offers a good comparison and insights for the localization behavior of pores under extreme loading.

3.5.3 Crack Path and Arrest

To investigate the crack path and arrest, a similar procedure, which uses the elastic solution to determine the direction of maximum shear, is undertaken for the 0.78 GPa case (Pore–0.8), the results from which are shown in Fig. 3.10. Estimating the initiation point is more straightforward for Pore–0.6, because the DIC results allow analysis in the reference configuration. Instead, for Pore–0.8, an ellipse is fit to the pore in the deformed state, and the fracture initiation point is manually identified on the fitted ellipse. From there, the angular location along the ellipse is calculated and applied to the circular contour in the reference configuration. Next, the streamline is generated to follow the path of maximum shear. One can imagine based on the results in Fig. 3.9c that the streamline would not resemble the crack path. However, recalling the

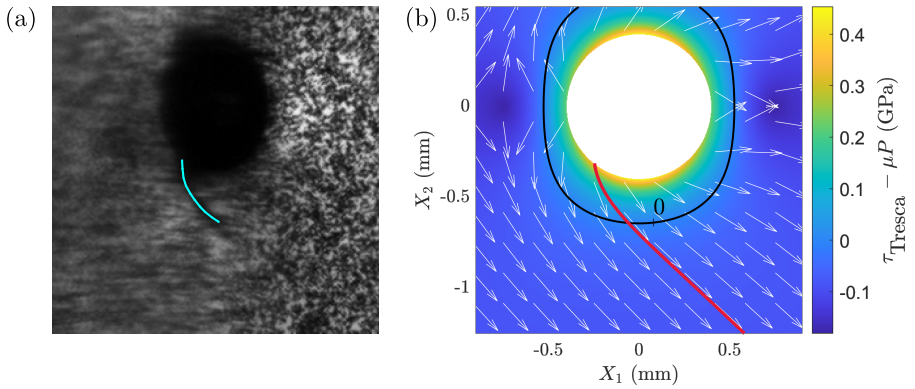

Figure 3.10: Comparison of experimental crack path in Pore–0.8 to the direction of maximum shear predicted by theory. (a) Raw deformation image from experiment Pore–0.8 at $t = 0.9\,\mu$s with shear fracture highlighted in light blue. (b) Elastic solution for driving force: $\tau_d = \tau_{\text{Tresca}} - \mu P$ (Eq. (3.8)) with direction of maximum shear (white arrows) and streamline (red) beginning at the fracture initiation location. Also shown is the contour (black) where the driving force is zero.

definition for direction of maximum shear and the fact that principal directions are independent of sign, there exists an alternative set of maximum shear directions which is orthogonal to the first set. Computing the streamline with this alternative set of maximum shear vectors, the result in Fig. 3.10b is achieved, which corresponds nearly identically to the fracture path observed in Pore–0.8 (Fig. 3.10a). This is another clear indication that fracture indeed occurs in shear and along the path of a shear band. Furthermore, one can consider the driving force for crack propagation, and compare it with the final crack tip location at $t = 0.9\,\mu$s. At this time, it appears the crack tip has arrested, as the subsequent images show no evidence of further propagation. The work by Lovinger et al. [30] also indicates crack arrest in Ti-6Al-4V for several experiments, though at higher pressures the crack propagates through to the boundary of the specimen. A simplistic shear driving force (τ_d) on the crack is considered:

$$\tau_d = \tau_{\text{Tresca}} - \mu P \tag{3.8}$$

where μ is the coefficient of friction, taken to be 0.3 [71], τ_{Tresca} is the Tresca shear stress defined in Eq. (3.9), and P is the pressure (2D), or compressive loading normal to the path of maximum shear, defined in Eq. (3.10). Compressive stress is taken to be negative, σ_{I} is the largest principal stress, and σ_{III} is the smallest principal stress. Note that compressive pressure (P) is taken to be positive here.

$$\tau_{\text{Tresca}} = \frac{\sigma_{\text{I}} - \sigma_{\text{III}}}{2} \tag{3.9}$$

$$P = \frac{-\left(\sigma_I + \sigma_{III}\right)}{2} \tag{3.10}$$

Such a failure criterion (Eq. (3.8)) has been considered before in numerical models for fracture of brittle materials [72] and to understand failure of brittle materials under confinement [73]. It is assumed that when the driving force goes to zero, the shear crack would stop propagating forward. This driving force is plotted as the color map in Fig. 3.10b, along with a black contour curve where the driving force is zero. Hence, the shear fracture arrest can be predicted to occur near the intersection of the streamline and the zero-driving force contour. As it turns out, this location coincides very closely with the experimental result of Pore–0.8. This finding indicates that the driving force (Eq. (3.8)) is indeed a good estimate for shear fracture behavior in these experiments. It also clarifies the mechanism for the crack arrest observed in Pore–0.8, and possibly in the recent results on hole closure in Ti-6Al-4V [30].

3.6 Conclusion

In summary, plate impact pore collapse experiments were conducted at shock stresses of $0.4 - 1.0\,\text{GPa}$, using the recently developed internal DIC technique to perform quantitative measurements of deformation in shock compression experiments [33]. These experiments led to the first *in-situ* observation of shear localization during pore collapse via adiabatic shear banding, and also confirmed the previous *in-situ* [28] and post-mortem [30] observations of crack nucleation from the pore surface. From these insights, two failure mode transitions were observed as the shock stress increased: first, from diffuse strain concentration to failure via adiabatic shear localization, and second, to dynamic fracture. Numerical simulations demonstrated that thermo-viscoplastic modeling qualitatively captures these failure mode transitions. Further, they confirmed the fracture at $0.78\,\text{GPa}$ to be shear-driven fracture (mode-II) and indicated the development of a dominant shear band at high pressures which enabled fracture through the weakened material inside the shear band.

Analysis of the pore asymmetry evolution during collapse demonstrated a correlation between large asymmetry in the collapsed pore shape (which arises from wave interactions with the pore) and nucleation of dynamic fracture. It

is proposed that the wave interactions and subsequent asymmetric collapse create shear strain concentrations which lead to the development of a dominant ASB. The ASB effects a partial stress (energy) release, and eventually gives way to shear fracture that provides an additional stress (energy) release. It also accommodates the large deformations imposed by the shock wave interactions with the pore and surrounding material. The physics governing the distribution of ASBs at 0.62 GPa are clarified through comparison of ASB spacing with the theoretical model proposed by Grady and Kipp [67], which fits well to the experimentally measured spacing of developed shear bands at the pore surface. Thus, the fundamental mechanism in the model: unloading of nearby material through the development of ASBs, which is captured through a momentum-diffusion model [67], should also govern the number and spacing of developed shear bands at the pore surface.

Static elastic theory helped elucidate the physics which determine the paths and arrest of ASBs and cracks. The direction of maximum shear is found to effectively replicate the paths which the ASBs and the crack follow, providing a simple and reasonable method for predicting and understanding the failure paths during pore collapse. Finally, using a simple estimate (Eq. (3.8)) for the driving force for shear fracture, the arrest location of the crack tip can be accurately replicated.

Future work aspires to extend the fundamental understanding of the deformation and failure for heterogeneous materials beyond a single pore. Extending the experimental technique, and leveraging the insights gained in this work, one could investigate the interactions between multiple pores in various configurations. Additionally, the influence of pore size on the pore collapse phenomenon and its associated deformations and failure modes, is likely to yield intriguing results. Synthesis of these types of experiments and implementation in multiscale modeling may also greatly enhance our understanding of the underlying mechanisms for the continuum response of porous materials. Additionally, understanding the role of hard inclusions—the fundamental building block of particulate composites—on the neighboring matrix material is of similar interest. Finally, implementing the technique presented here with phase contrast imaging at a synchrotron x-ray source could minimize the issues associated with optical distortions, enable investigation of longer loading periods and higher stresses, and enlarge the list of material candidates for study.

APPENDIX

3.A Elastic Solution for a Pore Subjected to Multiaxial Loading

The general solution for static, uniaxial stress loading of an infinite, isotropic, linear elastic body with a spherical pore inside, derived by Southwell, [42] is shown in Eqs. (3.A.1)–(3.A.4). The notation is adapted to suit the convention for this work, and uses the spherical coordinate system (centered at the pore center) depicted in Fig. 3.A.1a, where r is the position along the radial coordinate, θ is the polar angle, and ϕ is the azimuthal angle. Figure 3.A.1b shows a two-dimensional view at the plane of interest ($X_3 = 0$ or $\theta = \pi/2$; comparable to the experimental speckled mid-plane), with an arbitrary applied longitudinal stress, $\sigma_{11} = \sigma_0$. Note that R represents the nominal initial pore radius. Values for the elastic parameters (Young's modulus, $E = 5.76\,\text{GPa}$, and Poisson's ratio, $\nu = 0.42$) are taken for PMMA under dynamic loading with confinement [43].

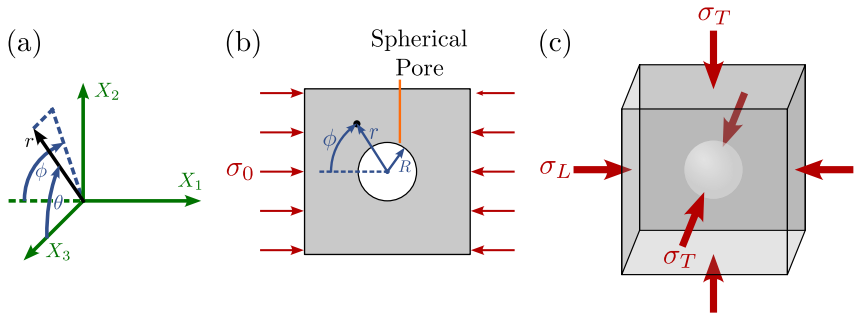

Figure 3.A.1: Schematic for elastic solution of a spherical pore in an infinite body. (a) Spherical and Cartesian coordinate systems overlaid. (b) 2D diagram of uniaxial stress ($\sigma_{11} = \sigma_0$) static loading on body with a spherical pore. 2D view is shown at the mid-plane ($X_3 = 0$, $\theta = \pi/2$). (c) Superposition of shock (longitudinal) stress, $\sigma_{11} = \sigma_L$, and lateral (transverse) confining stress, $\sigma_{22} = \sigma_{33} = \sigma_T$.

$$\begin{aligned}\sigma_{rr} &= \sigma_0 \left\{ \cos^2\phi + \frac{1}{14-10\nu}\frac{R^3}{r^3}\left[-38 + 10\nu + 24\frac{R^2}{r^2} + \left(50 - 10\nu - 36\frac{R^2}{r^2}\right)\sin^2\phi \right] \right\} \\ &= \sigma_0 K_{rr}(\phi, r)\end{aligned} \tag{3.A.1}$$

$$\sigma_{\theta\theta} = \frac{\sigma_0}{2\left(7-5\nu\right)}\frac{R^3}{r^3}\left[9-15\nu-12\frac{R^2}{r^2}-15\left(1-2\nu-\frac{R^2}{r^2}\right)\sin^2\phi\right] = \sigma_0 K_{\theta\theta}\left(\phi,r\right) \tag{3.A.2}$$

$$\begin{aligned}\sigma_{\phi\phi} &= \sigma_0\left\{\sin^2\phi+\frac{1}{2\left(7-5\nu\right)}\frac{R^3}{r^3}\left[9-15\nu-12\frac{R^2}{r^2}-\left(5-10\nu-21\frac{R^2}{r^2}\right)\sin^2\phi\right]\right\}\\ &= \sigma_0 K_{\phi\phi}\left(\phi,r\right)\end{aligned} \tag{3.A.3}$$

$$\sigma_{r\phi} = \frac{-\sigma_0}{2}\sin 2\phi\left\{1+\frac{1}{2(7-5\nu)}\frac{R^3}{r^3}\left[10\left(1+\nu\right)-24\frac{R^2}{r^2}\right]\right\} = \sigma_0 K_{r\phi}\left(\phi,r\right) \tag{3.A.4}$$

This solution can then be superposed to determine the solution under uniaxial strain conditions which are characteristic for plate impact experiments. The longitudinal stress (σ_L), is taken as the magnitude of the shock stress in the corresponding experiment, and the transverse, confining stress (σ_T) is imposed in the lateral directions, as depicted in Fig. 3.A.1c. The confining stress, σ_T, is calculated based on the elastic Poisson's ratio, ν,

$$\sigma_T = \frac{\nu}{1-\nu}\sigma_L. \tag{3.A.5}$$

The elastic confining stress also provides a good estimate for the lateral confining stress which is present in the shock experiments, the effect of which is discussed in Section 3.3.1. The superposition procedure using the fundamental solution [42] in Eqs. (3.A.1)–(3.A.4) leads to the solution in Eqs. (3.A.6)–(3.A.10) for the uniaxial strain loading of the plate impact experiments ($\sigma_{11} = \sigma_L$, $\sigma_{22} = \sigma_{33} = \sigma_T$).

$$\sigma_{rr}(\sigma_L,\phi,r) = \sigma_L K_{rr}\left(\phi,r\right)+\sigma_T K_{rr}\left(\phi-\frac{\pi}{2},r\right)+\sigma_T K_{rr}\left(\phi=\frac{\pi}{2},r\right) \tag{3.A.6}$$

$$\sigma_{\theta\theta}(\sigma_L,\phi,r) = \sigma_L K_{\theta\theta}\left(\phi,r\right)+\sigma_T K_{\theta\theta}\left(\phi-\frac{\pi}{2},r\right)+\sigma_T K_{\phi\phi}\left(\phi=\frac{\pi}{2},r\right) \tag{3.A.7}$$

$$\sigma_{\phi\phi}(\sigma_L,\phi,r) = \sigma_L K_{\phi\phi}\left(\phi,r\right)+\sigma_T K_{\phi\phi}\left(\phi-\frac{\pi}{2},r\right)+\sigma_T K_{\theta\theta}\left(\phi=\frac{\pi}{2},r\right) \tag{3.A.8}$$

$$\sigma_{r\phi}(\sigma_L, \phi, r) = \sigma_L K_{r\phi}(\phi, r) + \sigma_T K_{r\phi}\left(\phi - \frac{\pi}{2}, r\right) \tag{3.A.9}$$

$$\sigma_{r\theta}(\sigma_L, \phi, r) = \sigma_T K_{r\phi}\left(\phi = \frac{\pi}{2}, r\right) \tag{3.A.10}$$

Finally, the stress state is converted to Cartesian coordinates and rotated to the principal frame (σ_{I}, σ_{II}, σ_{III}), from which Tresca shear stress and the direction of maximum shear can be determined. The stresses are also converted to strains through the generalized Hooke's law,

$$\varepsilon_{ij} = \frac{1}{E}\left[(1+\nu)\,\sigma_{ij} - \nu\delta_{ij}\sigma_{kk}\right]. \tag{3.A.11}$$

The results derived in this section are used in Figs. 3.4, 3.9, and 3.10 and the corresponding discussion and analysis.

3.B Effect of DIC Subset Size on Measured Strain in Shear Bands

Digital image correlation (DIC) has an inherent filtering characteristic in the method, which must be taken into account, especially when investigating features of very fine spatial scale, as is the case when dealing with shear localization. To properly investigate the role of filtering on the DIC measurements and to make a comparison to the actual physical strain in the deformed body, one must carry out a DIC subset size analysis. The general idea is to compare the DIC measurement results when using various correlation settings, and compare the convergence of the results as a function of the filter size. The effective filter size can be summarized by the virtual strain gage length [41] (Eq. (3.2)),

$$L_{\mathrm{VSG}} = (SW - 1)ST + SS.$$

If the calculated strain magnitude converges for a sufficiently small virtual strain gage length, then it is considered the actual strain magnitude. However, if no convergence is reached, then the largest calculated strain is taken as a lower bound for the actual strain magnitude, and the actual feature size is considered to be smaller than the smallest virtual strain gage length used.

In the case of the shear bands in Pore–0.6, the shear strain along a semicircular contour is considered, as shown in Fig. 3.B.1a. When projected into one dimension in Fig. 3.B.1b, the shear bands can be seen as peaks, which makes

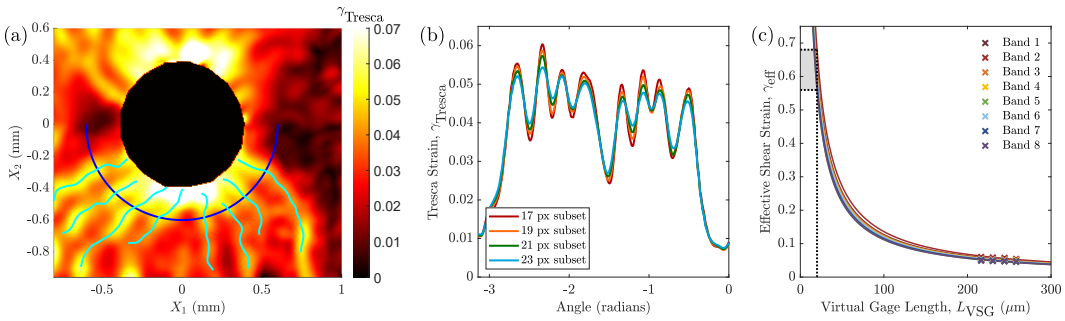

Figure 3.B.1: DIC subset size analysis for Pore–0.6. (a) Tresca shear strain contours at $t = 0.7\,\mu$s are shown in the reference (undeformed) configuration. The semicircular blue curve represents the contour (at $r = 0.6\,$mm) along which the full-field shear strain data is projected. (b) Projection of shear strain along semicircular contour for various subset sizes (strain window and step size are fixed at 15 and 1 pixels, respectively). Lack of convergence for small subset size indicates physical nature of features and determines the actual strain to be larger than calculated. (c) Extrapolation of DIC measurements to estimate actual shear strain magnitude.

visual inspection for various virtual strain gage lengths possible. It is observed that convergence is not achieved, indicating the bands are indeed a physical feature with large strain magnitude and small thickness, and also not a DIC artifact. Specifically, it is clear that the features are smaller than $217\,\mu$m and have strain magnitudes generally larger than the measured 6% strain. Because DIC strain measurements scale as $\gamma \propto 1/L_{\text{VSG}}$, one can roughly estimate the actual strain magnitude via extrapolation, if the feature length scale is known. In this case, the size of the shear band is taken to be $20\,\mu$m based on prior postmortem measurements of plugged PMMA samples [43]. Further assuming uniform strain in the shear band, one can fit a curve to the DIC measurements and determine the intersection at $L_{\text{VSG}} = 20\,\mu$m, as is shown in Fig. 3.B.1c. Such a procedure suggests the actual strain magnitude ($\sim 60\%$) to be on the correct order of magnitude expected for an ASB. While this estimate of actual shear strain is admittedly a large extrapolation, it is not suggested as a quantitative measurement of strain in the shear bands. The purpose of this analysis is to demonstrate the importance of DIC correlation and filtering parameters, and to illustrate the particularly large influence of filtering on fine features such as adiabatic shear bands. The analysis shows that the DIC clearly captures a significantly filtered measurement of the deformation field, including distinct bands which are likely to have an actual strain on the same order as that of adiabatic shear bands.

3.C Numerical Simulations Details

Numerical simulations were conducted in Abaqus/Explicit [50] to capture the deformation and localization response at shock stresses corresponding to experiments Pore–0.4, Pore–0.6, and Pore–0.8, and to provide additional insights to the experimental results. The numerical modeling framework is described in Section 3.4. Here, additional details are provided for the mesh and equation of state implemented for the simulations.

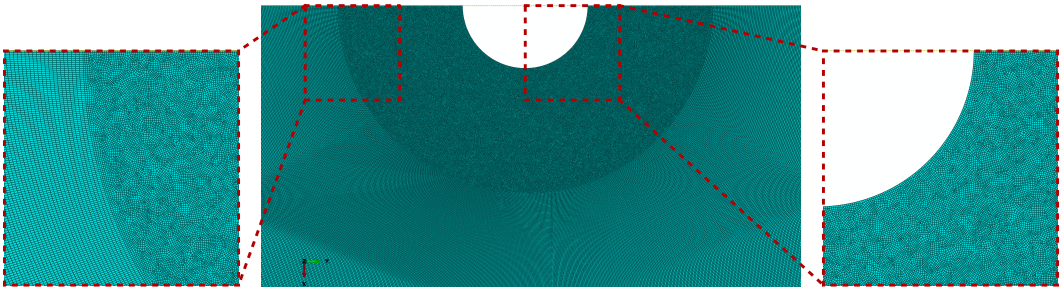

Figure 3.C.1: Visualization of the mesh used for simulations. Insets provide details on the mesh partition (left) and refined mesh near the pore surface (right).

Figure 3.C.1 depicts the mesh which was used in the simulations, where the mesh was partitioned to provide a fine mesh near the pore surface and a coarse mesh in the far field. The region within a 1.2 mm radius from the center of the pore was meshed with nominally 5 μm element size, while the outer region uses a nominally 20 μm element size. A view of the partitioned mesh and the refined mesh is provided in Fig. 3.C.1.

The equation of state (EOS) was defined through a $U_s - u_p$ relation (Eq. (3.5)), which, as described in Section 3.4, was segmented into two linear relations: EOS 1 and EOS 2. The EOS was segmented to capture the non-linear $U_s - u_p$ response which has been well characterized in PMMA [53, 74, 75], while still interfacing with the finite element solver through the traditional linear relation. Figure 3.C.2 shows the two fits along with the tabular data to which they are fit, the intersection between the fits, and the particle velocities of each experiment for reference.

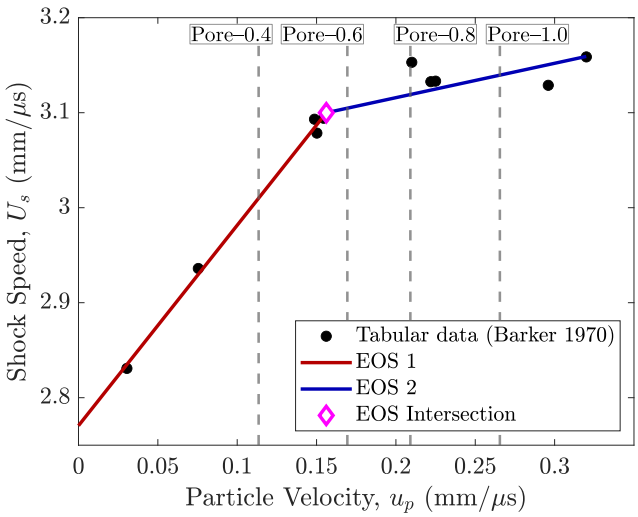

Figure 3.C.2: Plot of $U_s - u_p$ (EOS) relation for PMMA, as was defined in Eq. (3.5) and Table 3.3. Tabulated data from Barker et al. [53] is presented along with two linear fits to the data, which are used in the numerical simulations. The particle velocity for each experiment is denoted with a gray, dashed line for reference.

References

[1] C. M. Tarver, S. K. Chidester, and A. L. Nichols, "Critical conditions for impact- and shock-induced hot spots in solid explosives," The Journal of Physical Chemistry **100**, 5794–5799 (1996).

[2] A. Barua, S. Kim, Y. Horie, and M. Zhou, "Ignition criterion for heterogeneous energetic materials based on hotspot size-temperature threshold," Journal of Applied Physics **113**, 10.1063/1.4792001 (2013).

[3] S. N. Heavens and J. E. Field, "The ignition of a thin layer of explosive by impact," Proceedings of the Royal Society of London. A. Mathematical and Physical Sciences **338**, 77–93 (1974).

[4] C. S. Coffey and S. J. Jacobs, "Detection of local heating in impact or shock experiments with thermally sensitive films," Journal of Applied Physics **52**, 6991–6993 (1981).

[5] R. W. Armstrong, S. G. Bardenhagen, and W. L. Elban, "Deformation-induced hot-spot consequences of AP and RDX crystal hardness measurements," International Journal of Energetic Materials and Chemical Propulsion **11**, 413–425 (2012).

[6] J. E. Field, "Ignition mechanisms of explosives during mechanical deformation," Proceedings of the Royal Society of London. A. Mathematical and Physical Sciences **382**, 231–244 (1982).

[7] J. E. Field, "Hot spot ignition mechanisms for explosives," Accounts of Chemical Research **25**, 489–496 (1992).

[8] N. K. Bourne and A. M. Milne, "The temperature of a shock-collapsed cavity," Proceedings of the Royal Society A: Mathematical, Physical and Engineering Sciences **459**, 1851–1861 (2003).

[9] C. Czarnota, A. Molinari, and S. Mercier, "The structure of steady shock waves in porous metals," Journal of the Mechanics and Physics of Solids **107**, 204–228 (2017).

[10] Z. Lovinger, C. Czarnota, S. Ravindran, A. Molinari, and G. Ravichandran, "The role of micro-inertia on the shock structure in porous metals," Journal of the Mechanics and Physics of Solids **154**, 10.1016/j.jmps.2021.104508 (2021).

[11] E. Chiu, A. Needleman, S. Osovski, and A. Srivastava, "Mitigation of spall fracture by evolving porosity," Mechanics of Materials **184**, 104710 (2023).

[12] R. G. Kraus, D. J. Chapman, W. G. Proud, and D. C. Swift, "Hugoniot and spall strength measurements of porous aluminum," Journal of Applied Physics **105**, 10.1063/1.3133237 (2009).

[13] Z. Lovinger, C. Czarnota, S. Ravindran, C. Kettenbeil, A. Molinari, and G. Ravichandran, "Shock structure and spall behavior of porous aluminum," in AIP Conference Proceedings, Vol. 2272 (Nov. 2020).

[14] W. Herrmann, "Constitutive equation for the dynamic compaction of ductile porous materials," Journal of Applied Physics **40**, 2490–2499 (1969).

[15] M. M. Carroll and A. C. Holt, "Static and dynamic pore-collapse relations for ductile porous materials," Journal of Applied Physics **43**, 1626–1636 (1972).

[16] B. M. Butcher, M. M. Carroll, and A. C. Holt, "Shock-wave compaction of porous aluminum," Journal of Applied Physics **45**, 3864–3875 (1974).

[17] W. Tong and G. Ravichandran, "Dynamic pore collapse in viscoplastic materials," Journal of Applied Physics **74**, 2425–2435 (1993).

[18] C. Czarnota, S. Mercier, and A. Molinari, "Modelling of nucleation and void growth in dynamic pressure loading, application to spall test on tantalum," International Journal of Fracture **141**, 177–194 (2006).

[19] N. K. Bourne and J. E. Field, "Shock-induced collapse of single cavities in liquids," Journal of Fluid Mechanics **244**, 225–240 (1992).

[20] J. P. Dear and J. E. Field, "A study of the collapse of arrays of cavities," Journal of Fluid Mechanics **190**, 409–425 (1988).

[21] A. B. Swantek and J. M. Austin, "Collapse of void arrays under stress wave loading," Journal of Fluid Mechanics **649**, 399–427 (2010).

[22] B. Branch, A. Ionita, B. E. Clements, D. S. Montgomery, B. J. Jensen, B. Patterson, A. Schmalzer, A. Mueller, and D. M. Dattelbaum, "Controlling shockwave dynamics using architecture in periodic porous materials," Journal of Applied Physics **121**, 10.1063/1.4978910 (2017).

[23] J. Lind, A. K. Robinson, and M. Kumar, "Insight into the coordinated jetting behavior in periodic lattice structures under dynamic compression," Journal of Applied Physics **128**, 10.1063/5.0003776 (2020).

[24] B. A. Branch, G. Frank, A. Abbott, D. Lacina, D. M. Dattelbaum, C. Neel, and J. Spowart, "Directional shock diode behavior through the interaction of geometric voids in engineered polymer assemblies," Journal of Applied Physics **128**, 10.1063/5.0029835 (2020).

[25] V. S. Glazkov, O. N. Ignatova, A. N. Malyshev, S. S. Nadezhin, A. M. Podurets, V. A. Raevsky, and O. A. Tyupanova, "Peculiarities of high-rate deformation of copper upon convergence of cylindrical channels by action of shock waves," in AIP Conference Proceedings, Vol. 1195 (2009), pp. 735–738.

[26] J. Lind, M. D. Nelms, A. K. Robinson, M. Kumar, and N. R. Barton, "Examining material constitutive response under dynamic compression and large plastic strains using in situ imaging of hole closure," Acta Materialia **206**, 10.1016/j.actamat.2020.116584 (2021).

[27] M. Nelms, J. Lind, J. Margraf, S. B. Qamar, J. Herrington, A. Robinson, M. Kumar, and N. Barton, "High-rate strength response of tantalum from dynamic hole closure experiments," Journal of Applied Physics **132**, 10.1063/5.0107391 (2022).

[28] E. M. Escauriza, J. P. Duarte, D. J. Chapman, M. E. Rutherford, L. Farbaniec, J. C. Jonsson, L. C. Smith, M. P. Olbinado, J. Skidmore, P. Foster, T. Ringrose, A. Rack, and D. E. Eakins, "Collapse dynamics of spherical cavities in a solid under shock loading," Scientific Reports **10**, 10.1038/s41598-020-64669-y (2020).

[29] N. K. Rai, E. M. Escauriza, D. E. Eakins, and H. S. Udaykumar, "Mechanics of shock induced pore collapse in poly(methyl methacrylate) (PMMA): Comparison of simulations and experiments," Journal of the Mechanics and Physics of Solids **143**, 10.1016/j.jmps.2020.104075 (2020).

[30] Z. Lovinger and R. Kositski, "Shear localization as a damage mechanism in pore collapse under shock compression," International Journal of Impact Engineering **193**, 10.1016/j.ijimpeng.2024.105039 (2024).

[31] D. Hodge, S. Pandolfi, Y. Liu, K. Li, A. Sakdinawat, M. Seaberg, P. Hart, E. Galtier, D. Khaghani, S. Vetter, C. B. Curry, F.-J. Decker, B. Nagler, H. J. Lee, C. Bolme, K. Ramos, P. M. Kozlowski, D. S. Montgomery, M. S. Dayton, L. Dresselhaus-Marais, S. Ali, L. D. Claus, M. O. Sanchez, T. Carver, R. L. Sandberg, and A. Gleason, "Visualization of shocked material instabilities using a fast-framing camera and XFEL four-pulse train," in X-ray Nanoimaging: Instruments and Methods V, Vol. 11839 (International Society for Optics and Photonics, 2021), p. 1183908.

[32] M. A. Sutton, J. J. Orteu, and H. Schreier, *Image correlation for shape, motion and deformation measurements: Basic concepts, theory and applications* (Springer US, 2009), pp. 1–321.

[33] B. P. Lawlor, V. Gandhi, and G. Ravichandran, "An internal digital image correlation technique for high-strain rate dynamic experiments," Experimental Mechanics **65**, 407–419 (2025).

[34] T. A. Berfield, J. K. Patel, R. G. Shimmin, P. V. Braun, J. Lambros, and N. R. Sottos, "Micro-and nanoscale deformation measurement of surface and internal planes via digital image correlation," Experimental Mechanics **47**, 51–62 (2007).

[35] A. McGhee, J. Yang, E. C. Bremer, Z. Xu, H. C. Cramer, J. B. Estrada, D. L. Henann, and C. Franck, "High-speed, full-field deformation measurements near inertial microcavitation bubbles inside viscoelastic hydrogels," Experimental Mechanics **63**, 63–78 (2023).

[36] S. Ravindran, V. Gandhi, A. Joshi, and G. Ravichandran, "Three-dimensional full-field velocity measurements in shock compression experiments using stereo digital image correlation," Review of Scientific Instruments **94**, 10.1063/5.0131590 (2023).

[37] S. Ravindran, V. Gandhi, B. Lawlor, and G. Ravichandran, "Mesoscale shock structure in particulate composites," Journal of the Mechanics and Physics of Solids **174**, 10.1016/j.jmps.2023.105239 (2023).

[38] M. A. Meyers, *Dynamic behavior of materials* (John Wiley & Sons, Ltd, Sept. 1994).

[39] J. Y. Huang, Y. Li, Q. C. Liu, X. M. Zhou, L. W. Liu, C. L. Liu, M. H. Zhu, and S. N. Luo, "Origin of compression-induced failure in brittle solids under shock loading," Physical Review B - Condensed Matter and Materials Physics **92**, 10.1103/PhysRevB.92.144101 (2015).

[40] Correlated Solutions, *VIC-2D (version 6.2) software manual* (2020).

[41] P. Reu, "Virtual strain gage size study," Experimental Techniques **39**, 1–3 (2015).

[42] R. V. Southwell and H. J. Gough, "VI. On the concentration of stress in the neighbourhood of a small spherical flaw; and on the propagation of fatigue fractures in "statistically isotropic" materials," The London, Edinburgh, and Dublin Philosophical Magazine and Journal of Science **1**, 71–97 (1926).

[43] D. Rittel and A. Brill, "Dynamic flow and failure of confined polymethylmethacrylate," Journal of the Mechanics and Physics of Solids **56**, 1401–1416 (2008).

[44] Y. Gupta, "Determination of the impact response of PMMA using combined compression and shear loading," Journal of Applied Physics **51**, 5352–5361 (1980).

[45] The MathWorks Inc., *Matlab version: 9.11.0 (r2021b)*, Natick, Massachusetts, United States, 2021.

[46] E. G. Kirsch, "Die theorie der elastizit t und die bed rfnisse der festigkeitslehre," Zeitshrift des Vereines deutscher Ingenieure **42**, 797–807 (1898).

[47] J. Lambros and A. J. Rosakis, "Shear dominated transonic interfacial crack growth in a bimaterial-I. Experimental observations," Journal of the Mechanics and Physics of Solids **43**, 169–188 (1995).

[48] K. N. Broberg, "The propagation of a brittle fracture," Arkiv fur Fysik **18**, 159 (1960).

[49] L. B. Freund, *Dynamic fracture mechanics* (Cambridge University Press, 1990).

[50] Hibbitt, Karlsson, and Sorenson, *Abaqus/Explicit: User's manual, version 6.2* (Hibbitt, Karlsson and Sorenson Inc., 2001).

[51] G. R. Johnson and W. Cook, "A constitutive model and data for metals subjected to large strains, high strain rates and high temperatures," Proceedings of the 7th International Symposium on Ballistics, 541–547 (1983).

[52] T. J. Holmquist, J. Bradley, A. Dwivedi, and D. Casem, "The response of polymethyl methacrylate (PMMA) subjected to large strains, high strain rates, high pressures, a range in temperatures, and variations in the intermediate principal stress," European Physical Journal: Special Topics **225**, 343–354 (2016).

[53] L. M. Barker and R. E. Hollenbach, "Shock-wave studies of PMMA, fused silica, and sapphire," Journal of Applied Physics **41**, 4208–4226 (1970).

[54] S. P. Marsh, *LASL shock hugoniot data*, Vol. 5 (University of California Press, 1980).

[55] N. S. Brar, V. S. Joshi, and B. W. Harris, "Constitutive model constants for Al7075-T651 and Al7075-T6," in AIP Conference Proceedings, Vol. 1195 (2009), pp. 945–948.

[56] D. J. Steinberg, *Equation of state and strength properties of selected materials* (Lawrence Livermore National Laboratory, Livermore, 1996).

[57] D. Rittel, P. Landau, and A. Venkert, "Dynamic recrystallization as a potential cause for adiabatic shear failure," Physical Review Letters **101**, 10.1103/PhysRevLett.101.165501 (2008).

[58] Y. L. Bai and B. Dodd, *Adiabatic shear localization: Occurrence, theories, and applications* (Pergamon Press, London, 1992).

[59] L. Davison, *Fundamentals of shock wave propagation in solids* (Springer, Berlin Heidelberg, 2008).

[60] G. H. Markstein, "A shock-tube study of flame front-pressure wave interaction," Symposium (International) on Combustion **6**, Sixth Symposium (International) on Combustion, 387–398 (1957).

[61] G. Rudinger, "Shock wave and flame interactions," in Combustion and propulsion, third agard colloquium (Pergamon Press, London, 1958), pp. 153–182.

[62] J. F. Haas and B. Sturtevant, "Interaction of weak shock waves with cylindrical and spherical gas inhomogeneities," Journal of Fluid Mechanics **181**, 41–76 (1987).

[63] V. F. Nesterenko, M. A. Meyers, and T. W. Wright, "Self-organization in the initiation of adiabatic shear bands," Acta Materialia **46**, 327–340 (1998).

[64] Q. Xue, M. A. Meyers, and V. F. Nesterenko, "Self-organization of shear bands in titanium and Ti–6Al–4V alloy," Acta Materialia **50**, 575–596 (2002).

[65] Q. Xue, V. F. Nesterenko, and M. A. Meyers, "Evaluation of the collapsing thick-walled cylinder technique for shear-band spacing," International Journal of Impact Engineering **28**, 257–280 (2003).

[66] F. Zhou, T. W. Wright, and K. T. Ramesh, "The formation of multiple adiabatic shear bands," Journal of the Mechanics and Physics of Solids **54**, 1376–1400 (2006).

[67] D. E. Grady and M. E. Kipp, "The growth of unstable thermoplastic shear with application to steady-wave shock compression in solids," Journal of the Mechanics and Physics of Solids **35**, 95–119 (1987).

[68] M. J. Assael, S. Botsios, K. Gialou, and I. N. Metaxa, "Thermal conductivity of polymethyl methacrylate (PMMA) and borosilicate crown glass BK7," International Journal of Thermophysics **26**, 1595–1605 (2005).

[69] T. W. Wright and H. Ockendon, "A scaling law for the effect of inertia on the formation of adiabatic shear bands," International Journal of Plasticity **12**, 927–934 (1996).

[70] A. Molinari, "Collective behavior and spacing of adiabatic shear bands," Journal of the Mechanics and Physics of Solids **45**, 1551–1575 (1997).

[71] S. Bouissou, J. Petit, and M. Barquins, "Normal load, slip rate and roughness influence on the polymethylmethacrylate dynamics of sliding 1. stable sliding to stick-slip transition," Wear **214**, 156–164 (1998).

[72] G. T. Camacho and M. Ortiz, "Computational modelling of impact damage in brittle materials," International Journal of Solids and Structures **33**, 2899–2938 (1996).

[73] W. Chen and G. Ravichandran, "Failure mode transition in ceramics under dynamic multiaxial compression," International Journal of Fracture **101**, 141–159 (2000).

[74] D. Lacina, C. Neel, and D. Dattelbaum, "Shock response of poly [methyl methacrylate] (PMMA) measured with embedded electromagnetic gauges," Journal of Applied Physics **123**, 10.1063/1.5023230 (2018).

[75] J. L. Jordan, D. Casem, and M. Zellner, "Shock response of polymethylmethacrylate," Journal of Dynamic Behavior of Materials **2**, 372–378 (2016).

Chapter 4

MECHANICS OF COLLAPSE IN PORE ARRAYS AND THEIR INTERACTION IN SHOCK COMPRESSED PMMA

B.P. Lawlor and G. Ravichandran, "Mechanics of collapse in pore arrays and their interaction in shock compressed PMMA," *In Preparation*

Contributions: B.P.L. participated in conception of the project, performed the experiments, conducted the numerical simulations, integrated the theoretical analysis, analyzed the results, and wrote the manuscript.

Abstract

Recent studies on dynamic pore collapse have revealed significant development of shear localization, which can lead to material failure in porous structures and hot spot generation in energetic materials. These findings have dramatically improved the understanding of failure mechanisms during pore collapse, but also prompt further investigation of realistic porous materials. In particular, porous media consist of many pores and porous networks. Even in low-porosity materials, pores can form in close proximity during the manufacturing process, leading to the critical question of pore-pore interaction during collapse under dynamic loading conditions. This study investigates, via plate impact experiments coupled with high-speed internal digital image correlation and shadowgraphy techniques, the collapse of two pores in shock compressed PMMA between 0.4 and 1 GPa. The results of these experiments provide new insights into shear localization in pore collapse, in addition to distinct interactions between pores. Shadowgraphy measurements reveal novel, direct visualization of shear band development and crack evolution from pore surfaces. Spacing between adiabatic shear bands is measured over a range of impact stresses and is predicted accurately by the Grady-Kipp model. Pore interactions are found to effect a transition in the impact stress threshold at which different failure mechanisms initiate, and are also found to possibly in-

fluence preferential sites for shear cracking. Throughout the study, numerical and theoretical models are leveraged to understand shear localization behavior. The role of baroclinicity and wave interactions between the pores are used to elucidate interaction mechanisms between pores.

4.1 Introduction

Porosity is ubiquitous throughout engineering materials, presenting itself via manufacturing defects in both additive manufacturing and traditional material processing techniques such as casting, and is also intentionally incorporated in engineered structures such as foams and lattice structures or in energetic materials. In some settings, porosity has desirable properties such as shock attenuation (energy absorption due to large plastic work required to close pores, which decreases the peak stress experienced behind the porous material) [1–4] and shock disruption (broadening of shock wave structure via micro-inertial effects) [5, 6]. Porous materials also exhibit changes in spall strength compared to their homogeneous counterparts [4, 7, 8], although whether the spall strength improves or degrades depends on the details of the base material properties and initial porosity. Each of these macroscopic properties represent critical aspects of engineering design with porous materials, which has made the study of dynamic compression of porous materials a key research topic. In this work, particular attention is given to studying the closure of arrays of two pores under shock compression—a phenomenon known as pore collapse—and the associated material response in the vicinity of the pores, which is fundamentally intertwined with the macroscopic material response. Of specific interest is the topic of shear localization and failure mechanisms, which could lead to catastrophic macroscopic failure.

Prior to recent investigations on pore collapse, a rich literature in the fluid dynamics community has been developed on the analogous problem of shock bubble interaction, or bubble collapse, [9–12]. These investigations revealed instability generation and complex geometric evolution of the bubble due to vorticity generation and intricate wave interactions at the bubble interface. Baroclinicity has been identified as the driving mechanism for the vorticity generation in this setting, leading to instabilities [13], which provides possible insight to localization phenomenon during pore collapse in solid materials. In addition to bubble collapse, the closely related cavity collapse experiment

was developed in which cylindrical holes (cavities) cut from gelatin (which behaves as a fluid in this setting) are loaded with a stress wave and analyzed during their deformation and collapse [14]. These works serve as an excellent predecessor to the pore collapse studies in solids described below.

In recent years, substantial attention has been given to the pore collapse problem and the possibility of adiabatic shear band nucleation at the surface of collapsing pores, leading to local investigations of pore collapse at the individual pore scale. Adiabatic shear bands (ASBs) are small regions of material in which instabilities nucleate, growing into localized regions of severe shearing. ASBs can simplistically be said to arise due to high shear strain rates leading to large, localized deformation and thermal softening when the rate of deformation and plastic heating exceeds the rate of heat diffusion away from the local region [15–17]. This picture is complicated by competition between strain rate hardening, strain hardening, and thermal softening, in addition to a host of microstructural considerations. That being said, ASBs are an important failure mechanism in dynamic loading situations, yet they pose an enormous challenge for experimental measurement and for accurate prediction via theoretical and numerical modeling. For that reason, it has long been an important area of research, and recent investigations have begun to reveal key details about ASB growth in pore collapse. Experiments using phase contrast imaging (PCI) to study collapsing spherical pores of $3-6\,\mathrm{mm}$ diameter in PMMA have revealed cracking and surface perturbations [18] which may indicate the growth of ASBs from those regions. Later, Lovinger et al., through post-mortem analysis of shock compressed Ti-6Al-4V (Ti64) with $1-2\,\mathrm{mm}$ diameter cylindrical holes, found shear cracks which evidenced shear localization as the primary failure mechanism during their hole closure experiments [19]. Lawlor et al. conducted experiments on $0.8\,\mathrm{mm}$ diameter spherical pores in PMMA while using internal digital image correlation (DIC) with optical imaging, where they obtained *in-situ* evidence of ASB growth and shear cracking [20]. Finally, Lind et al. performed hole closure experiments on Ti64 ($1.2\,\mathrm{mm}$ diameter holes), using PCI to capture the evolution of the hole geometry in conjunction with post-mortem electron back-scatter diffraction (EBSD) analysis, and observed a serrated surface texture, clearly evidencing shear band development which was corroborated through post-mortem analysis [21]. These works have demonstrated the propensity for both PMMA and Ti64 to fail via adiabatic shear banding due to extreme loading imposed during pore collapse

or hole closure, and have also opened the door to investigate many facets of adiabatic shear banding in pore collapse. Some interesting areas of investigation include alternative materials [22, 23], the role of pore size and shape, and interactions among networks of pores.

It is the interaction between pores that is the focus of the present work, with a particular interest in shear localization. Few experimental studies have considered shock loading of pore arrays, despite the reality that porous materials are inherently composed of arrays of pores, and often even networks of connected pores. The aforementioned bubble collapse problem in fluids has been more fully studied with respect to bubble interactions. One such example is Tomita et al. who investigated lines of equally spaced bubbles that are symmetrically and asymmetrically loaded by radial shock waves [24]. They found the early collapse to be similar to the single bubble response, but the late collapse dynamics were dramatically affected by the neighboring pores—resulting in asymmetric collapse geometries because the flow between the bubbles was restrained. The bubble configuration was also found to dictate the direction of jetting. Cavity collapse experiments have also been conducted on arrays of holes. Dear and Field investigated vertical and horizontal lines; rectangular and triangular arrays of pores [14]. Some notable findings arising from bubble interactions include: diverging jet directions, jet velocity enhancement, generation of double jets, and pressure amplification. Most interactions are attributed to wave interactions among bubbles as the planar stress wave generates reflected and refracted waves. Continuing the experiments on arrays of cavities, Swantek and Austin implemented particle image velocimetry (PIV) to enable quantitative analysis of interactions via full field velocity measurements [25]. In all configurations, they found the leading cavity to behave mostly the same as in individual cavity experiments, but neighboring downstream cavities (within approximately one diameter distance) were affected by both collapse-shielding and collapse-triggering interactions. Downstream cavities were also typically found to collapse more slowly than upstream cavities. Finally, moving into the domain of solid materials with strength, Lovinger et al. investigated the interaction of arrays of holes in Ti64 during plate impact experiments along with post-mortem characterization [19]. The post-mortem analysis revealed development of shear cracking and connectivity of cracks with one another and with specimen boundaries, providing distinct evidence of shear localization during pore collapse and of the possibility for crack con-

nectivity to occur. The connectivity of cracks was then linked to possible degradation of spall strength as was measured previously in porous tungsten carbide. Overall, these works demonstrate the complex and impactful role of interactions between bubbles and pores during collapse.

Wave interactions have been shown to be critical mechanisms for creating asymmetric bubble collapse and enhanced localization in the form of jetting, leading one to expect analogous interactions in solid materials and in the shear band localization phenomena which have been observed in single pores. Lovinger et al. have shown the propensity for shear cracks to connect and lead to catastrophic failure in Ti64 [19]. Hence, *in-situ* work investigating the interaction mechanisms via time-resolved measurement of localization and collapse evolution in time is a promising direction which is undertaken here.

To that end, this study presents results from pore collapse experiments on arrays of two pores in PMMA. Following the methodology of Lawlor et al. [20] plate impact experiments, coupled with high-speed imaging, are conducted on PMMA samples with embedded spherical pores. To quantitatively visualize the deformation fields around and between collapsing pores, internal digital image correlation (DIC) [26] is implemented. DIC is a pattern matching technique for which a specimen is painted with a random black and white speckle pattern, images are captured before and during deformation, and pattern matching algorithms determine the displacement field which best maps the deformed speckle pattern to its undeformed state [27]. This displacement field can then be used to compute velocities and strains with which to analyze the deformation during the experiment At higher impact stresses, shadowgraphy [28] is implemented instead, which leverages deflection of light in regions with changing refractive index to create shadows in the image that highlight the second spatial gradient of refractive index. This is particularly useful in this work for identifying the presence of shear bands and cracks, as will be seen throughout the study.

The experimental approach and techniques implemented in the work are described in Section 4.2 along with details of specimen preparation and experimental setup. Results from plate impact pore collapse experiments are then presented in Section 4.3 for both internal DIC and shadowgraph measurements. These results are subsequently complemented by numerical simulations, the approach for which is detailed in Section 4.4, as are the simulated results.

Finally, the observed localization phenomena are analyzed, theoretical and numerical findings are examined to understand the localization, and mechanisms are proposed which may governing their initiation and propagation, elucidating an understanding of wave interactions between neighboring pores.

4.2 Materials and Methods

4.2.1 Experiment Overview

This work investigates the role of interactions between two pores during collapse, with a particular focus on their effect on shear localization, by conducting normal plate impact experiments in conjunction with ultra-high speed imaging. Following the work of Lawlor et al. [20] which explored the collapse of individual pores, this work considers the collapse of two 0.8 mm diameter spherical pores arranged in vertical and horizontal arrays, under shock loading of $0.4 - 0.9$ GPa impact stress. Samples are manufactured from transparent polymethyl methacrylate (PMMA), enabling imaging of internally embedded pores using both the internal digital image correlation (DIC) technique [26] and the more traditional shadowgraphy method [28]. These imaging techniques, respectively, accomplish quantitative deformation measurements and qualitative identification of large deformation features via changes in density gradient.

In this study, a powder gun (38.7 mm bore diameter) facility at Caltech, depicted in Fig. 4.1a, is used to conduct the normal plate impact experiments, which generate controlled planar shock loading (nominally uniaxial strain state) to initiate pore collapse. In short, the experimental technique consists of accelerating a projectile down the gun barrel into the vacuum chamber, where it impacts a target plate and generates a planar shock wave. Traditionally, free surface velocity measurements are taken at the target's rear surface, which are interpreted through one-dimensional shock theory to understand the material response [29, 30]. Instead, here, a high-speed camera is set up, as shown in Fig. 4.1b, to visualize the in-plane deformation inside the transparent sample (in the $X_1 - X_2$ plane) as the shock front propagates along the X_1 direction. In the case of internal DIC, an embedded DIC speckle pattern must be generated at the center-plane in which deformation measurements will be made.

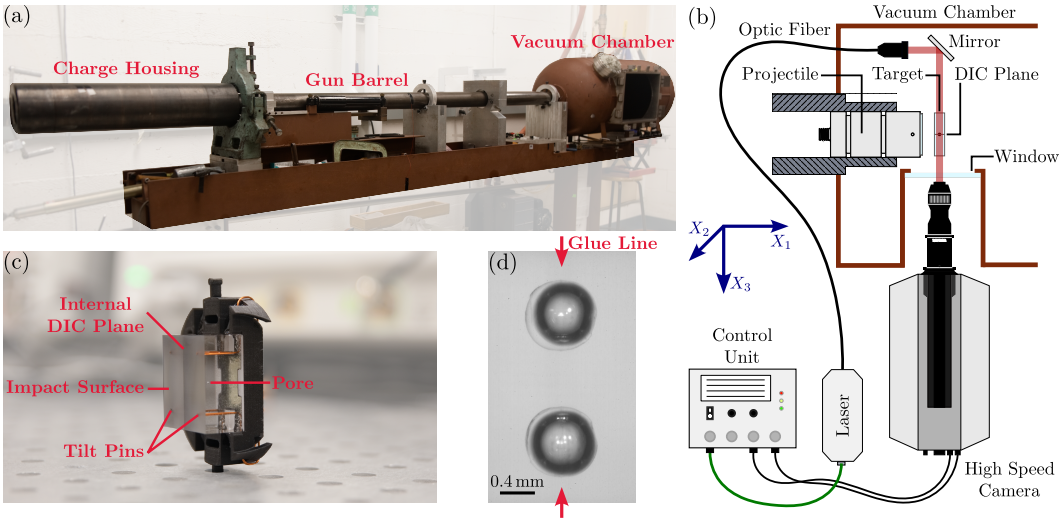

Figure 4.1: Experimental setup with important features labeled. (a) Powder gun facility. (b) Schematic of vacuum chamber and imaging setup for high-magnification, high-speed internal DIC measurements, viewed from top-down. (c) Specimen mounted to the target holder. (d) Microscope image of pore array after gluing, with nearly indiscernible glue line identified.

It is noteworthy that the pore must be embedded internally, and the visualization and corresponding measurements must be conducted internally. This is done to probe the physics of pore collapse under shock compression and free from the effects of surface boundaries and associated reflected waves which disturb the intended loading state. To this end, sample geometries and impact conditions are carefully designed to enable sufficiently large windows of time during which the measurements are taken, before interfering boundary waves arrive. In addition to careful design, the experiments require precise specimen preparation and alignment to ensure planar shock generation. This process is described in the following sections.

4.2.2 Specimen Preparation

Both flyer and target plates are manufactured to satisfy stringent requirements for parallelism (i.e., thickness variation) and surface flatness. Target plate specimens for these experiments are manufactured from as-received PMMA stock obtained from E&T Plastics (Long Island City, New York). The final specimens are cuboid plates with nominal dimensions of $36 \times 36 \times 17$ mm and which have spherical pores (0.8 mm diameter, each, and inter pore spacing of nominally 0.8 mm) embedded at the mid-plane, as shown in Fig. 4.1c. The

specimens begin as two half-specimens ($36 \times 18 \times 17\,\text{mm}$), identical to within machine tolerances, which undergo a preparation process before gluing, as follows. These half-specimens are lapped in pairs on the four largest sides to ensure nearly identical specimen pairs prior to the gluing process. This step aids accurate alignment of half-specimens and creation of a thin, strong glue layer at the interface. Then, the visualization surfaces (all surfaces parallel to the intended glue interface) are mirror polished to enable clear internal visualization. Matching hemispherical voids (0.4 mm radius) are then machined into both half-specimens using a ball-end mill. At this point, the specimens being prepared for internal DIC are speckled by air-brushing a thin layer of transparent paint, depositing toner powder onto the wet paint, and covering the speckle pattern with another thin layer of transparent paint. The paint is allowed to dry for 24 hours prior to gluing. Alternatively, specimens for shadowgraphy are not painted.

After preparing the half-specimens for gluing, they are carefully aligned in a fixture, and the alignment of the hemispherical voids is checked under a microscope. Finally, the two-part epoxy glue, EpoxAcast 690 obtained from SmoothOn (Macungie, Pennsylvania), is applied at the glue interface. Load is then applied to the top half-specimen to squeeze out excess glue, and visual inspection under microscope reveals whether glue seeped into the pore. If glue seeped in, the half-specimens are separated and the gluing process is repeated. Once the specimen is satisfactorily aligned, excess glue removed, and minimal glue seeps into the pore, then weights are added to the specimen to maintain the thin glue layer, and the glue is allowed to set for 48 hours.

After the required 48 hours, the specimen is removed from the gluing fixture, dried glue on the surfaces is carefully removed with a razor blade, and the specimen is lapped on the impact surface and rear free surface. The specimen is lapped to meet specifications of less than $40\,\mu$m thickness variation and less than $2\,\mu$m surface flatness. Finally, shorting pins, used to trigger the experiment, are glued into four holes around the perimeter of the specimen, and are lapped flush with the impact surface. At this point, the specimen preparation is complete. Figure 4.1c provides an example of a completed DIC specimen, with the impact surface, pore, internal DIC plane, and tilt pins labeled. Additionally, the quality of pore alignment after gluing is shown in Fig. 4.1d, where the hemispherical voids and glue line are nearly indiscernible,

instead appearing as two spherical pores.

Flyer plates are machined from as-received aluminum 7075 or PMMA stock, depending on the experiment, into disks of 35 mm diameter and 13 mm thickness. The flyer plates are similarly lapped to achieve less than 15 μm thickness variation and less than 1 μm surface flatness. Flyer plates are then glued into a pocket on the projectile to create the full projectile assembly.

4.2.3 Experimental Setup

After specimen preparation has been completed, the projectile is placed into the gun barrel and the target plate is mounted to a target holder and onto the six-degree-of-freedom gimbal. The gimbal is placed into the vacuum chamber such that the projectile will impact it shortly after exiting the barrel, as depicted in Fig. 4.1b, which shows the complete configuration of specimens and lighting components inside the vacuum chamber.

To ensure planar shock generation, it is imperative that the flyer plate impacts the target plate with minimal angle of misalignment or inclination, which will henceforth be called tilt. To accomplish this, the target plate is carefully aligned to the flyer, first via translational degrees of freedom to center the target on the flyer. Second, mirrors are mounted to both flyer and target, and an auto-collimator is set up to shine a beam of light onto both mirrors and receive the reflected beam, thus determining the misalignment between the plates. This misalignment is then minimized by adjusting the rotational degrees of freedom on the gimbal.

With the specimens prepared and aligned, one can turn to configure the high-speed visualization setup which is composed of the high-speed camera, light source, and zoom lens. Because of the short time scales associated with shock experiments, very high framing rates are necessary. Additionally, to study fine features of pore collapse, high-magnification imaging is implemented. Both high-speed and high-magnification imaging make for an extremely light-starved situation. To remedy this issue, synchronized, pulsed laser illumination is used in a back-lit configuration. This lighting configuration functions both to maximize light for imaging with DIC and to provide nominally collimated light for shadowgraphy in experiments without a speckle pattern. The camera and light source configuration is shown in Fig. 4.1b.

The high-speed camera is mounted on a five-degree of freedom optical stage, enabling precise translational movement to fix the field of view on the pores and to optimize the focus of the images. The camera is additionally aligned to the visualization surface of the target plate using the auto-collimator. This is done to minimize optical effects upon arrival of the shock front. Because the shock front carries a sharp change in refractive index, any misalignment of the camera with the sample leads to an artificial rigid body translation in the image after the shock passes. Hence, this alignment process is undertaken to ensure the field of view which was chosen prior to firing the shot is not lost when the shock front arrives.

4.2.4 High-speed Imaging and Digital Image Correlation

The heart of the high-speed, high-magnification imaging configuration depicted in Fig. 4.1b and detailed in the previous section is the Shimadzu HPV-X2 high-speed camera (Kyoto, Japan) which is utilized to image at 10 million frames per second (100 ns inter-frame time). The high-speed camera is configured with a Navitar $0.7 - 4.5\times$ zoom lens and $2\times$ adapter tube (Rochester, New York). The spatial resolution is 400×250 pixels, which translates to pixel sizes ranging from $7\,\mu$m/pixel to $12\,\mu$m/pixel, depending on the selected lens magnification. Further, it is coupled to the Cavilux Smart pulsed laser illumination source obtained from Cavitar (Tampere, Finland), which is set to pulse for 50 ns during each exposure.

For DIC specimens, the toner powder speckle pattern generates typical speckle sizes of $10 - 20\,\mu$m, which is suitable for the $7\,\mu$m/pixel resolution for the DIC experiments. This speckle size enables correlation using VIC-2D software [31] with parameters of 21 pixel subset size, 1 pixel step size, and 15 pixel strain computation filter size. These correlation settings enable sufficient measurement resolution to capture the filtered trace of shear localization via adiabatic shear bands in PMMA, as was demonstrated previously [20].

Finally, due to optical distortions generated by the zoom lens, a distortion correction procedure is completed before the DIC experiments. After bringing the chamber to vacuum before the shot, a series of static images are taken after moving the camera horizontally and vertically, to simulate rigid body motion of the specimen in the horizontal and vertical directions. These images are then used in the VIC-2D software [31] to determine a correction function

which regains the uniform displacement field in the DIC speckle pattern that is expected from rigid body motion. This correction function is then applied to the images from the experiment to remove lens distortions.

4.3 Results

Five plate impact experiments were conducted to investigate various pore configurations and impact stresses, while maintaining constant pore diameter of 0.8 mm. Table 4.1 summarizes the imaging settings of each experiment, and Table 4.2 details the specimen geometries and loading conditions. Two pore configurations: horizontal (denoted H) and vertical (denoted V), are implemented, with spacing between pores nominally set to 0.8 mm measured from edge to edge. Comparisons are also made with previous work [20] on single pores, which are denoted as S. Shot names are given based on the nominal impact stress (GPa) and pore configuration, vertical (V) and horizontal (H) (e.g., 0.6V). The spacing between pores was selected based on the region of influence observed in the single pore experiments and to work within experimental limits of the camera field of view and spatial resolution. Additionally, impact stresses varying from $0.4-0.9$ GPa are considered based on previously observed localization and failure phenomenon occurring in this stress regime [20].

Impact stress is predicted during experiment design by combining the flyer and target plate equations of state (empirical $U_s - u_p$ relations, where u_p is the particle velocity and U_s is the corresponding shock wave speed), as well as the impact velocity. These are analyzed through a process known as impedance matching [30] to predict the particle velocity in the target material. Then, the predicted impact stress is calculated based on the target plate properties as

$$\sigma_{11} = \rho_0 U_s u_p \tag{4.1}$$

where ρ_0 is the unshocked density. Similarly, after measuring impact velocity in experiment, the actual impact stress can be calculated and is reported in Table 4.2 for all experiments.

4.3.1 Internal Digital Image Correlation (DIC)

For experiments 0.4V, 0.6V, and 0.6H, in which internal DIC was conducted, the raw images are analyzed in VIC-2D software [31] to correlate the speckle

Table 4.1: Summary of experimental imaging specifications. Shot number indicates the nominal impact stress (GPa) and the configuration of pores—vertical (V) or horizontal (H).

Shot	Imaging Technique	Spatial Resolution (μm/pix)
0.4V	DIC	7
0.6V	DIC	7
0.6H	DIC	7
0.8V	Shadowgraphy	11
0.9V	Shadowgraphy	12

Table 4.2: Summary of pore collapse experiments: specimen geometries, materials, and loading conditions. Shot number indicates the nominal impact stress (GPa) and the configuration of pores—vertical (V) or horizontal (H).

Shot Number	Flyer Material	Flyer Thickness [mm]	Target* Thickness [mm]	L_{Space}** [mm]	L_{Pore}*** [mm]	Impact Velocity V_i [m/s]	Shock Stress σ_{11} [GPa]	Tilt [mrad]
0.4V	PMMA	12.981 ± 0.004	16.315 ± 0.020	0.78	4.4	227 ± 2	0.41 ± 0.01	N/A
0.6V	Al 7075	12.881 ± 0.002	15.965 ± 0.009	0.77	4.7	226 ± 4	0.66 ± 0.01	1.26
0.6H	Al 7075	12.893 ± 0.007	16.142 ± 0.007	0.60	5.0	217 ± 5	0.64 ± 0.02	3.2
0.8V	Al 7075	12.848 ± 0.001	16.457 ± 0.011	0.70	4.8	260 ± 3	0.78 ± 0.01	2.5
0.9V	Al 7075	12.964 ± 0.005	16.199 ± 0.003	0.61	5.2	293 ± 3	0.89 ± 0.01	0.25

*All target plates were manufactured from PMMA.
**L_{Space} indicates the edge-to-edge spacing between pores.
***L_{Pore} indicates the distance from impact surface to the front edge of the pores. For 0.6H, the distance is measured to the leading (upstream) pore.

pattern evolution to extract quantitative displacement field measurements. From the displacement fields, Lagrangian strain is computed via discrete differentiation. Further, because the interest of these experiments lies in the identification of localization features, such as shear bands, an effective shear strain metric is most instructive. For that reason, the DIC data is presented in terms of Tresca shear strain, defined as

$$\gamma_{\text{Tresca}} = \frac{\varepsilon_{\text{I}} - \varepsilon_{\text{III}}}{2} \tag{4.2}$$

where ε_{I} and ε_{III} denote the maximum and minimum principal strains.

The DIC results for these three experiments are summarized in Fig. 4.2, which presents a series of representative time instances during each experiment. The images are displayed with Tresca shear strain fields overlaid wherever applicable (i.e., behind the shock front). Upon inspection of the images, one notes the presence of a dark, blurry band moving across the image from left to right. This feature is the shock front, inside of which the steep gradient in density and refractive index casts a shadow and generates blurriness/opacity, but the

material regains its clarity/transparency behind the shock front. The material also begins to deform and develop distinct strain contours after the shock front passes.

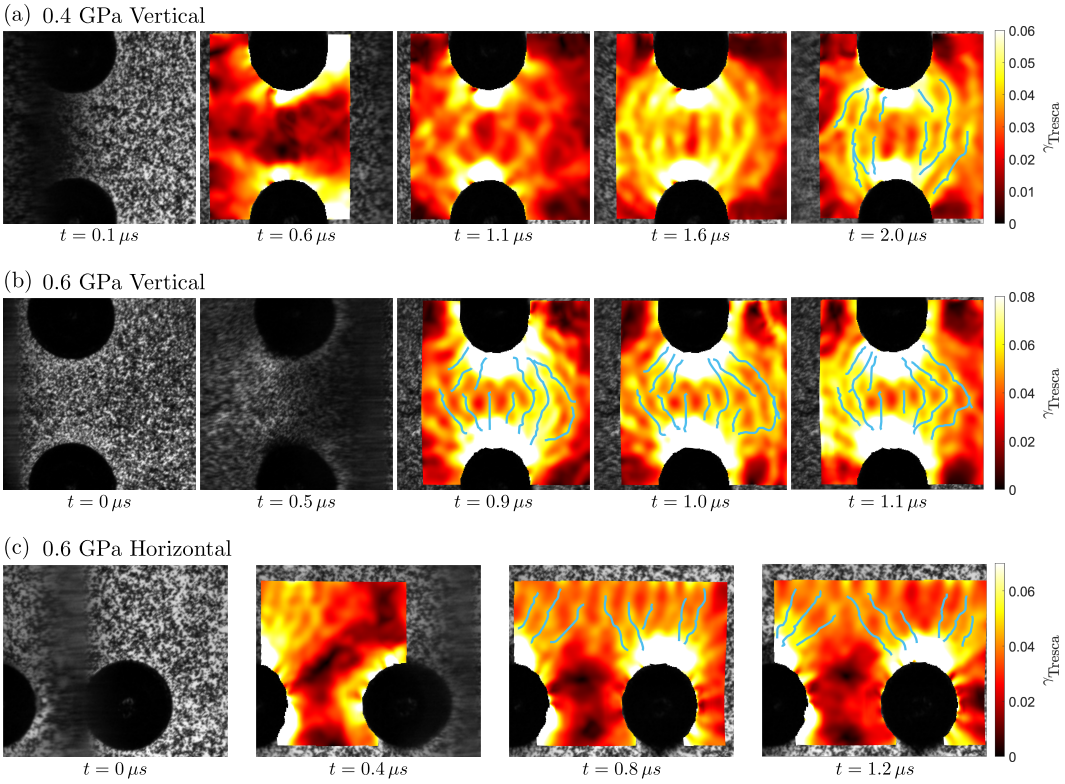

Figure 4.2: Time series of experimental images with DIC measurements of Tresca strain overlaid, along with tracked shear bands (blue), at selected time instances.

In experiment 0.4V, displayed in Fig. 4.2a, a strain field develops which is initially characteristic of classical strain concentrations around a compressed pore, at $t = 0.6\,\mu$s, for instance. The shear strain is directly concentrated in the top and bottom of the pores, and becomes small in the region between the pores. This result is very similar to that of a single pore under 0.4 GPa impact stress (experiment 0.4S), as was shown previously [20]. However, at late time instances a structure of bands begins to develop (e.g., $t = 1.6\,\mu$s). This structure, identified as an array of shear bands emanating from the pore surface, is very similar to what was seen previously at 0.6 GPa for a single pore (0.6S). However, these bands were not observed in 0.4S, indicating that the presence of neighboring pores is inducing a shift in the impact stresses at which these bands develop.

After it develops, the mature shear band structure is tracked from frame to frame by manually inputting initial guesses for shear band locations, then identifying all local maxima in shear strain, and finally trimming down the local maxima based on the initial guesses. This process is further described in Appendix 4.A. The results from the shear band tracking process are overlaid on the DIC shear strain fields, such as in Fig. 4.2a at $t = 2.0\,\mu$s. When mapped back to the reference configuration, the tracked shear bands indicate consistent material location, emphasizing their nature as material deformations, rather than optical artifacts.

As expected, based on previous results from single pore experiments at 0.6 GPa, the results from experiments 0.6V and 0.6H in Fig. 4.2b-c reveal a banded structure similar to that of 0.4V. However, in this case the bands develop rapidly after the shock front passes the pore and DIC correlation is achieved. Of particular note in the vertical configurations is the apparent connection of shear bands, either coalescing with or intersecting one another.

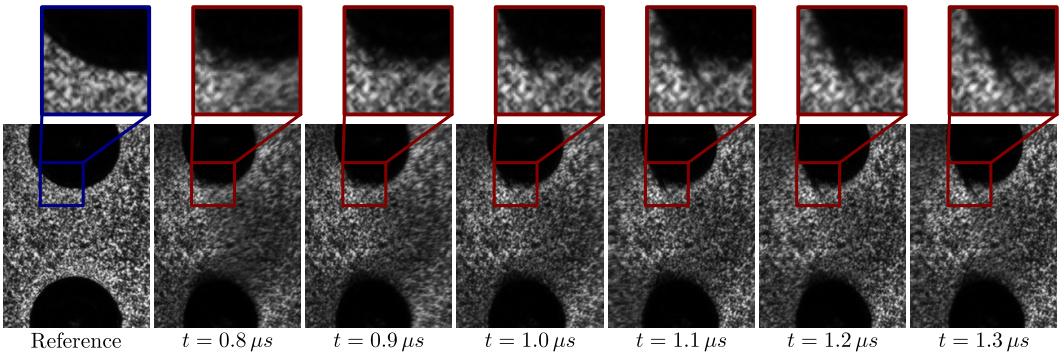

Figure 4.3: Time series of raw experimental images for experiment 0.6V. Insets provide a magnified view of the region of interest, where the crack grows from the top pore. Crack initiation is observed beginning at $t = 1.0\,\mu$s and branching starts at $t = 1.2\,\mu$s.

While shear banding was expected to occur in both experiments 0.6V and 0.6H, a different shift in failure mode was observed at 0.6 GPa. Experiments on a single pore at 0.8 GPa (0.8S) had previously revealed a transition to failure via a strong shear band which gave way to shear cracking due to material weakening in the shear band [20]. Similarly here, cracks begin developing at the surfaces of the pores in experiment 0.6V. Figure 4.3 highlights the prominent cracking at the surface of the top pore, though a more subtle crack also appears to propagate from the surface of the bottom pore. While in experiment 0.8S, the cracking occurred nearly immediately after the shock

front passed the pore ($t = 0.5\,\mu$s), in 0.6V there is a substantial delay until $t = 1.0\,\mu$s at which point a crack grows from the top pore to a length of approximately 0.38 mm by $t = 1.3\,\mu$s There is also evidence that such cracking initiates in 0.6H, but it is less apparent.

These shifts in failure mode thresholds are of great interest to understanding the localization phenomenon during pore collapse in materials with networks of pores that interact with one another. The time delay observed in this case suggests the involvement of some transient mechanisms such as wave reflections. This topic will be discussed in greater detail in Section 4.5.4.

4.3.2 Shadowgraphy

Beyond 0.6 GPa impact stress, substantial cracking has been observed which prevents accurate use of DIC for strain measurement (e.g., experiment 0.8S) [20]. Additionally, large out of plane deformations in the target plate, as well as changes in refractive index in the target plate, lead to defocusing while under very high magnification. For these reasons, the experiments above 0.6 GPa (i.e., 0.8V and 0.9V) are conducted using shadowgraphy, rather than DIC, and with lower magnification to preserve optical focus and visualize the entirety of both pores and the surrounding material. While this technique does not provide quantitative strain measurements, it is sensitive to the second spatial gradient of refractive index [28], making it an excellent tool to qualitatively identify the location of shear bands and cracks. Throughout this study, shear band and crack lengths are tracked quantitatively, but because of the lowered spatial resolution and imperfectly collimated light, the data reported are considered to be estimates, rather than concrete measurements. Even so, these estimates provide useful insights into the shear banding and cracking phenomenon which occur during pore collapse and have not been previously observed.

The results from experiments 0.8V and 0.9V are presented in Figs. 4.4 and 4.5. Selected time instances are presented from the experimental high-speed images, and important features throughout the experiments are identified with labels.

Examining first the experiment 0.8V, one observes the planar shock front, marked by the letter A, propagating from left to right, for $t = 0.2 - 0.4\,\mu$s before leaving the camera's field of view. Upon its arrival at the leftmost (up-

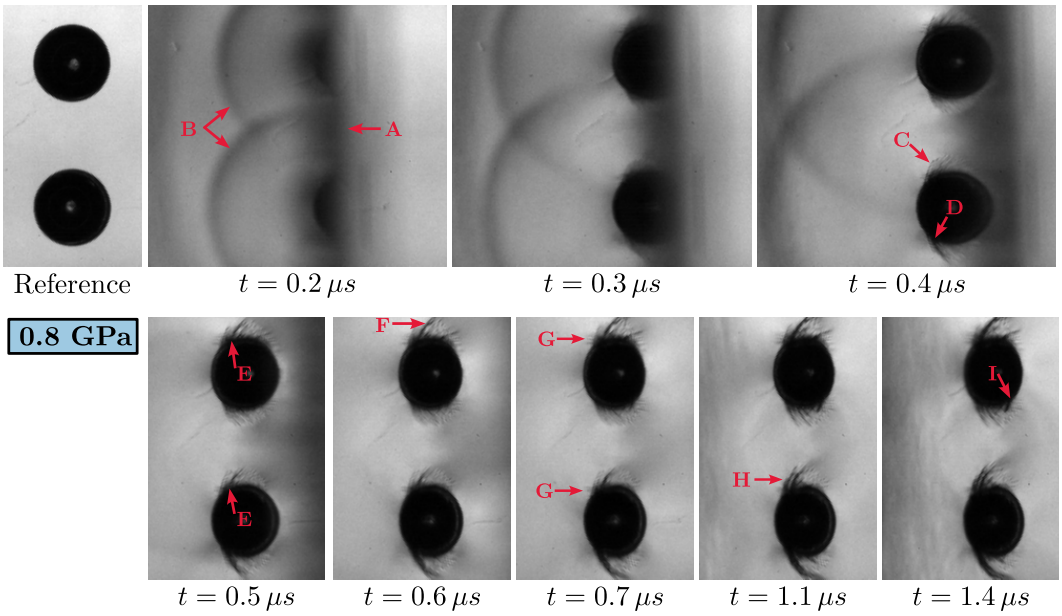

Figure 4.4: Time series of experimental shadowgraphy images for experiment 0.8V. Distinct features observed are labeled as follows. A: Shock front. B: Diffracted longitudinal waves. C: Example of first shear band initiation (observed at top and bottom of both pores). D: First crack propagation. E: Examples of abrupt crack growth. F: Crack branching. G: Backward propagating shear bands. H: Example of late-stage crack growth. I: Backward propagating crack. Note, time is shifted such that $t = 0$ corresponds with shock front arrival at the upstream pore surface.

stream) pore surface, the planar shock front generates diffracted, or reflected waves, (denoted by the letter B) which propagate radially from the pore surface. These longitudinal (pressure) diffracted waves originate from the pore surface in order to maintain a traction-free surface at the PMMA-air boundary. Alternatively, this can be thought of as a reflection due to impedance mismatch between PMMA and air. The diffracted waves intersect and amplify one another at the intersection point, resulting in an enhanced darkening. These longitudinal diffraction waves are visible in shadowgraphy because of the steep density (refractive index) change, but the shear diffraction waves which follow behind are invisible in this technique. Shear diffraction waves are revealed through numerical simulations and discussed more fully in Sections 4.4 and 4.5.4.

After the planar shock fully passes the pore, transparency is regained, starting at $t = 0.4\,\mu$s and completely restored by $t = 0.5\,\mu$s. Immediately after transparency is regained, a rich structure of shear bands (C indicates an example

region) is revealed—visible as partially-darkened bands—emanating from the top and bottom of the pores. To the authors' knowledge, this is the first direct, *in-situ* visualization of shear band development during pore collapse, and possesses remarkable qualitative consistency with the structures previously predicted via numerical simulations [20]. At the same time, a shear crack (D) begins to propagate, presumably along a shear band through the weakened material, as was suggested by Lawlor et al. [20]. From $t = 0.5 - 0.6\,\mu$s, several cracks begin to propagate and grow abruptly (E), and also exhibit branching (F), both of which provide clear distinction between the behavior of shear bands and cracks. In addition to the crack-like behaviors of abrupt growth and branching, the thickness and darkness of the shadow cast by the features are heuristically used to distinguish between cracks and shear bands.

In the initial field of shear bands, one can observe several instances of backward-propagating shear bands which will be examined using numerical results to be presented in Section 4.4. While the shock direction imposes a strongly preferential direction for shear banding and cracking, it does not prevent the occasional instances of backward band propagation (G) or backward crack propagation (I). Finally, one sees at late time instances, such as $t = 1.1\,\mu$s, that late stage crack propagation occurs, well after the passing of the shock front, indicating the transient nature of these failure modes and the possible role of diffracted waves in initiating such failure.

Turning one's attention to experiment 0.9V shown in Fig. 4.5, many of the same features develop as in experiment 0.8V. The planar shock propagates past the pore (A) and diffracted longitudinal waves propagate (B). Shear bands develop immediately after the passing of the planar shock front, once again (e.g., C), but now with greater density of bands relative to the pore surface length on which they initiate (particularly notable at $t = 0.5 - 0.8\,\mu$s, with an example indicated as H). More severe, early, abrupt crack propagation occurs (e.g., D), along with several sets of backward-propagating shear bands (E). Additionally, crack branching occurs once again at $t = 0.5\,\mu$s (F) along with late crack growth around $t = 1.1\,\mu$s (I). Distinct from experiment 0.8V, however, is the emergence of secondary, weaker (lighter) bands emanating, first, from the left side of the pore (G), and later, from the right side of the pore (J). This weaker, more spread out, band structure appears to indicate a secondary set of shear bands and possesses contours very similar to those

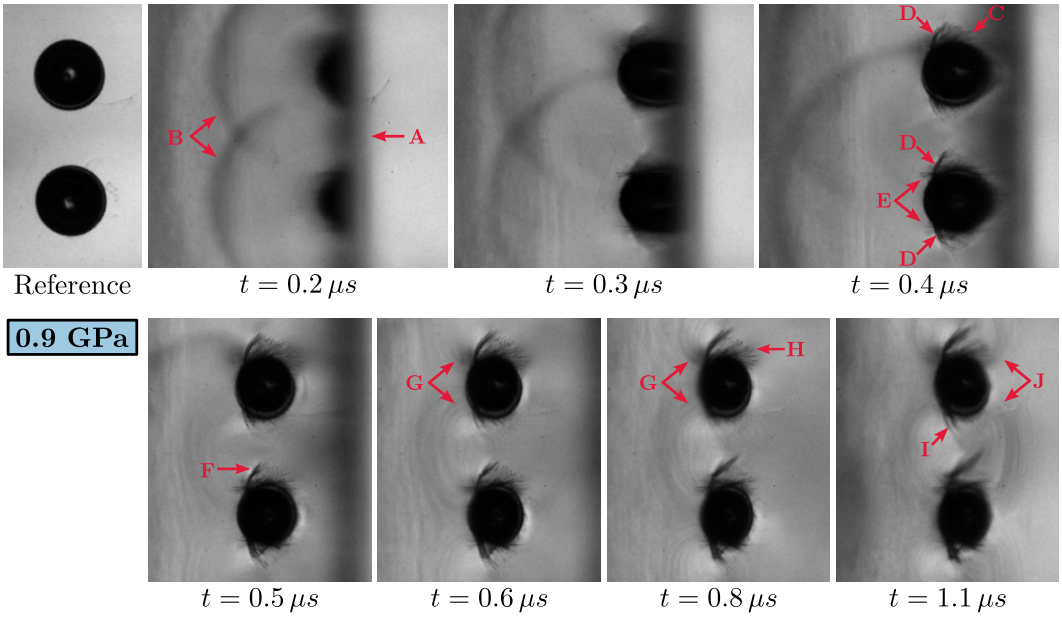

Figure 4.5: Time series of experimental shadowgraphy images for experiment 0.9V. Distinct features observed are labeled as follows. A: Shock front. B: Diffracted longitudinal waves. C: Example of first shear band initiation (observed at top and bottom of both pores). D: Rapid, large crack propagation. E: Backward propagating shear bands. F: Crack branching. G: Secondary (weak) band pattern emanating from left side of pores. H: Examples of dense field of mature shear bands. I: Late-stage crack growth. J: Secondary band pattern now emanating from right side of pore. Note, time is shifted such that $t = 0$ corresponds with shock front arrival at upstream pore surface.

observed via DIC in experiments 0.4V, 0.6V, and 0.6H. These bands likely exist in 0.8V as well, but, while DIC is sensitive enough to pick them up at lower stresses, it appears that only at 0.9 GPa impact stress do they become severe enough that they can be identified via shadowgraphy.

In summary, the experiments presented here have unveiled several important deformation and failure phenomena associated with the pore collapse event and interactions between multiple pores. In particular, an apparent shift occurs in the impact stress threshold required to initiate localization and failure, due to pore interactions. Further, the implementation of shadowgraphy in pore collapse has revealed rich fields of shear bands and enabled characterization of their evolution in time and transition into shear cracking. Additionally, a distinction has been made between primary, strong shear bands and secondary, weak shear bands, which ties together the DIC and shadowgraphy measurements across the impact stress range. These findings will be further explored

in Sections 4.4 and 4.5, and their driving mechanisms will be investigated.

4.4 Numerical Modeling

4.4.1 Model details

Numerical modeling is undertaken in an effort to supplement experimental findings and understand the physics and mechanisms which govern the material and structural responses observed. Specifically, thermo-viscoplastic finite element analysis is conducted in Abaqus/Explicit [32] under adiabatic conditions. To accomplish this, the Johnson-Cook plasticity model [33] is implemented to incorporate strain rate hardening, strain hardening, and thermal softening, which is described by Eq. (4.3) where Y is the Mises flow strength as a function of equivalent plastic strain, equivalent plastic strain rate, and temperature.

$$Y = \left[A + B\left(\bar{\varepsilon}^{pl}\right)^{n}\right]\left[1 + C\ln\frac{\dot{\bar{\varepsilon}}^{pl}}{\dot{\varepsilon}_{ref}}\right]\left[1 - \left(\frac{T - T_r}{T_m - T_r}\right)^{m}\right] \tag{4.3}$$

The model parameters for PMMA were calibrated previously by Lawlor et al. [20] using a collection of data presented by Holmquist et al. [34]. The considerable thermal softening which is inherent in PMMA proves to be the mechanism responsible for adiabatic shear banding to occur, as was previously shown [20]. Parameters for aluminum 7075 were taken from Brar et al. [35]. These material parameters are reported in Table 4.3, where B and n govern strain hardening, C governs strain rate hardening, and m dictates thermal softening. Additional parameters T_r and T_m, the reference and melting temperature, are set to room temperature and the glass transition temperature, respectively. Finally, an equation of state (EOS) must be prescribed to accurately capture shock wave propagation, the details of which are reported in Table 4.4, where parameters C_0 and S inform the $U_s - u_p$ relationship,

$$U_s = C_0 + Su_p \tag{4.4}$$

and Γ_0, the Grüneisen parameter, completes the EOS description. Because of the unusual nonlinear $U_s - u_p$ response for PMMA at low pressures [36–38], two piecewise-continuous linear EOS models are used, denoted EOS 1 and EOS 2.

To capture any possible effects of pore interactions in the experiments, three-dimensional finite element analysis is conducted. The model is meshed with

quadratic tetrahedral elements (C3D10M) to conform to the complex geometry of the pore surface. Additionally, to capture the fine localization features of experiments, such as adiabatic shear bands, mesh refinement near the pore is necessary. In the vicinity of the pores (within 600 μm of the pore surfaces), 15 μm elements are incorporated, while the mesh far from the pores uses 40 μm elements. This choice of element size introduces an inherent shear band length scale of approximately 30 μm thickness, consistent with previous experimental observations of shear band thicknesses in PMMA [39].

To accommodate such a fine mesh, the model is significantly reduced to lower the computational cost. Specifically, the flyer thickness is reduced to 4 mm and the target thickness to 5 mm, which is sufficient to prevent wave reflections from affecting results. The width of the model is also reduced, such that the rectangular part extends only 300 μm beyond the refined mesh region. Finally, the model is halved, making use of the symmetry across the plane which sections both pores. The number of elements in the simulation are approximately 8.5×10^6 and the number of degrees of freedom are approximately 60×10^6. To maintain lateral confinement with these width reductions, displacement boundary conditions are imposed at the center plane and outer boundaries. The nodes at the impact surface between the flyer and target are also tied to ensure a perfect contact.

Table 4.3: Parameters for the Johnson-Cook plasticity model.

Material	Model parameters (Eq. (4.3))							
	A [MPa]	B [MPa]	n	C	m	$\dot{\varepsilon}_{ref}$ [1/s]	T_m [K]	T_r [K]
PMMA [34]	210	160	2.95	0.077	0.74	1	398	298
Aluminum 7075 [35]	546	678	0.71	0.024	1.56	1	903	298

Table 4.4: Material properties and equation of state parameters.

Material	Density ρ_0 [kg/m^3]	Specific Heat c [J/(kg·K)]	Shear Modulus G [GPa]	C_0 [m/s]	S	Γ_0
PMMA (EOS 1) [34, 36, 40–42]	1186	1466	2.19	2770	2.11	0.85
PMMA (EOS 2) [34, 36, 40–42]	1186	1466	2.19	3044	0.36	0.85
Aluminum 7075 [41, 42]	2804	N/A	26.9	5022	1.99	1.97

4.4.2 Modeling Results

A series of four simulations are conducted to replicate the experimental conditions of experiments 0.4V, 0.6V, 0.8V, and 0.9V, with an aim to understand the transient dynamic mechanics which cause different localization responses in vertically configured pores, compared to single pores. The results for the equivalent plastic strain ($\bar{\varepsilon}^{pl}$) from these simulations are presented in Fig. 4.6, with selected time instances reported for each simulation, along with representative experimental results reproduced for comparison.

The model appears to accurately capture the presence or absence of strong shear bands, such as those seen in 0.8V and 0.9V, and also those in 0.6V which give rise to shear cracking. The 0.4 GPa simulation, conversely, does not show any strong shear bands, which is consistent with the lack of shear cracking in 0.4V. Along these same lines, the simulations do capture many of the same shear band modes which are observed in experiments. The dominant shear bands and shear cracks, which develop at the top left and bottom left regions of the pore, are accurately reproduced, especially in the 0.6 GPa and 0.8 GPa simulations. By 0.9 GPa, the simulations begin to favor strong shear banding farther to the right of the pore, which is seen in experiments 0.8V and 0.9V; however, this is not the dominant mode of localization in those experiments. Another feature which is well-captured are the backward-propagating shear bands at the left side and top/bottom right regions of the pores. However, the numerical results do not capture the secondary shear bands observed via shadowgraphy in 0.9V and via DIC in 0.4V and 0.6V. This is indicative of a subtle material instability present in PMMA and/or a perturbing load arising from wave interactions, which the numerical model is unable to capture.

Further, experiments 0.8V and 0.9V appear to indicate that shear localization severity, timing, and modality is somewhat stochastic, but may be influenced by the pore surface orientation being inward (facing the neighboring pore) or outward, and localization is enhanced by neighboring pores in the vertical configuration. Unlike experiments, simulations on single or double pores do not reveal substantial differences from one another. While the results are consistent with the partially stochastic behavior observed with respect to shear band modality and timing, it also suggests that the effects of pore interaction on localization are governed by subtleties not entirely captured in simulation. This experimental feature will be explored in more depth in Section 4.5, but it

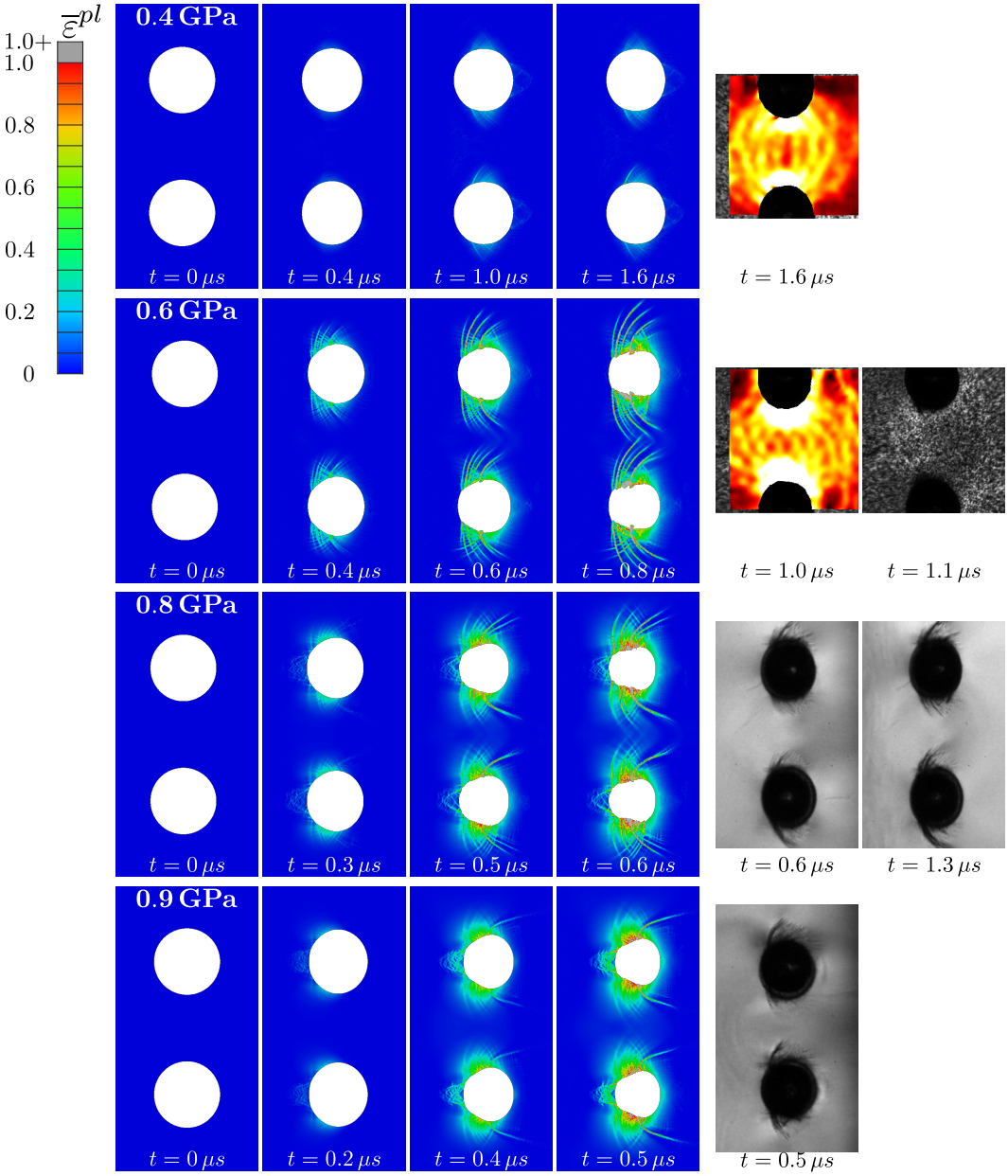

Figure 4.6: Summary of 3D numerical simulations. Results (at the center-plane) for equivalent plastic strain ($\overline{\varepsilon}^{pl}$) from simulations matching experimental impact stresses are presented for 0.4V, 0.6V, 0.8V, and 0.9V on the left. Experimental comparisons at selected time instances are shown on the right.

warrants mention here that the numerical simulations do not entirely capture this feature. Finally, the simulated results predict substantial material collapse, from the top and bottom pore surfaces, into the pore itself, as a result of large shear deformations due to shear bands. While this is experimentally observed to some extent, especially for the most dominant cracks, the overall pore geometry evolution in time for simulations does not correspond with the experiments. This difference may be related to the absence of frictional effects or other stabilizing forces in the simulations. Rather than modeling the shear band transition into shear fracture, and the corresponding frictional resistance to sliding, the shear bands are able to entirely weaken and slide with minimal resisting forces. This feature would be worth further investigation in future computational studies of pore collapse. It is worth noting that the numerical simulations presented here demonstrate the ability to capture the most dominant localization features present in experiments with reasonable qualitative accuracy, offering promise for predictive capabilities while also drawing attention to areas for future improvement, such as capturing the more subtle material instabilities and pore shape evolution. This numerical framework will be further leveraged throughout Section 4.5 to unravel the pertinent physics involved in pore interactions.

4.5 Discussion

Having considered the findings of these pore collapse experiments with multiple pores, along with numerical simulations to model the experiments and extract additional understanding of physics at play, one now turns to consider several pertinent issues. Those include the topics of shear band spacing and its evolution with varied impact stresses; crack propagation and the roles of impact stress, timing, location on the pore surface, and interactions between pores; driving mechanisms for crack initiation; and the mechanisms for pore interactions.

4.5.1 Shear band spacing

Shear band spacing is a topic which has garnered great interest from both experimental, especially using the thick walled collapsing cylinder experiment [43–45], and theoretical studies, including two which are considered here [46, 47] that have been summarized by Nesterenko et al. [43]. Previous work

by Lawlor et al. [20] provided the first comparison of these models with the experimental results from shock-induced collapse of a single pore at 0.6 GPa impact stress, based on measurements of developed shear bands which were captured via DIC. The results in the current work have provided access to shear band spacing data across various impact stresses, and from different measurement techniques—DIC and shadowgraphy—which can be compared to the relevant theories. Average shear band spacing is computed by manually counting the number of bands in each region that exhibits shear bands (e.g., experiment 0.8V has four regions: the top and bottom of both pores) and measuring the pore surface length along-which the shear bands develop. These results, compared to the theories which are described below, are presented in Fig. 4.7.

The Grady-Kipp (GK) model [46] captures the natural length scale between shear bands through a momentum diffusion model. This approach considers the process by which large deformations and material weakening in an ASB cause unloading of the material in its vicinity. This unloading process is determined to have a length scale based on the speed of the unloading front,

$$L_{\mathrm{GK}} = 2\left(\frac{9kc}{\dot{\gamma}^3 a^2 \tau_0}\right)^{1/4} \tag{4.5}$$

where L_{GK} represents the predicted spacing between ASBs; k and c are the thermal conductivity and specific heat capacity, respectively. A linear thermal softening material model described by

$$\tau = \tau_0[1 - a(T - T_0)] \tag{4.6}$$

is used, which relates the flow stress, defined as $\tau = \sigma/2$ where σ is the yield stress under uniaxial loading, to the flow stress at room temperature, τ_0 and a linear softening parameter, a. Here, the same model parameters are used as in Lawlor et al. [20], which fit PMMA material parameters to data from Holmquist et al. [34] for the linear thermal softening model. The parameters are reproduced in Table 4.5.

Finally, the model assumes a representative applied shear strain rate, $\dot{\gamma}$. This strain rate is determined by conducting numerical simulations that reproduce the experimental loading conditions, while preventing development of shear bands. To this end, the same approach is used as in Section 4.4, but artificially increases the PMMA melting temperature, T_m, to 1000 K to prevent any

Table 4.5: Parameters for Grady-Kipp adiabatic shear band spacing model.

Material	k [W/(m·K)]	c [J/(kg·K)]	$\dot{\gamma}$ [s^{-1}]	τ_0 [MPa]	T_0 [K]	a [K^{-1}]	m
PMMA [34, 40, 48]	0.19	1466	0.45×10^6	53	298	0.0061	0.077

appreciable thermal softening in the simulation. Then, the peak strain rate in the concentrated region at the top and bottom of the pore (where experimental observations show shear band initiation) is computed and input to the GK model.

Alternatively, Wright and Ockendon (WO) took a perturbation theory approach to the problem, identifying the wavelength which generates the maximum growth of perturbations. They assume linear thermal softening in addition to strain rate hardening (parameter m),

$$\tau = \tau_0[1 - a(T - T_0)] \left(\frac{\dot{\gamma}}{\dot{\gamma}_0}\right)^m \tag{4.7}$$

where $\dot{\gamma}_0$ is the reference strain rate (set to $1\,s^{-1}$) and $\dot{\gamma}$ is the imposed strain rate. Following their perturbation analysis, they find the minimum spacing to be

$$L_{WO} = 2\pi \left(\frac{kcm^3\dot{\gamma}_0^m}{\dot{\gamma}^{3+m}a^2\tau_0}\right)^{1/4}. \tag{4.8}$$

These two models, taking entirely different approaches, have been found to accurately describe different stages of adiabatic shear band growth [29], WO capturing the spacing between even the smallest shear bands which nucleate but may die out in the presence of competing neighboring shear bands, and GK capturing the spacing between more mature shear bands which have grown past the initial nucleation phase. This difference was found to be true in the single pore experiments [20] which, comparing DIC measurements to GK model, found good agreement. Once again, in this study, the measurements lack the resolution to capture the fine details of shear band nucleation near the pore surface. Hence, it is difficult to compare accurately with the WO model, and the WO model predicts smaller spacing than are found in the experiments. In contrast, in the comparison to the GK model, one finds an excellent match with experimental results. This confirms that the measured shear bands in these experiments are an indicator of mature, developed shear bands, while smaller shear bands likely initiated at the pore surface but died out in the presence of competing shear bands.

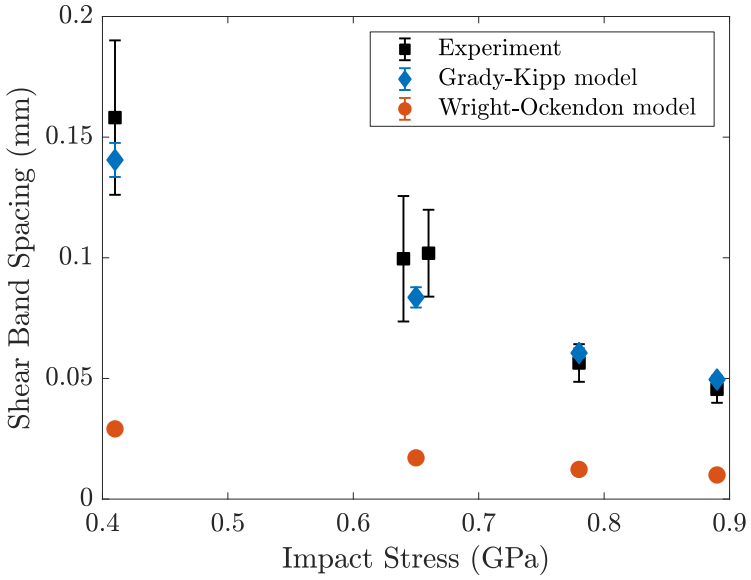

Figure 4.7: Average shear band spacing for each experiment, compared to classical models for prediction of spacing (Grady-Kipp [46] and Wright-Ockendon [47]).

Overall, the experimentally observed trend coincides with the theoretical prediction that shear bands will become more densely packed as the strain rate (correlated with the impact stress) increases. Simultaneously, it appears that, in addition to becoming more closely packed, shear bands may become finer as strain rate increases. Beyond these observations and consistent trends, the GK model proves to be a predictive tool for shear band spacing in the pore collapse problem and at this length scale. It would be worthwhile to investigate its applicability at higher stresses and in alternative materials and pore geometries.

4.5.2 Crack propagation

Focusing now on the shadowgraphy results from experiments 0.8V and 0.9V, one can begin to track major features more quantitatively. In both experiments, the most dominant shear bands and cracks are manually tracked from frame to frame, enabling the extraction of various features such as initiation position and length evolution with time. Unfortunately, many shear bands develop which are partially obscured by neighboring shear bands, not severe enough to be distinctly identified with shadowgraphy, or simply too small relative to the spatial resolution of the camera. Although they were identified for shear band spacing measurements, those bands are ignored in this analysis.

Instead, the most dominant features are identified with the aid of the MATLAB image processing toolbox [49], manually tracked, and displayed overlaid on the experimental images in Fig. 4.8a and Fig. 4.9a. The features are then classified as cracks or shear bands based on the darkness and thickness of the features (darker and thicker features are more likely to be cracks) and characteristic behaviors of cracks such as abrupt, rapid growth and branching. These classifications are not made with complete certainty, but are helpful for categorizing the data and understanding the overall trends in their initiation and growth. Next, their lengths are plotted as a function of time in Fig. 4.8b,c and Fig. 4.9b for more quantitative analysis.

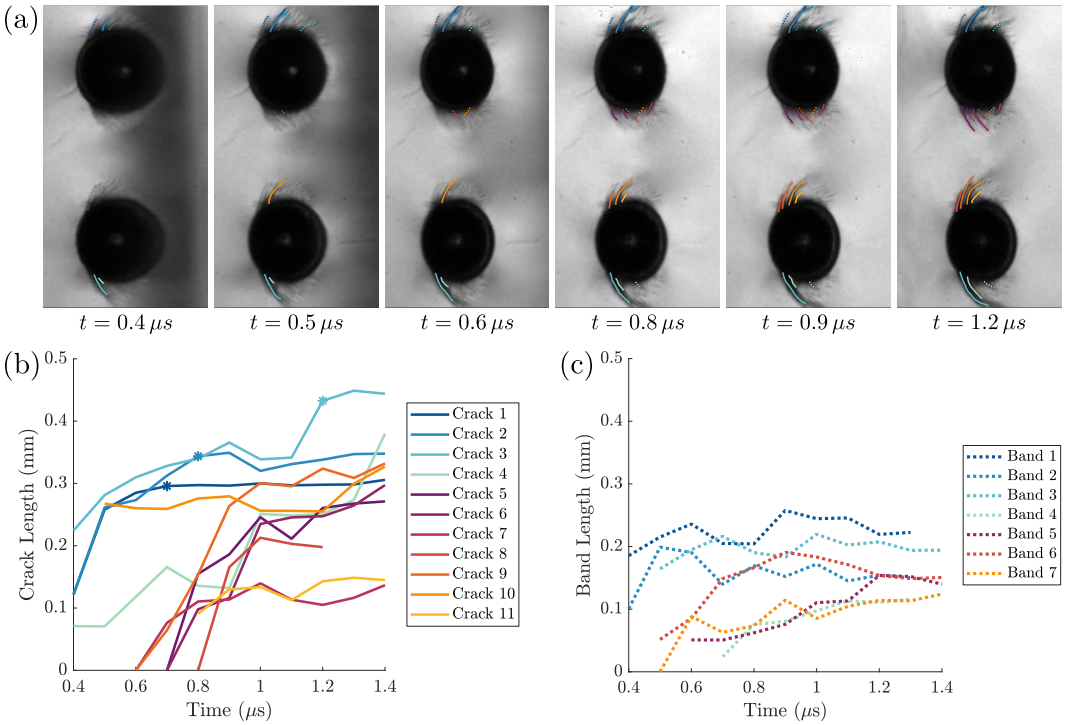

Figure 4.8: Experiment 0.8V crack and shear band profile evolution with time. (a) Cracks are tracked and plotted over deformation images at several representative time instances. (b) Crack length estimates from tracking are displayed as a function of time. (c) Shear band length estimates as a function of time. The asterisk symbol on curves indicates that the crack tip exited the camera's field of view at this time. Measurements of those cracks at later time instances only capture the length within the field of view, hence their apparent plateau. This applies for cracks 1, 2, and 3.

First considering experiment 0.8V, one observes a strong preference for cracks to grow on the outer pore surfaces (i.e., top surface of the top pore and bottom surface of the bottom pore) first, and then for cracks to grow later on the inner

surfaces (i.e., bottom surface of the top pore and top surface of the bottom pore). This is particularly notable in Fig. 4.8b which shows cracks 1, 2, 3, and 10 growing early on—only one of which is an inner crack. However, around $t = 0.6 - 0.8\,\mu$s other cracks begin to propagate and grow in length including one outer crack (4) but mostly inner cracks (5-9,11). Conversely, as shown in Fig. 4.8c, the shear bands do not demonstrate substantial growth during the visible window of time after the passage of the planar shock front ($t = 0.4 - 1.4\,\mu$s). Instead, the shear bands generally grew during the initial shock compression and maintain relatively constant length or they grow slowly after the shock passage.

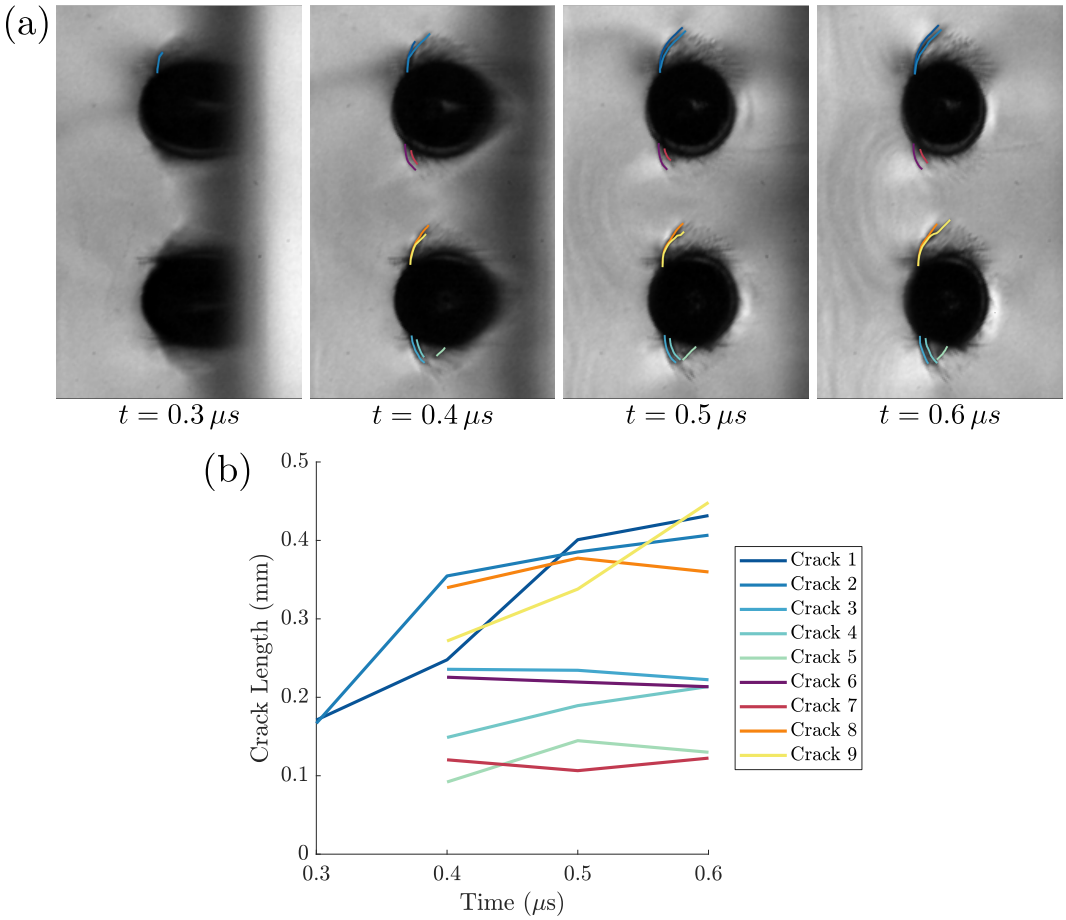

Figure 4.9: Experiment 0.9V crack profile evolution with time. (a) Cracks are tracked and plotted over the deformation images for several representative time instances. (b) Crack length estimates from tracking are displayed as a function of time.

Turning now to experiment 0.9V, only cracks are tracked due to lower spatial resolution and decreased spacing between shear bands making it difficult to

distinguish between individual features with sufficient confidence to quantitatively track them. Hence, it is not true that fewer cracks and shear bands grow, but rather that fewer concretely traceable cracks and shear bands are identified. Considering the cracks which were tracked, experiment 0.9V shows a preference for cracking at the top of the pores (e.g., cracks 1,2,8,9), with cracks on the bottom of the pores nucleating initially, but not growing until later time instances, as shown qualitatively in Fig. 4.5. These later time instances were not quantitatively tracked because of image blurring which distorted the ability to make an accurate estimate of crack contours. However, it is still discernible in Fig. 4.5 that cracks 6 and 7 begin to grow again at $t = 1.0\,\mu$s, while cracks 3, 4, and 5 remain approximately constant beyond $t = 0.6\,\mu$s.

One might conclude that the tendency, in this experiment, toward crack propagation on the tops of pores is simply an effect of impact tilt causing preferential crack location. However, experiment 0.9V was conducted with impact tilt of only 0.25 mrad, making it highly unlikely for tilt to predispose cracks in either direction. Instead, this experiment suggests the preferential crack sites (with respect to top, bottom, inner, or outer) at early time instances to be highly stochastic.

Experiment 0.8V indicates that, for the initial crack growth phase ($t \approx 0.3 - 0.5\,\mu$s) the outside locations may be preferred relative to inside locations, while experiment 0.9V suggests that this site preference has substantial stochasticity. It is possible that the site preference in both experiments is stochastic. However, when evaluating mechanisms for crack suppression which may be active in experiment 0.8V, numerical simulation results reveal a substantial pressure concentration between the pores which may partially suppress crack growth on the inner surfaces. In this case, one can understand the inner surface crack growth (cracks 8 and 9 on the top surface of the bottom pore) in experiment 0.9V to indicate the driving force for shear cracking has overcome the normal stress-dependent shear resistance. To conclusively understand this potential competition or stochasticity, future experiments exploring higher impact stresses and varied spacing (hence, partially decoupling driving forces and pressure concentrations between pores) would be necessary.

Beyond the initial crack growth stage, both experiments exhibit late stage crack growth at $t \approx 0.6 - 1.0\,\mu$s. In both cases, the late stage crack growth

is predominantly experienced by cracks on the inner surfaces, suggesting an interaction mechanism between neighboring pores to be responsible for this late crack growth. This idea will be explored in Section 4.5.4.

The discussion above has focused on the timing of crack propagation relative to the nucleation location in the vertical (X_2) dimension (inner or outer pore surface). However, the dependence of nucleation location on the horizontal (X_1) dimension is also of interest. To understand this aspect of shear band and crack propagation in pore collapse, the final length of each crack and shear band is computed and compared to the deformed position of nucleation, x_1, in Fig. 4.10. Here, $x_1 = 0$ indicates the center of the pore at the first time step after the planar shock passes the pore. While not an exact measurement of deformed position, this comparison provides insight to the overall trends.

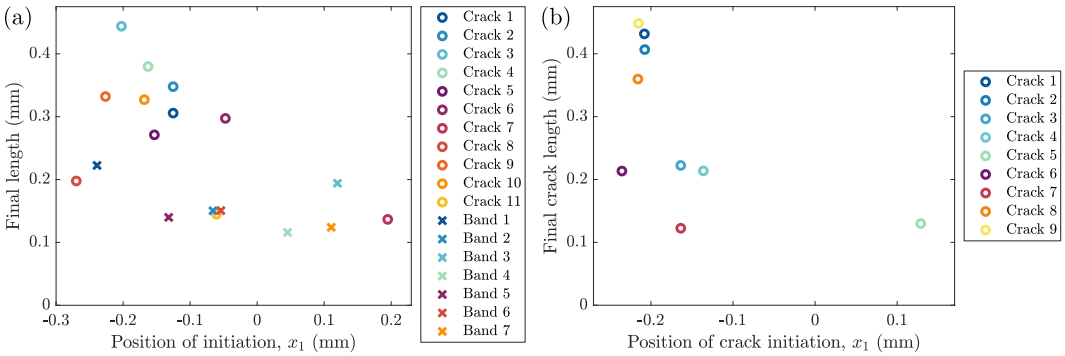

Figure 4.10: Final feature (crack (o) or shear band (x)) length as a function of initiation location. (a) Experiment 0.8V. (b) Experiment 0.9V. Note that cracks 1, 2, and 3 in experiment 0.8V may have grown longer, beyond the camera's field of view.

The results of Fig. 4.10 for both experiments 0.8V and 0.9V show a heavy concentration of cracks and dominant shear bands which nucleate on the left (upstream) side of the pores. This confirms what was visually apparent from the raw images. While shear bands nucleate somewhat uniformly at the top and bottom of the pores, the cracks and most dominant, severe shear bands tend to nucleate on the upstream side of the pore. Additionally, there is a clear trend in which the longest cracks nucleate on the left side of the pore. The mechanisms for these tendencies will be discussed further in Section 4.5.3.

Finally, it is worth noting that there appears to be a limit to the crack growth around 0.45 mm in length, approximately the radius of the pore. This is consistent with prior results on single pore experiments by Lawlor et al. [20] in

which elastostatic theory was used to predict the crack arrest location based on a simple driving force that captured the competition of shear stress and normal stress-dependent shear resistance at the crack surface. This consistent limit confirms that the region of influence of the pore, in which the shear stress is elevated, is the limiting factor for shear crack propagation during pore collapse. Further work focused on varied pore spacing may reveal a distance at which the regions of influence overlap enough that the cracks are able to connect and create a longer crack, as was previously observed by Lovinger et al. through post-mortem measurements [19]. Such behavior would be critical for understanding the role of pore networks on catastrophic failure in structures made of porous materials. Tensile unloading of these cracks also warrants future investigation.

4.5.3 Baroclinicity and strain rate as driving mechanisms for shear banding and cracking

Having discussed the tendency for strong shear localization and shear cracking to develop at the top left and bottom left regions of the pores during collapse, a natural question follows: what mechanisms determine the location at which shear localization and cracking occur? One may instinctively think of equivalent shear stress and shear strain rate as the driving mechanisms for such shear localization. To evaluate the utility of these quantities for identification of the regions in which shear localization occurs, numerical simulations are conducted as in Section 4.5.1, with negligible thermal softening, in order to evaluate the imposed loading from the planar shock onto the material around the pore.

The results from these simulations are presented in Fig. 4.11, and the Mises stress and Tresca shear strain rate are plotted in Fig. 4.11a,b. The strain rate plots show the rich wave interactions generated by diffraction off of the pore, with the longitudinal diffracted wave first propagating radially outward, followed by the shear diffracted wave which propagates at a slower speed. Most interesting for the present discussion, however, is the concentration of shear stress and strain rate near the pore. Shear stress appears to broadly concentrate around the pore with a slightly larger concentration near the top and bottom of the pores. Overall, the concentrated regions of shear stress are consistent with experimentally observed shear banding locations, but it not a

very precise metric for predicting regions of shear localization. Shear strain rate, on the other hand, is distinctly concentrated in the areas on the top and bottom of the pore where shear bands initiate, and is much lower in the front and back regions that do not exhibit shear banding. While strain rate appears to be an excellent indicator of where shear bands are likely to form, it still does not provide insight about the locations for shear cracking or the most severe shear band development. To answer that question, one must turn to the concept of baroclinicity in the fluid dynamics community.

In the analogous problem in fluid mechanics, shock-bubble interaction or bubble collapse [11, 12], the planar shock loading of bubbles in fluids generates various instabilities during the collapse of the bubble, typically centering around substantial vorticity generation near the location where cracks are observed in the present pore collapse experiments. Baroclinicity, defined in Eq. (4.9) as the misalignment between pressure (p) and density (ρ) gradients, is considered to be the primary source of vorticity generation in this setting [13], leading to the aforementioned instabilities. The instabilities in bubble collapse experiments are reminiscent of the Richtmyer-Meshkov instability (RMI) [50, 51], which is observed primarily in fluids, but also in solid materials at extreme pressures (i.e., hydrodynamic regime). Baroclinicity has been found to play a critical role in RMI, and competes with material strength to determine material stability [52, 53]. The baroclinicity vector is defined as

$$\boldsymbol{B} = \frac{1}{\rho^2} \left(\nabla \rho \times \nabla p \right) \tag{4.9}$$

of which the third component (B_3) is important in the present coordinate system.

The computed baroclinicity from numerical simulations is presented in Fig. 4.11c, in which one observes large concentrations of baroclinicity, during the shock wave passage, in the same region in which shear cracking was observed experimentally. Elsewhere, minimal baroclinicity is generated. This result is most clearly conveyed by Fig. 4.12a which displays the extrema of baroclinicity at each material point, considered across all time instances of the simulation. One clearly sees the concentrated regions on the top left and bottom left of the pores, coinciding very closely with the experimental locations of severe shear band development and shear cracking. The combination of the planar shock loading and spherical material interface (PMMA with air) generates this

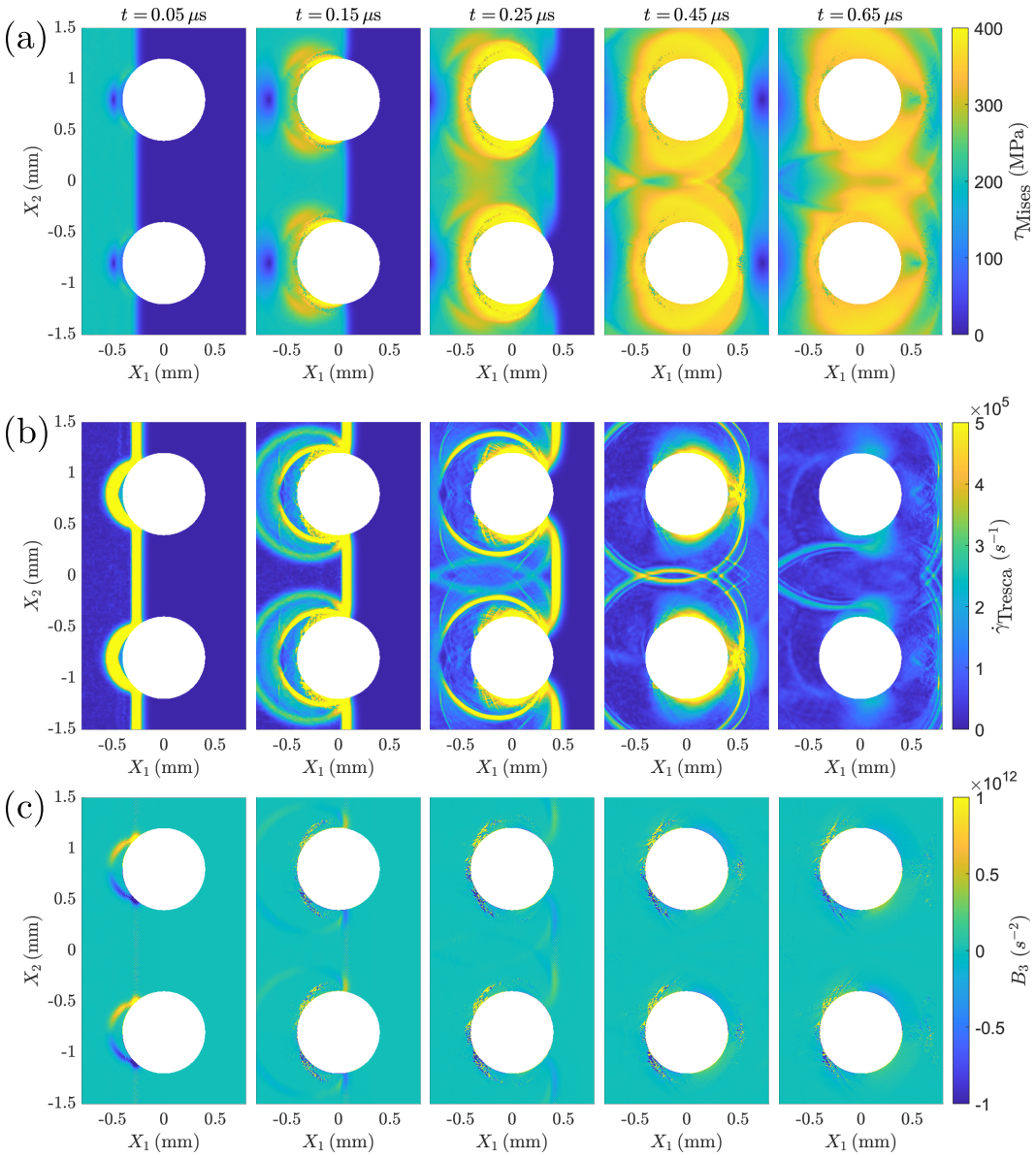

Figure 4.11: Analysis of shock wave loading on the two vertical pores configuration. Results from numerical simulations at 0.65 GPa impact stress are presented in undeformed coordinates, with thermal softening removed, in order to visualize the imposed loading in the absence of shear localization. Selected time instances are displayed for (a) Mises stress, (b) Tresca strain rate, and (c) baroclinicity, which reveal interesting mechanics as follows. (a) Shear stress concentrations around the pores. (b) Strain rate concentrations at the top and bottom of the pores; intricate diffracted wave patterns (both longitudinal and shear), including the development of head waves between the longitudinal and shear diffracted waves ($t = 0.25\,\mu s$); and enhancement of strain rate concentrations by the shear diffracted wave interaction with neighboring pore. (c) The regions of extreme baroclinicity at $t = 0.05\,\mu s$ in the upper left and lower left regions of the pores.

large baroclinicity and corresponding baroclinic torque. While in fluids, the baroclinicity gives rise to substantial vorticity and instabilities, materials with strength (i.e., solids in the strength-dominated regime of shock compression) instead respond with shear deformation in these regions, which can lead to localization as was seen in the present experiments.

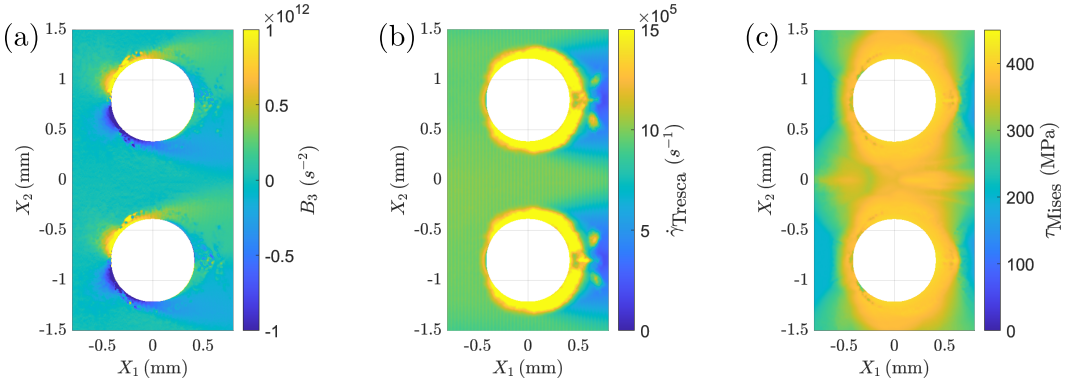

Figure 4.12: Summary of numerical simulations without thermal softening at 0.65 GPa impact stress. At every material location, the extrema is calculated across all simulated time instances, and compiled into a single plot for (a) baroclinicity, (b) Tresca shear strain rate, and (c) Mises stress. These results provide an overview of the locations of concentrated imposed loading during the shock compression and pore collapse event.

Figure 4.12b,c presents similar cumulative results for strain rate and shear stress, respectively. These results reiterate the observations that shear stress is not the best predictor of shear banding in these experiments, strain rate is an excellent indicator of where shear bands are likely to form, and baroclinicity is an excellent indicator of failure through severe shear bands and shear cracking. This finding has important implications for predicting the behavior of irregular pore geometries when designing porous structures. Accurate prediction could enable designs to leverage material enhancement (e.g., energy absorption via large deformations) while mitigating the undesirable localization and failure phenomenon observed in the spherical geometry in this work.

4.5.4 Diffracted wave propagation as a possible mechanisms for failure enhancement

Throughout this study, several instances have arisen which demonstrate the importance of interactions between pores. The two primary examples of this are (1) the shifting of impact stress thresholds for failure mode initiation and

(2) late stage crack growth on inner surfaces of the pores, discussed in Section 4.3.1 and Section 4.5.2, respectively. In the case of failure mode shifting, the failure occurs at a significantly later time when compared to the single pore experiments which demonstrate the same failure mode, but at higher impact stresses (e.g., 0.4V and 0.6S both demonstrate shear band evolution as measured by DIC). Similarly, in the crack propagation from experiments 0.8V and 0.9V, some cracks grow very quickly after the shock wave passes, while others are delayed by several hundred nanoseconds. One possibility for these apparently time-delayed behaviors is that the loading imposed by the initial planar shock wave was insufficient to initiate localization or failure on its own, but diffracted waves from a neighboring pore could supply sufficient additional loading and perturbation to cause localization/failure. This idea is not without predecessors, as the interactions between collapsing cavities have been attributed to wave interactions [14, 25].

To investigate this possibility, three-dimensional numerical simulations for an impact stress of 0.65 GPa are conducted, using the same framework as in Section 4.5.3. In this case, identical simulations were conducted on two different geometries—a single pore, and a pore with a neighbor situated in the vertical configuration, as in the vertical pore experiments. The results for the single pore simulation are then subtracted from the results of the pore with a neighbor, to isolate the effects of pore interactions. This concept is depicted in Fig. 4.13b which shows the two pores, Pore 2 being the pore of interest, and Pore 1 being the neighboring pore that imposes interacting loads on Pore 2. The planar shock, longitudinal diffracted wave, and shear diffracted wave are also included in the schematic.

Preliminary consideration of the simulation results reveals insignificant interaction in the baroclinicity and Mises stress fields. However, the shear diffraction wave is observed to carry significant strain rate perturbation, as is seen at $t = 0.55\,\mu$s and $t = 0.7\,\mu$s in Fig. 4.13c. The arrival time of the shear diffraction wave is estimated to be $0.73\,\mu$s after the initial planar shock wave arrival at the pore surface. This may explain the delayed timing of the failures observed in experiments 0.4V and 0.6V (in which an impact stress threshold shift was observed) compared to their single pore counterparts which exhibited the same failure modes, 0.6S and 0.8S. This comparison is plotted in Fig. 4.13a. The time at which the shear diffraction reaches the neighboring

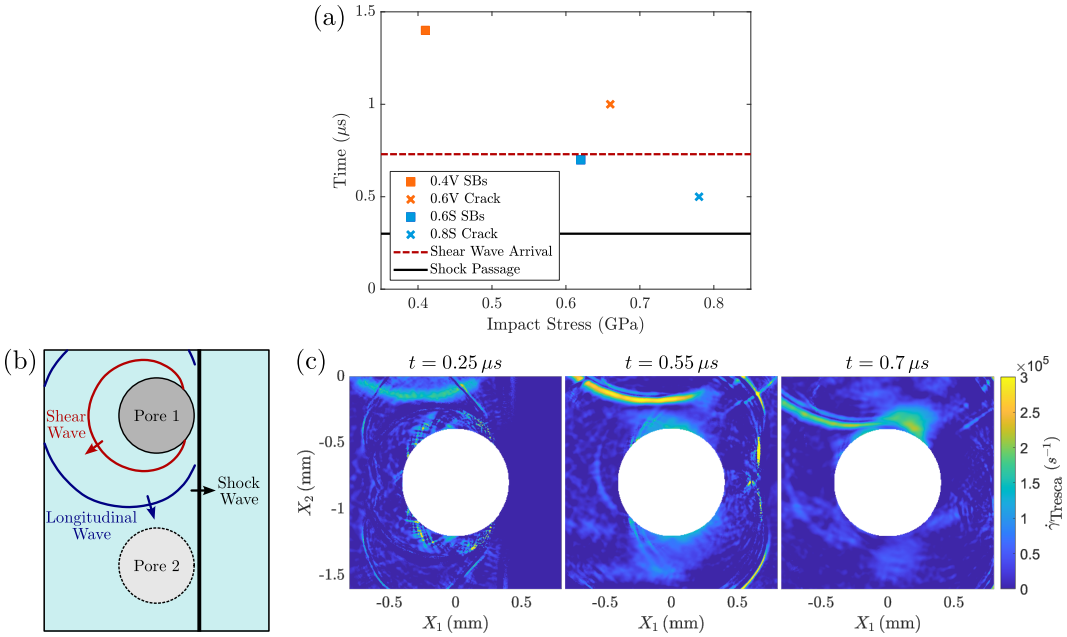

Figure 4.13: Analysis of failure threshold shifting. (a) Plot of initiation time for relevant experiments in this work (0.4V - shear bands, 0.6V - crack) compared to single pore experiments [20] (0.6S - shear bands, 0.8S - crack). (b),(c) The effect of longitudinal and shear diffracted waves from Pore 1 in the vicinity of Pore 2. (b) Depiction of analysis conducted and the propagation of the shock wave, longitudinal diffracted wave, and shear diffracted wave. (c) Selected time instances of numerical simulations at 0.65 GPa impact stress, highlighting the imposed Tresca strain rate on Pore 2 from the diffracted waves off of Pore 1.

pore is plotted as an orange dotted line, showing a clear differentiation between the timing of failure in single pore experiments, which consistently occurs before the shear diffracted wave timing, and the failure in vertically configured two-pore experiments with shifted failure thresholds, where the failure occurs shortly after the predicted arrival time of the shear wave. For experiments 0.8V and 0.9V, which had slightly closer pore spacing, the timing of the shear diffracted wave arrival at the neighboring pore is estimated to be $t = 0.62\,\mu$s and $t = 0.55\,\mu$s, respectively. These times coincides with, and may explain, the late stage crack growth on inner surfaces, especially in experiment 0.8V at approximately $t = 0.6 - 0.8\,\mu$s, and to a lesser extent in 0.9V at approximately $t = 1.0\,\mu$s.

In summary, failure via shear localization during pore collapse of neighboring pores appears to occur mostly independently of the neighbors during early time instances. However, shear diffraction waves provide perturbing loads to neighboring pores which may cause further localization and failure responses

which otherwise would not have occurred. These results provide supporting evidence for the shear diffraction wave to be the governing mechanism behind the pore interactions observed in these experiments. To more rigorously investigate the shear diffraction wave as a primary mechanism for pore interactions in this impact stress regime, additional experiments and simulations would be necessary in various pore configurations and pore spacings.

4.6 Conclusion

4.6.1 Summary

The study presented here has successfully conducted pore collapse experiments in PMMA across impact stresses of $0.4 - 0.9$ GPa and leveraged both DIC and shadowgraphy to investigate deformation, failure, and interaction mechanisms between pore arrays during collapse. Numerical simulations were also conducted, which demonstrated the ability of 3D dynamic finite element analysis and the Johnson-Cook plasticity model to capture some of the more prevalent features of pore collapse and shear localization, such as the impact stress at which strong shear bands develop, the common modalities of shear bands, and the preferred nucleation sites for shear bands and cracks. The shadowgraphy method enabled *in-situ* visualization of shear bands and shear cracks, providing the first direct visualization of these features and their evolution during the pore collapse process. Additionally, shadowgraphy and DIC measurements revealed a secondary set of apparently weaker shear bands which grow in a more diffuse fashion. Finally, shear band spacing was found to decrease substantially with increasing impact stress, which was accurately captured by the Grady-Kipp model [46].

Analysis of experimental results brought together theoretical and numerical models which elucidated the physics which governed the aforementioned behaviors. Experimental measurements of shear band spacing revealed a distinct decrease in shear band spacing with increasing impact stress, which was found to be consistent with theoretical models [46, 47]. Further, the excellent match with the Grady-Kipp (GK) model highlighted the ability to predict the spacing of mature shear bands, which were measured in experiment, while Wright and Ockendon's estimate for minimum spacing indicated the likely presence of smaller bands near the pore surface which did not grow beyond the initial nucleation stage. Comparisons with previous experiments on single pores

in PMMA [20] uncovered a shift in the impact stresses which are necessary to grow the secondary shear bands and the dominant shear bands and shear cracks. Tracking of crack and shear band features revealed distinct trends in the locations of strong shear bands and cracks, while also bringing attention to the differences in early stage crack growth and late stage crack growth. Leveraging numerical simulations to investigate the physics involved in the various observed phenomena, baroclinicity was identified as the driving mechanism which concentrates strong shear localization and cracking in the regions at the top left and bottom left (upstream side) of the pore. Finally, shear diffraction waves were proposed as a potential interaction mechanism between pores, which explains both the shift in failure mode thresholds and the timing and location of late stage crack growth behaviors.

Overall, these experiments provided a rich view into the detailed evolution of shear localization during pore collapse. Moreover, they revealed that pore interactions (in this impact stress regime) are subtle and nuanced. Their effect can be significant, but appears to be accomplished primarily through perturbations such as via diffracted waves, rather than in a direct way through overlapping regions of shear stress concentrations.

4.6.2 Future work

The experiments conducted and analyzed here took place in a impact stress regime in which significant transitions occur in shear localization behaviors. While the results are interesting in their own right and have revealed many insights regarding the pore collapse phenomenon, they also beg several questions. Among these is how the localization behaviors and pore interaction mechanisms evolve with increasing impact stress and with different pore array configurations. At higher impact stresses or closer spacings, it is possible that cracks begin connecting and generating more catastrophic failure, such as Lovinger et al. observed post-mortem [19]. The role of impact stress, spacing between pores, and whether this occurs in compression or during tensile unloading are important topics to be addressed through future experiments. Finally, the role of length scale and complex geometries such as non-spherical pores or connected pore networks, are of critical interest for practical understanding of the implications of pore collapse in applications, and should be explored.

APPENDIX

4.A Shear Band Location Tracking

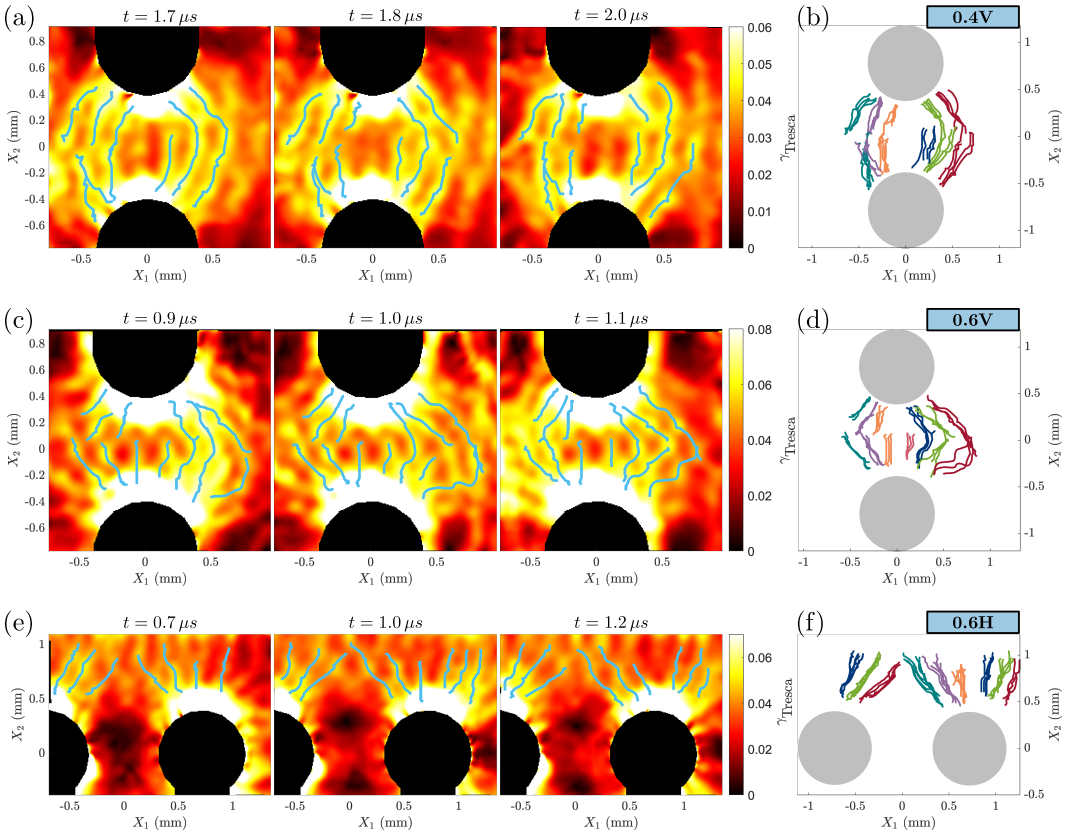

Figure 4.A.1: Evolution of shear bands identified with DIC. (a),(c),(e) display several time instances of full field Tresca strain in the reference coordinate system (X_1, X_2), along with the tracked shear band contours for experiments 0.4V, 0.6V, and 0.6H, respectively. The tracked bands are then produced in (b),(d),(f) which overlay the results from several time instances.

To avoid mistakenly treating noise in DIC measurements as physical features, the identification of shear bands in experiments 0.4V, 0.6V, and 0.6H is partially automated based on automatic identification of local maxima in addition to user input to restrict shear band identification to the regions which are consistent from frame to frame. This process is accomplished by first taking user input to track the shear band locations manually for each frame of good DIC data. Good data is considered to be data obtained from correlating raw images which were free of distortions or blurriness. The good frames of data are manually identified as well. Next, the DIC data is analyzed in Matlab, using the watershed algorithm to identify all local maxima. The local maxima are

then cross-checked against the manual inputs, which are considered as initial guesses. Local maxima data is trimmed to only the data which is similar to the initial guess. Finally, branches of maxima data are trimmed, and the data is smoothed.

The final tracked shear band contours are plotted at representative time instances in Fig. 4.A.1a,c,e. The data from all good frames are then compiled into overlaid plots in the undeformed coordinate system in Fig. 4.A.1b,d,f. These tracked band locations in undeformed coordinates prove to remain constant over time, which is expected for any physical deformation feature. Thus, the analysis reveals that the bands tracked here are real features that can be reported and analyzed.

References

[1] W. Herrmann, "Constitutive equation for the dynamic compaction of ductile porous materials," Journal of Applied Physics **40**, 2490–2499 (1969).

[2] F. Lu, S. Huan, and J. Ding, "Viscoplasticity and porosity effects on the shock propagation in PMMA and porous aluminum oxide," AIP Conference Proceedings **309**, 1013–1015 (1994).

[3] S. Bonnan, P.-L. Hereil, and F. Collombet, "Experimental characterization of quasi static and shock wave behavior of porous aluminum," Journal of Applied Physics **83**, 5741–5749 (1998).

[4] E. Chiu, A. Needleman, S. Osovski, and A. Srivastava, "Mitigation of spall fracture by evolving porosity," Mechanics of Materials **184**, 104710 (2023).

[5] C. Czarnota, A. Molinari, and S. Mercier, "The structure of steady shock waves in porous metals," Journal of the Mechanics and Physics of Solids **107**, 204–228 (2017).

[6] Z. Lovinger, C. Czarnota, S. Ravindran, A. Molinari, and G. Ravichandran, "The role of micro-inertia on the shock structure in porous metals," Journal of the Mechanics and Physics of Solids **154**, 10.1016/j.jmps.2021.104508 (2021).

[7] R. G. Kraus, D. J. Chapman, W. G. Proud, and D. C. Swift, "Hugoniot and spall strength measurements of porous aluminum," Journal of Applied Physics **105**, 10.1063/1.3133237 (2009).

[8] Z. Lovinger, C. Czarnota, S. Ravindran, C. Kettenbeil, A. Molinari, and G. Ravichandran, "Shock structure and spall behavior of porous aluminum," in AIP Conference Proceedings, Vol. 2272 (Nov. 2020).

[9] G. H. Markstein, "A shock-tube study of flame front-pressure wave interaction," Symposium (International) on Combustion **6**, Sixth Symposium (International) on Combustion, 387–398 (1957).

[10] G. Rudinger, "Shock wave and flame interactions," in Combustion and propulsion, third agard colloquium (Pergamon Press, London, 1958), pp. 153–182.

[11] J. F. Haas and B. Sturtevant, "Interaction of weak shock waves with cylindrical and spherical gas inhomogeneities," Journal of Fluid Mechanics **181**, 41–76 (1987).

[12] D. Ranjan, J. Oakley, and R. Bonazza, "Shock-bubble interactions," Annual Review of Fluid Mechanics **43**, 117–140 (2011).

[13] J. J. Quirk and S. Karni, "On the dynamics of a shock–bubble interaction," Journal of Fluid Mechanics **318**, 129–163 (1996).

[14] J. P. Dear and J. E. Field, "A study of the collapse of arrays of cavities," Journal of Fluid Mechanics **190**, 409–425 (1988).

[15] T. W. Wright and J. W. Walter, "On stress collapse in adiabatic shear bands," Journal of the Mechanics and Physics of Solids **35**, 701–720 (1987).

[16] Y. L. Bai and B. Dodd, *Adiabatic shear localization: Occurrence, theories, and applications* (Pergamon Press, London, 1992).

[17] A. Molinari, "Collective behavior and spacing of adiabatic shear bands," Journal of the Mechanics and Physics of Solids **45**, 1551–1575 (1997).

[18] E. M. Escauriza, J. P. Duarte, D. J. Chapman, M. E. Rutherford, L. Farbaniec, J. C. Jonsson, L. C. Smith, M. P. Olbinado, J. Skidmore, P. Foster, T. Ringrose, A. Rack, and D. E. Eakins, "Collapse dynamics of spherical cavities in a solid under shock loading," Scientific Reports **10**, 10.1038/s41598-020-64669-y (2020).

[19] Z. Lovinger and R. Kositski, "Shear localization as a damage mechanism in pore collapse under shock compression," International Journal of Impact Engineering **193**, 10.1016/j.ijimpeng.2024.105039 (2024).

[20] B. P. Lawlor, V. Gandhi, and G. Ravichandran, "Full-field quantitative visualization of shock-driven pore collapse and failure modes in PMMA," Journal of Applied Physics **136**, 225901 (2024).

[21] J. Lind, M. Nelms, M. Kumar, and N. Barton, "Observation of shear band localization in Ti-6Al-4V through in-situ imaging under dynamic compression conditions," in AIP Conference Proceedings, Vol. 3066, 1 (AIP Publishing, 2024).

[22] J. Lind, M. D. Nelms, A. K. Robinson, M. Kumar, and N. R. Barton, "Examining material constitutive response under dynamic compression and large plastic strains using in situ imaging of hole closure," Acta Materialia **206**, 10.1016/j.actamat.2020.116584 (2021).

[23] M. Nelms, J. Lind, J. Margraf, S. B. Qamar, J. Herrington, A. Robinson, M. Kumar, and N. Barton, "High-rate strength response of tantalum from dynamic hole closure experiments," Journal of Applied Physics **132**, 10.1063/5.0107391 (2022).

[24] Y. Tomita, A. Shima, and T. Ohno, "Collapse of multiple gas bubbles by a shock wave and induced impulsive pressure," Journal of Applied Physics **56**, 125–131 (1984).

[25] A. B. Swantek and J. M. Austin, "Collapse of void arrays under stress wave loading," Journal of Fluid Mechanics **649**, 399–427 (2010).

[26] B. P. Lawlor, V. Gandhi, and G. Ravichandran, "An internal digital image correlation technique for high-strain rate dynamic experiments," Experimental Mechanics **65**, 407–419 (2025).

[27] M. A. Sutton, J. J. Orteu, and H. Schreier, *Image correlation for shape, motion and deformation measurements: Basic concepts, theory and applications* (Springer US, 2009), pp. 1–321.

[28] G. S. Settles, *Schlieren and shadowgraph techniques: Visualizing phenomena in transparent media* (Springer Science & Business Media, 2001).

[29] K. T. Ramesh, "High rates and impact experiments," in *Springer handbook of experimental solid mechanics* (Springer, 2008), pp. 929–960.

[30] M. A. Meyers, *Dynamic behavior of materials* (John Wiley & Sons, Ltd, Sept. 1994).

[31] Correlated Solutions, *VIC-2D (version 6.2) software manual* (2020).

[32] Hibbitt, Karlsson, and Sorenson, *Abaqus/Explicit: User's manual, version 6.2* (Hibbitt, Karlsson and Sorenson Inc., 2001).

[33] G. R. Johnson and W. Cook, "A constitutive model and data for metals subjected to large strains, high strain rates and high temperatures," Proceedings of the 7th International Symposium on Ballistics, 541–547 (1983).

[34] T. J. Holmquist, J. Bradley, A. Dwivedi, and D. Casem, "The response of polymethyl methacrylate (PMMA) subjected to large strains, high strain rates, high pressures, a range in temperatures, and variations in the intermediate principal stress," European Physical Journal: Special Topics **225**, 343–354 (2016).

[35] N. S. Brar, V. S. Joshi, and B. W. Harris, "Constitutive model constants for Al7075-T651 and Al7075-T6," in AIP Conference Proceedings, Vol. 1195 (2009), pp. 945–948.

[36] L. M. Barker and R. E. Hollenbach, "Shock-wave studies of PMMA, fused silica, and sapphire," Journal of Applied Physics **41**, 4208–4226 (1970).

[37] D. Lacina, C. Neel, and D. Dattelbaum, "Shock response of poly [methyl methacrylate] (PMMA) measured with embedded electromagnetic gauges," Journal of Applied Physics **123**, 10.1063/1.5023230 (2018).

[38] J. L. Jordan, D. Casem, and M. Zellner, "Shock response of polymethylmethacrylate," Journal of Dynamic Behavior of Materials **2**, 372–378 (2016).

[39] D. Rittel and A. Brill, "Dynamic flow and failure of confined polymethylmethacrylate," Journal of the Mechanics and Physics of Solids **56**, 1401–1416 (2008).

[40] N. K. Rai, E. M. Escauriza, D. E. Eakins, and H. S. Udaykumar, "Mechanics of shock induced pore collapse in poly(methyl methacrylate) (PMMA): Comparison of simulations and experiments," Journal of the Mechanics and Physics of Solids **143**, 10.1016/j.jmps.2020.104075 (2020).

[41] S. P. Marsh, *LASL shock hugoniot data*, Vol. 5 (University of California Press, 1980).

[42] D. J. Steinberg, *Equation of state and strength properties of selected materials* (Lawrence Livermore National Laboratory, Livermore, 1996).

[43] V. F. Nesterenko, M. A. Meyers, and T. W. Wright, "Self-organization in the initiation of adiabatic shear bands," Acta Materialia **46**, 327–340 (1998).

[44] Q. Xue, M. A. Meyers, and V. F. Nesterenko, "Self-organization of shear bands in titanium and Ti–6Al–4V alloy," Acta Materialia **50**, 575–596 (2002).

[45] Q. Xue, V. F. Nesterenko, and M. A. Meyers, "Evaluation of the collapsing thick-walled cylinder technique for shear-band spacing," International Journal of Impact Engineering **28**, 257–280 (2003).

[46] D. E. Grady and M. E. Kipp, "The growth of unstable thermoplastic shear with application to steady-wave shock compression in solids," Journal of the Mechanics and Physics of Solids **35**, 95–119 (1987).

[47] T. W. Wright and H. Ockendon, "A scaling law for the effect of inertia on the formation of adiabatic shear bands," International Journal of Plasticity **12**, 927–934 (1996).

[48] M. J. Assael, S. Botsios, K. Gialou, and I. N. Metaxa, "Thermal conductivity of polymethyl methacrylate (PMMA) and borosilicate crown glass BK7," International Journal of Thermophysics **26**, 1595–1605 (2005).

[49] The MathWorks Inc., *Matlab version: 9.11.0 (r2021b)*, Natick, Massachusetts, United States, 2021.

[50] R. D. Richtmyer, "Taylor instability in shock acceleration of compressible fluids," Communications on Pure and Applied Mathematics **13**, 297–319 (1960).

[51] E. Meshkov, "Instability of a shock wave accelerated interface between two gases," NASA Tech. Trans **13**, 74 (1970).

[52] A. Subramaniam, N. S. Ghaisas, and S. K. Lele, "High-order eulerian simulations of multimaterial elastic–plastic flow," Journal of Fluids Engineering **140**, 050904 (2018).

[53] Y. Zhou, R. J. Williams, P. Ramaprabhu, M. Groom, B. Thornber, A. Hillier, W. Mostert, B. Rollin, S. Balachandar, P. D. Powell, et al., "Rayleigh–Taylor and Richtmyer–Meshkov instabilities: A journey through scales," Physica D: Nonlinear Phenomena **423**, 132838 (2021).

Chapter 5

CONCLUSIONS

5.1 Summary

The work presented in this thesis successfully developed a digital image correlation (DIC) based technique for internal strain measurements in dynamic experiments and conducted plate impact pore collapse experiments on individual pores and pore arrays in PMMA, leveraging the internal DIC technique to characterize, for the first time, the *in-situ* deformation evolution around the pores. The shadowgraphy technique was also employed to visualize the wave interactions and failure modes around the collapsing pore(s).These experiments probed the pertinent deformation responses, failure modes, and the role of pore-pore interactions during pore collapse. The roles of impact stress and pore-pore interactions were investigated through experiments across a range of impact stresses ($0.4 - 1.0\,\mathrm{GPa}$) in the strength-dominated regime, and with various pore configurations including individual pores and vertical/horizontal pore arrays. Through these experiments and corresponding theoretical/numerical analyses, shear localization was found to be a critical failure mechanism—which is highly dependent on impact stress and neighboring pore interactions—during pore collapse in PMMA.

In Chapter 2 the internal DIC technique for *in-situ*, deformation measurements during dynamic experiments was developed and validated. By embedding a DIC speckle pattern internally in mirror-polished transparent specimens, quantitative visualization inside of the specimens was enabled in conjunction with high-speed imaging and DIC software. These experiments were conducted for both low-magnification visualization in SHPB experiments and high-magnification visualization in plate impact experiments. The limiting factor for the experiments was found to be the spatial resolution of state-of-the-art high-speed cameras and the focal-plane sensitivity introduced by high-magnification optics. Beyond the technological limitations for the technique, validation of the internal DIC technique was completed by comparison to theoretical and experimental measures. The measurements showed good agreement to the validation metrics, and importantly maintained the expected uniform

deformation fields that were imposed by the respective dynamic experiments.

Chapter 3 implemented the internal DIC technique for the pore collapse problem: investigating the collapse of individual, 800 μm diameter, spherical pores under varied impact stresses. The high-speed images enabled characterization of the geometric evolution of the pore in addition to the in-plane deformation of material surrounding the pore during its collapse. Two distinct failure mode transitions were observed with increasing impact stress—first from coarse strain concentrations at the pore surface to the initiation of shear bands emanating from the pore surface, and second, to the development of fracture at the pore surface. Numerical simulations revealed the observed crack to be a shear crack propagating along the weakened material in an adiabatic shear band. Asymmetry during pore collapse was also observed and related to this crack evolution. Theoretical analysis through the Grady-Kipp model demonstrated good agreement with experimentally observed shear band spacing, and identified the measured shear bands to be mature/developed bands as opposed to those which nucleate but die out. Finally, elastostatic theory elucidated the preferred shear band and crack paths, in addition to the arrest of the crack after propagating approximately one pore radius from the surface.

Finally, Chapter 4 addresses the question of pore-pore interactions and their influence on deformation and failure, by conducting pore collapse experiments on arrays of pores. Namely, vertical and horizontal arrays of two pores are considered. For these experiments, internal DIC is implemented for lower impact stresses in which no fracture is expected, and shadowgraphy is utilized at higher stresses to qualitatively visualize the shear band and crack features. These experiments revealed pore interactions to cause shifts in the impact stress thresholds at which failure modes (both shear bands and cracks) occur, where the vertical configuration appears to enhance the driving force for failure. Comparison to shear band spacing models revealed excellent agreement across a range of impact stresses, and finite element analysis accurately reproduced many details of the shear band evolution captured via shadowgraph images. Finally, baroclinicity was identified as the dominant driving force for severe shear band development and crack propagation, and shear diffraction waves are considered as a plausible mechanism by which pores interact and enhance failure.

Based on the experiments and analysis conducted throughout this thesis, rich deformation, failure, and interaction mechanisms have been revealed at the mesoscale, which underlie the macroscopic response of porous materials. In such a complex, coupled problem, these findings simply are the beginning of what is required to fully understand the mechanics of pore collapse, the thermo-chemo-mechanical coupling, and ties between meso and macroscale responses. Some important, open areas of research are outlined below.

5.2 Future Work

Important open areas for research in pore collapse should focus on improving the understanding of real porous materials and structures under shock compression. Overall, there is a need to translate investigation at the mesoscale from idealized model scenarios, such as presented here, toward realistic porous materials, and similarly, to bridge the gap between the mesoscale and macroscale. Some specific areas of focus are as follows.

5.2.1 Technique Improvement

A most obvious next step in these investigations is to improve limiting aspects of the experimental technique. Improvement of quantitative visualization capabilities through advancements in the cutting edge of high-speed camera technologies could yield greater insight to the nuances of the failure modes observed here (through improved spatial resolution) and the temporal evolution through higher framing rates. Similarly, more controlled, optimized DIC speckling techniques at the micron scale would help minimize noise in full-field measurements. Additionally, implementation of more sophisticated optics could mitigate challenges with focal plane shifting at high stresses, and thus enable extension of the investigation to much higher impact stresses and smaller length scales. At higher stresses, one could explore the evolution of failure modes such as crack propagation, and possible connectivity between cracks of neighboring pores. The role of shear diffracted waves at increasing stresses, as the shear strength is diminished, could be explored as well. The importance of length scale is discussed below.

5.2.2 Realistic Porous Materials

In the applied, engineering domain, it is critical that the physics explored here, at a fundamental level, be extended to more realistic porous materials or structures. Some key features are the pore geometry, length scale, and the base material choice. One should consider investigation of complex pore geometries which extend beyond spherical or cylindrical pores, in addition to arrays and connected networks of pores. These complex geometries may change the localization process based on different plane wave interactions with the pores. Additionally, the length scale of pores poses, perhaps, the greatest challenge. Pores exist across length scales, primarily in the range of nanometers to hundreds of microns, while ground truth investigations via molecular dynamics [1] and experiments generally fall into the lower and upper extremes of that range, respectively—making it technically challenging to investigate several orders of magnitude within the range of interest. Exploring length scale effects within the range of relevant application scales remains an important topic of research from both numerical and experimental perspectives. This problem also ties into the topic of multiscale investigation discussed in Section 5.2.4.

For practical reasons, optically transparent materials are most advantageous for experiments. However, most applications for shock compression of porous media involve non-transparent materials, such as energetic crystals or metal alloys. Investigations have endeavored to understand the pore collapse geometry in these settings via phase contrast imaging (PCI) at synchrotron sources. Some examples include an energetic crystal embedded in Sylgard [2] and hole closure in copper [3], tantalum [4, 5], and Ti-6Al-4V [6]. Further work in this area could also use PCI to probe the internal deformation response around collapsing pores in low-z materials of interest using x-ray digital image correlation and high-z tracer particles for the speckle pattern.

5.2.3 Experimentally-Informed Modeling

Macroscopic characterization of porous materials has been primarily through empirical, continuum measurements, and through models such as the $P - \alpha$ [7] which assumes symmetric pore collapse. However, experiments at the mesoscale continue to demonstrate the asymmetry inherent in pore collapse, which has also been directly linked to localization via jetting and shear cracking. This growing experimental dataset on pore collapse and hole closure [3–6,

8–12] presents an opportunity for more sophisticated continuum theories to incorporate asymmetric collapse features and experimentally determined collapse times. Similarly, the rich experimental data provides valuable ground truth with which numerical simulations can be compared, to develop modeling capabilities which capture nuanced features from experiments, as was done for previous pore collapse experiments on PMMA [9, 13] and with molecular dynamics-consistent continuum modeling [14].

5.2.4 Multi-scale Mechanics

As discussed frequently throughout this thesis, pore collapse is inherently a multiscale problem. Research efforts at the macro, meso, micro, and nanoscales represent critical advances in the understanding of the continuum response and the response of pores at various scales observed in application. However, it is necessary to extend the local studies to elucidate the mechanisms which govern the macroscopic response. Conventional multiscale modeling for this problem, because of the incredible amount of mesh refinement necessary to reproduce physical behaviors, may be too computationally intensive. Instead, alternative approaches, such as surrogate modeling [15] appear to present promising directions. Other studies have endeavored to explain the relation between specific local and macroscale features. One example is the connection between material hardening from plastic deformation of pore collapse to the changes in spall strength for porous materials [16]. Another question arising from recent mesoscale experimental works demonstrating shear localization in pore collapse [6, 10, 11] is under what conditions the shear localization and fracture develop large connected failure surfaces and how those surfaces may lead to macroscopic, catastrophic failure. Or, do the cracks simply arrest and have no bearing on the macroscopic structure? If shear cracking at pore surfaces leads to lower spall strength, then perhaps a material's inherent propensity toward shear banding would be an indicator for the effect of porosity on spall strength. Many such questions exist which warrant further investigation.

5.2.5 Thermo-chemo-mechanical Analysis

While the quantitative visualization presented here has provided novel insights to the deformation and failure in pore collapse, there still remain mechanical aspects which are not understood. To supplement the DIC deformation mea-

surements, photoelasticity could help to capture the finer details of the stress state near bands and cracks. Similarly, quantitative Schlieren, in place of shadowgraphy, could be used to characterize the refractive index change across the shock front and diffracted waves, providing a window into the structure of shock waves in solids. This would be of particular interest to improving understanding of shock wave interactions with irregular surfaces in solids.

As mentioned previously, the mechanics of pore collapse are intrinsically coupled to thermal effects arising from shock heating and localized plastic work, resulting in significant temperature rise. Conducting *in-situ* thermal measurements would provide a strong complement to the deformation measurements presented here—clarifying the thermal evolution during shear band growth and crack propagation. These results would also provide novel data and physical understanding which could inform continuum modeling efforts. Finally, to complete the thermo-chemo-mechanical analysis, mechanical and thermal measurements of pore collapse in energetic crystals could clarify the role of different proposed mechanisms for hot spot generation in addition to the evolution of temperature and reaction initiation.

5.2.6 Connections to Fluid Dynamics

The analysis put forth in this thesis has just touched on the connections between the classical bubble collapse problem in fluid dynamics and the pore collapse problem in solid mechanics which introduces significant material strength to the problem. Some connections between the problems, such as the role of baroclinicity in localization and the importance of wave interactions in governing the collapse of bubble/pore arrays, have been identified and discussed. But, there are likely to be additional, deeply rooted connections between the findings in fluid dynamics communities and the pore collapse problem, which warrant further consideration.

References

[1] P. Erhart, E. M. Bringa, M. Kumar, and K. Albe, "Atomistic mechanism of shock-induced void collapse in nanoporous metals," Physical Review B **72**, 052104 (2005).

[2] C. J. Blum-Sorensen, C. A. Duarte, J. D. Drake, N. E. Kerschen, K. Fezzaa, M. Koslowski, W. W. Chen, and S. F. Son, "Phase contrast x-

ray imaging of the collapse of an engineered void in single-crystal hmx," Propellants, Explosives, Pyrotechnics **47**, e202100297 (2022).

[3] J. Lind, M. D. Nelms, A. K. Robinson, M. Kumar, and N. R. Barton, "Examining material constitutive response under dynamic compression and large plastic strains using in situ imaging of hole closure," Acta Materialia **206**, 10.1016/j.actamat.2020.116584 (2021).

[4] J. Lind, R. Carson, N. Bertin, and M. Nelms, "High strain-rate strength response of single crystal tantalum through in-situ hole closure imaging experiments," Materialia **37**, 102219 (2024).

[5] M. Nelms, J. Lind, J. Margraf, S. B. Qamar, J. Herrington, A. Robinson, M. Kumar, and N. Barton, "High-rate strength response of tantalum from dynamic hole closure experiments," Journal of Applied Physics **132**, 10.1063/5.0107391 (2022).

[6] J. Lind, M. Nelms, M. Kumar, and N. Barton, "Observation of shear band localization in Ti-6Al-4V through in-situ imaging under dynamic compression conditions," in AIP Conference Proceedings, Vol. 3066, 1 (AIP Publishing, 2024).

[7] M. M. Carroll and A. C. Holt, "Static and dynamic pore-collapse relations for ductile porous materials," Journal of Applied Physics **43**, 1626–1636 (1972).

[8] V. S. Glazkov, O. N. Ignatova, A. N. Malyshev, S. S. Nadezhin, A. M. Podurets, V. A. Raevsky, and O. A. Tyupanova, "Peculiarities of high-rate deformation of copper upon convergence of cylindrical channels by action of shock waves," in AIP Conference Proceedings, Vol. 1195 (2009), pp. 735–738.

[9] E. M. Escauriza, J. P. Duarte, D. J. Chapman, M. E. Rutherford, L. Farbaniec, J. C. Jonsson, L. C. Smith, M. P. Olbinado, J. Skidmore, P. Foster, T. Ringrose, A. Rack, and D. E. Eakins, "Collapse dynamics of spherical cavities in a solid under shock loading," Scientific Reports **10**, 10.1038/s41598-020-64669-y (2020).

[10] Z. Lovinger and R. Kositski, "Shear localization as a damage mechanism in pore collapse under shock compression," International Journal of Impact Engineering **193**, 10.1016/j.ijimpeng.2024.105039 (2024).

[11] B. P. Lawlor, V. Gandhi, and G. Ravichandran, "Full-field quantitative visualization of shock-driven pore collapse and failure modes in PMMA," Journal of Applied Physics **136**, 225901 (2024).

[12] N. R. Barton, R. A. Austin, J. Lind, J. Margraf, and M. D. Nelms, "Vanadium response at high strain rates and large strains," AIP Conference Proceedings **3066**, 570001 (2024).

[13] N. K. Rai, E. M. Escauriza, D. E. Eakins, and H. S. Udaykumar, "Mechanics of shock induced pore collapse in poly(methyl methacrylate) (PMMA): Comparison of simulations and experiments," Journal of the Mechanics and Physics of Solids **143**, 10.1016/j.jmps.2020.104075 (2020).

[14] J. Herrin, C. Okafor, C. R. Picu, T. Sewell, J. Brennan, J. P. Larentzos, and H. S. Udaykumar, "Length scale and grid resolution effects in the simulation of shear and energy localization during pore collapse in shocked energetic crystals," Journal of Applied Physics **137**, 125903 (2025).

[15] S. W. Cheung, Y. Choi, H. K. Springer, and T. Kadeethum, "Data-scarce surrogate modeling of shock-induced pore collapse process," Shock Waves **34**, 237–256 (2024).

[16] Z. Lovinger, C. Czarnota, S. Ravindran, C. Kettenbeil, A. Molinari, and G. Ravichandran, "Shock structure and spall behavior of porous aluminum," in AIP Conference Proceedings, Vol. 2272 (Nov. 2020).